A Systems Engineering Approach to Disturbance Minimization for Spacecraft Utilizing Controlled Structures Technology

by

Christopher Emil Eyerman

B.S. Honors degree in Mechanical Engineering, The Pennsylvania State University

(1985)

SUBMITTED IN PARTIAL FULFILLMENT OF THE

REQUIREMENTS FOR THE DEGREE OF

Master of Science

in

Aeronautics and Astronautics

at the

Massachusetts Institute of Technology

June 1990

Signature of Author ______________________________

Department of Aeronautics and Astronautics

May 1990

Certified by ______________________________

Professor Joseph F. Shea

Thesis Supervisor, Department of Aeronautics and Astronautics

Accepted by ______________________________

Professor Harold Y. Wachman

Chairman, Department Graduate Committee

A Systems Engineering Approach to Disturbance Minimization for Spacecraft Utilizing Controlled Structures Technology

by

Christopher Emil Eyerman

Submitted to the Department of Aeronautics and Astronautics
in partial fulfillment of the requirements for the degree of
Master of Science in Aeronautics and Astronautics

Abstract

Future precision space vehicles with inherently large and flexible structures must be considered as complete systems in order that mission performance may be achieved. This includes a framework to meet the challenge of disturbance minimization for spacecraft with the use of controlled structures technology (CST). A system level approach to this problem addresses the potential for controlling the spectrum of spacecraft disturbances at their origin, along the structural transmission path, and at sensitive system elements through the use of an appropriate mix of CST techniques. This thesis characterizes spacecraft disturbances and develops models for use in assessing the magnitude and nature of the required minimization task. An overview of the available CST methodologies is provided to display the potential utility of these tools with respect the disturbances and integration with the system. Representative of this class of spacecraft, a space-based optical imaging interferometer is developed through conceptual design, revealing demands placed by such a system on the CST-disturbance minimization task, and leading to the development of a numerical model. An investigation into the design of the major subsystems, power, attitude control and payload, illustrates the approach for minimizing disturbances through subsystem design, and uncovers some of the interactions between subsystems as a result of structural flexibility, precision requirements and integration of CST tools. Also, performance specifications are verified through a first order implementation of minimization techniques to the spacecraft numerical model. This thesis serves to scope the systems responsibilities in the design of CST spacecraft to minimize disturbances, and provides the basis for further and more detailed systems investigations in this area.

Thesis supervisor: Dr. Joseph F. Shea
Adjunct Professor of Aeronautics and Astronautics

Acknowledgements

I wish to express my sincere gratitude to Professor Joe Shea. His perceptions, guidance and patience were invaluable in getting me focused on the real problem, and realizing that "it's not that difficult". I am honored as Joe's first graduate student in his new "retirement". I am also quite grateful to Professor Ed Crawley for supporting me in the Space Engineering Research Center, providing me with his valued insights and a stimulating environment, and for generating the initial nucleus for this research.

I dedicate this thesis to my family. To my mother and father, I am especially indebted, for it has been through their enduring love, faith and inspiration that I have come this far, and with which I am able to persist. To my brothers Mark and Greg, and my favorite sister, LuAnn, I also give my thanks for their support and friendship, which always seems to be strongest in these challenging times. I couldn't have done it without you, family.

Many thanks also go out to all of the graduate students in SERC with whom I have worked, and who have unselfishly provided their time for my numerous questions.

But above all, I thank the Lord for providing me this tremendous opportunity, the gifts to confront it, and the strength to endure.

Contents

List of Figures

List of Tables

Nomenclature

A_{apt}	=	area of aperture
A_s, A_t	=	shear areas
B_E	=	earth's magnetic flux density
C_d	=	drag constant
D	=	interferometer baseline vector
d_{apt}	=	aperture diameter
E	=	Young's modulus
F	=	force
f_1	=	fundamental frequency
G	=	shear modulus
H	=	angular momentum
I, I_{ss}, I_{tt}	=	moments of inertia
ΔI	=	inertia imbalances
J	=	rotational inertia
$\mathbf{K}$	=	stiffness matrix
λ	=	wavelength of light
M	=	stellar magnitude limit
$\mathbf{M}$	=	mass matrix
μ_e	=	earth's gravitational constant
$\mu_{s/c}$	=	spacecraft magnetic dipole moment
ν	=	Poisson's ratio
P_r	=	radiation pressure
ρ	=	density
ω	=	rotational velocity
Ω	=	matrix of eigenfrequencies
Φ	=	modal matrix
S_f	=	force power spectral density
σ	=	RMS value, or $\sqrt{variance}$

τ, T	=	torque
T_s	=	sampling interval
ζ	=	damping ratio
ζ_i	=	modal damping ratio
ζ_I	=	isolator damping ratio

Acronyms

ACS	=	attitude control subsystem
CMG	=	control moment gyro
CST	=	controlled structures technology
FE	=	finite element
FEM	=	finite element model
FGI	=	fine guidance interferometer
FHST	=	fixed head star tracker
FOV	=	field of view
G/E	=	graphite epoxy
GPM	=	gallons per minute
HST	=	Hubble Space Telescope
I&M	=	interferometer and metrology
I-RWA	=	improved reaction wheel assembly
MWA	=	momentum wheel assembly
OPTICS	=	Orbiting Precision Tetrahedral Interferometric CST Spacecraft
PCD	=	pathlength compensation device
PL,P/L	=	path length
PSD	=	power spectral density
RGA	=	rate gyro assembly
RMS	=	root mean square
RTG	=	radioisotopic thermoelectric generator
RWA	=	reaction wheel assembly
SA	=	solar array
S/C	=	spacecraft
SI	=	scientific instruments

Chapter 1

Introduction

1.1 Background

Systems engineering is a discipline dedicated to the design of a whole system as opposed to design of its constitutive parts. For complex aerospace systems, this whole has numerous subsystems and components with many complicated interactions arising when they are connected through an intricate exchange of information, mass and energy. In this network, the larger, global interactions typically dominate, affecting each of the elements in a somewhat collective fashion. But, quite often, an accumulation of smaller, localized factors may result in unacceptable overall performance, or the effects and limitations of a single component may generate a disproportionate influence on the total system. Additionally, an aggregate of many individually reliable components may add up to an unreliable system, due to unexpected interactions or conflicting individual objectives, generating phenomena far from what the designer had expected. Thus, the unifying function provided by systems engineering is required, which has as its primary responsibility the successful operation and harmony of the complete system in meeting mission objectives.

A fundamental systems process underlies the definitions developed by several authors [6,16], and is summarized here. Systems engineering is the process of selecting and integrating the appropriate combination of scientific and technical knowledge, equipment, and available resources in order to translate an operational need into system performance requirements and a system design, which can be effectively employed as a coherent whole to achieve the stated goal or purpose. This operational need and performance requirements are transformed through a highly iterative process of design, analysis, synthesis, optimization, simulation and test, where related subsystems and elements are integrated to assure compatibility of all physical and functional interfaces toward optimizing the overall system performance in a total engineering effort.

Since the early 1960's, an emphasis on this systems engineering approach to a wide range of highly complex systems has developed [16]. This is particularly true for the inherently diverse aerospace systems, where the nucleus for present-day spacecraft systems engineering was formed through the Apollo program [27], in which this author's thesis advisor was highly instrumental. Since then, every space mission has utilized some form of this systems process in assuring that mission objectives are met in an efficient transformation of requirements into a system design.

The current trend in civilian space missions for observatory-, and exploratory-class spacecraft is toward larger structures with increasingly stringent performance requirements. This trend, coupled with the need for mass efficient spacecraft leads to vehicle structures which are inherently susceptible to vibration and flexible interaction with control systems. Low mass and tight tolerance designs, and the use of materials with high specific stiffness result in flexible structures with very little inherent damping. Vibrations can thus propagate freely through them with little attenuation. These structures are also characterized by having densely spaced flexible modes, which, as configurations become larger, move lower in the frequency spectrum. And as performance demands increase and attitude control bandwidths move up into the region of structural modes, undesirable flexible interaction occurs.

Traditional approaches for avoiding this modal interaction through structural stiffness requirements and lower control bandwidths are no longer applicable. Therefore, in an attempt to minimize spacecraft vibrations and control the shape of structures in the presence of a spectrum of vehicle on-board and external disturbances, the field of controlled-structures technology (CST) has developed. CST includes a wide range of techniques and methodologies focused toward the attenuation of and/or compensation for structural vibrations, the reduction of flexible interaction with spacecraft control systems, and precision shape control for structures with inherent flexibility. These CST "tools" are primarily grouped into passive structural techniques, passive damping augmentation, vibration isolation, and active structural control. Space vehicles utilizing these tools are termed CST-spacecraft, and are the focus of this study. Specifically, this thesis is concerned with the application of the systems process to CST spacecraft toward minimizing the vibratory and flexible effects of disturbances to levels consistent with mission performance objectives.

1.2 Motivation

CST spacecraft must be considered as complete systems. As far as the overriding goal, or mission objectives, it is not sufficient to simply evaluate performance of discrete elements, such as the performance of certain CST tools, and try to extrapolate to overall system performance on the basis of individual demonstrations. The "system" matrix contains off-diagonal terms, if you will. Rightfully, research into the individual component technologies will provide the capability required of CST tools. But, on their own, each of these elements are of little utility unless they fit into the overall disturbance minimization scheme and are able to provide a net benefit to the system as a whole.

Beyond this, a CST tool must act harmoniously with other elements of the CST subsystem, and all other interfacing elements of the system. That is, the complete disturbance minimization scheme must be considered in the system context, with elements of sufficient type and capacity to confront each portion of the disturbance spectrum and within each region of the spacecraft. The goal is to meet mission performance requirements with an "optimum" combination of CST tools, in the least costly implementation to the system. Elements should be chosen which enhance the net performance while complementing, or at least not hindering, the performance of other elements, and should integrate to form a robust system which is reliable and does not overemphasize or over strain the capacity of any one element.

1.3 Overview

Chapter 2 discusses the spectrum of spacecraft disturbances confronting the vehicle, and formulates representative models for use in defining the disturbance minimization task. Disturbances external to the spacecraft system, or environmental effects, are characterized, as well as sources on board or internal to the vehicle system acting to excite flexible behavior in the structure and degrade performance.

Chapter 3 presents an overview of the various CST techniques, or tools which the system designer may call upon in approaching the disturbance minimization task. Methods for passive structural design, passive damping augmentation, vibration isolation, and active structural control are addressed. Some of the basic performance values are included, as well as other important system variables such as relative mass efficiency, physical parameters, power demand and disturbance types confronted.

Chapter 4 is devoted to the development of a point design for illustrating the systems approach to disturbance minimization. A conceptual design for an interferometric spacecraft (OPTICS) is developed, providing an overview of the demands placed by a representative precision CST vehicle. Also, a numerical model is formulated from the basic system configuration for use in the following chapter.

Chapter 5 takes an indepth look at three major subsystems of the OPTICS spacecraft: Power, Attitude Control and the payload subsystem, Interferometer & Metrology. Candidate options are evaluated with respect to subsystem requirements and configured into representative systems. Specific disturbances are then quantified and open-loop system performance response is obtained. A set of criteria and recommendations are formulated for design of each subsystem toward reducing disturbances and their effects to levels consistent with performance specifications. The chapter provides data and motivation for the formulation of a general systems approach to disturbance minimization, and reveals some of the constraints imposed through flexible interactions and the need to limit disturbances on the subsystem design.

Finally, Chapter 6 provides a summary of the systems approach to disturbance minimization. Information on the spectrum of disturbances and available CST techniques, and results through the OPTICS design are pooled into a general framework available for this and a larger class of precision spacecraft.

Chapter 2

Characterization of Spacecraft Disturbances

2.1 Introduction

For the spacecraft designer to accurately assess the challenges of structural control, attempt a control design, or begin the selection of hardware, requires an acute understanding of the mission performance metric, the spacecraft structural and vehicle system characteristics (plant dynamics), and the relative characteristics of the disturbance environment the spacecraft will be subjected to. The latter element is the goal of this chapter. A disturbance is any undesirable or uncontrollable effect, a force or torque vibration, structural distortion or electrical anomaly, which, when interacting with the spacecraft dynamical properties, produces a degradation in the performance parameters. To characterize disturbances is primarily to define the spectrum, ie. the magnitudes and frequencies of vibrations. But, it must also include information pertaining to the locations and implementational scenarios, that is, which ones are where and when are they active.

When looking at the spectrum of potential disturbances, two primary groupings may immediately be distinguished [20]: those disturbances produced as a result of the spacecraft's interaction with the space environment, including all effects "external" to the spacecraft system, and all "internally" generated disturbances, or those vibrations resulting from the operation and/or interaction of spacecraft components and subsystems. External disturbances typically tend to be low frequency, on the order of the orbital rate, and can usually be treated as DC inputs by the spacecraft attitude control system (ACS). However, these disturbances can be large drivers in the sizing of subsystem elements (primarily ACS), and directly affect the rate at which some devices operate. This subsequently affects the spectrum of internally generated disturbances. Additionally, these external effects may produce deformations and deflections which alter the spacecraft geometric and mass distribution properties, potentially producing unstable interactions. Therefore, an understanding of these external effects is important for an accurate assessment of the total disturbance environment, and a discussion of these is covered first. Following, internal disturbances are generally the more troublesome vibrations for precision spacecraft, in that they tend to cover the spectrum over which interaction with flexible modes of the spacecraft structural subsystems and components are unavoidable.

2.2 Environmental Disturbances

As mentioned, those disturbing effects (forces and torques) resulting from the spacecraft's interaction with its orbital environment are termed external disturbances. These interactions arise due to the coupling of the vehicle properties (physical dimensions, material composition, etc.) and the environmental characteristics (atmospheric density and composition, gravitational and magnetic fields, etc.). The frequency of these effects tends to be quite low, on the order of the orbital rate (LEO $\approx$90 min, or 10^{-4} Hz), are generally well below the first flexible modes of the spacecraft, and are typically within the regime of the spacecraft rigid body attitude control system (ACS). Therefore, the resulting *torques* on the spacecraft body, producing attitude errors, are of principle interest. As torque is applied over time, vehicle angular momentum builds up, and must be reacted and/or offloaded with control actuators to maintain attitude specifications.

The primary external effects discussed are torques produced from gravity gradients, atmospheric drag, radiation pressure and magnetic dipoles. Other environmental effects, including particle impacts and eclipse transients, will be addressed as additional areas of concern. For the following analyses, the orbital environment is considered that from the earth primarily (gravitational, magnetic and atmospheric), except, of course, for the calculation of solar radiation torques. Lower order effects, such as from remote bodies (primarily sun and moon), earth oblateness, relativity effects, etc. will not be addressed, as the following relations for external disturbances will be sufficient for most preliminary design analyses. For a more thorough treatment of these disturbances and of the secondary effects, see [1,20], and the NASA references.

Primary objectives for a preliminary phase external disturbance analysis are to:

- Obtain a reasonable approximation of the magnitudes of environmental torques and angular momentum.
- Identify geometrical features, eg. flexible appendages, with the greatest potential for causing instability.

- Determine constraints imposed by various spacecraft configurations on the attitude control and structural control subsystems.
- Indicate whether a more precise, detailed analysis is required.

2.2.1 Gravity Gradient Torque

Because the earth's gravitational field is not uniform over the distributed mass of a spacecraft, a gravity bias or gradient will exist. These variations in specific gravitational force (magnitude and direction) over a material body lead to a gravitational torque about the spacecraft mass center. The net torque, then, arises from the constitutive effect of each mass element under the influence of the gravitational field. Therefore, to minimize a gravity gradient, the spacecraft should be as isoinertial as practical, ie. equal principle moments of inertia and no coupling between axes. This can become particularly difficult as spacecraft become larger, or are composed of multiple, slewing appendages, ie. a non-constant inertia tensor.

Considering earth as the only attracting body, with a spherically symmetric mass distribution, and a single body spacecraft which is very small with respect to its distance from the mass center of the earth [20], we get the following net force and torque on the spacecraft:

$$\vec{F}_g = -\left(\frac{m\mu_e}{R^2} \right) \vec{r}_c \tag{2.1}$$

$$\begin{aligned} \vec{\tau}_g &= \left(\frac{3\mu_e}{R^3} \right) \vec{r}_c \times \vec{I} \cdot \vec{r}_c \\ &= -\left(\frac{3}{mR} \right) \vec{F}_g \times \vec{I} \cdot \vec{r}_c \end{aligned} \tag{2.2}$$

Where: μ_e = earth gravitational constant (=$M_e G$) =3.986 x 10^{14} Nm^2/kg

m = net mass of spacecraft (kg)

R = distance from spacecraft mass center to earth mass center ($R_e \approx$6378 km)

r_c = unit vector from vehicle mass center to earth mass center

I = spacecraft inertia tensor ($kg\ m^2$).

Equations 2.1 and 2.2 are accurate to within a fraction of a percent, ie. ignoring higher order terms and earth oblateness effects, for example. The primary limitation in estimating gravity gradient torques comes from inaccuracies in calculating the inertia tensor:

$$\vec{I} = \begin{bmatrix} I_{xx} & I_{xy} & I_{xz} \\ I_{xy} & I_{yy} & I_{yz} \\ I_{zx} & I_{zy} & I_{zz} \end{bmatrix}$$

This is inherently difficult to estimate for a large, complex spacecraft, and therefore care must be taken here. Further, off-diagonal terms may be minimized by careful selection of a coordinate system to coincide with the body's principle axes. Performing the matrix operations in Eqn 2.2 and dropping higher order terms, the maximum GGT is a result of the difference between two principle axis moments of inertia, or an off-axis term in the inertia tensor, according to:

$$\begin{aligned} |\tau_g|_{max} &= \left(\frac{3\mu_e}{R^3}\right) \times (\Delta I) \\ &= 3\omega_o^2 \times (\Delta I) \end{aligned} \tag{2.3}$$

Where ω_o is the orbital angular rate at radius, R, (rad/sec). Depending on the inertia imbalance ΔI, primary or off-axis term, either cyclic or secular disturbances are produced. Differences in primary axis inertias produce cyclic torques on the vehicle, whereas an off-axis inertia term results in both cyclic and secular torques over the orbital period. Equation 2.3 holds for both torque types, however, the maximum angular momentum according to $H = \int \tau dt$ is given by:

$$\begin{aligned} |H_{cyc}|_{max} &= \left(\frac{3\mu_e}{2\omega_o R^3}\right) \times (\Delta I_c) \\ &= \left(\frac{3}{2}\right) \omega_o \times (\Delta I_c) \\ |H_{sec}|_{max} &= \left(\frac{3\pi\mu_e}{\omega_o R^3}\right) \times (\Delta I_s) \\ &= 3\pi\omega_o \times (\Delta I_s) \end{aligned} \tag{2.4}$$

From Equations 2.3 and 2.4, magnitudes of the gravitational torque and angular momentum vary as R^{-3}, therefore, this disturbance diminishes by nearly three orders of magnitude as altitude increases from low earth orbit (LEO) to geosynchronous (GEO). For earth-pointing spacecraft, gravity gradient effects are effectively DC, with no cyclic components. However, when the spacecraft rotates with respect to the gravitational field, in star tracking mode for example, the torque is periodic at two times the orbital rate, and may also contain secular contributions. These effects also depend on the orientation of the inertia tensor with respect to the axis of rotation, or where in the sky the vehicle is pointing.

2.2.2 Atmospheric Torque

At orbital altitudes, the atmospheric density is small, such that the momentum transfer between the gas particles and the vehicle does not force an immediate descent of the orbit.

The spacecraft - atmosphere interaction is at the limit of the laws of aerodynamics, and is more accurately characterized by considering the atmosphere with a free molecular flow model, ie. the mean free path of the gas molecules is much greater than the size of the spacecraft, and the presence of the vehicle does not alter the flow field. This model considers the momentum transfer to the vehicle (disturbing force and torque) as a function, not only of atmospheric density and vehicle relative speed, but, of the vehicle surface material (composition, roughness, temperature, etc.), particle interaction coefficients (diffuse/specular reflection, accommodation, etc.), and the gas composition. These factors are used to calculate the contributions of each spacecraft element to the net torque acting on the vehicle. A detailed assessment of this is given in references [32,34], however, for a first order estimate, atmospheric disturbances will be approximated as net aerodynamic forces and torques:

$$\vec{F}_a = \left(\frac{1}{2} C_d \, \rho_a \, v^2 \, A\right) \cdot \vec{n} \tag{2.5}$$

$$\vec{\tau}_a = \vec{e}_a \times \vec{F}_a \tag{2.6}$$

Where: v = magnitude of spacecraft relative velocity to the atmosphere (m/s):

$$\begin{aligned} |\vec{v}| &= |\vec{v}_{s/c} - \vec{v}_a| \\ &= \sqrt{\frac{\mu_e}{R}} - \left(\frac{2\pi R}{24\ hr}\right) \end{aligned} \tag{2.7}$$

v_a = assumed to rotate at a velocity constant with the earth surface
(LEO: 495 m/s; GEO: 3080 m/s - equatorial)

$\vec{n}$ = unit vector in a direction opposite that of velocity

A = instantaneous area of incidence, normal to $\vec{n}$ (m^2)

R = distance from earth center of mass to vehicle center of mass (m)

ρ_a = atmospheric density (see Figure 2.1) (kg/m3)

C_d = drag coefficient (generally assumed ≈2.6)

$\vec{e}_a$ = eccentricity vector from center of mass to center of pressure (m)
(generally a few percent, < 5%)

The center of pressure is defined as the single point of application on a surface of a force equivalent in magnitude to the net pressure force acting over the entire surface. When the line of action of this equivalent force at the center of pressure does not pass through the center of mass, a torque is produced. Thus, we see that aerodynamic torques will vary according to the spacecraft orientation with respect to its velocity vector ($\vec{v}_{s/c}$), ie. a varying projected area, and with respect to the atmospheric velocity ($\vec{v}_a$). For example,

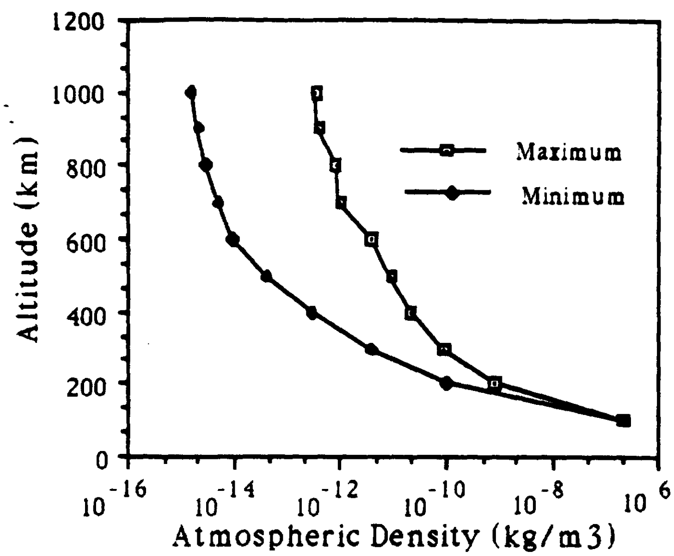

Figure 2.1: Maximum and Minimum Atmospheric Density Profiles for High and Low Solar Activity.

an inertially pointing spacecraft will experience a periodic disturbance proportional to the orbital rate, varying as the incident area of the spacecraft. Additionally, a spacecraft in an inclined orbit will pick up an additional drag component as the vehicle cuts across the atmospheric velocity vector and the atmospheric bulge, experiencing its maximum at the equatorial crossing (max v_a, ρ_a).

The accuracy for estimating aerodynamic disturbances is therefore primarily limited by how accurately the designer can predict the incident surface area of the spacecraft throughout its orbit. Also, from Figure 2.1, the atmospheric density profile decreases exponentially with altitude, similar to gravity gradient torques, exerting its greatest effect in low earth orbit. Variations in the atmospheric density can be large and over relatively short times, resulting in rapid changes in the atmospheric pressure [44]. These ionospheric "bubbles" may be modelled simply as a step in the aerodynamic force profile, with magnitudes of 25-50% the maximum force.

2.2.3 Electromagnetic Radiation Torque

Electromagnetic radiation can be thought of as a momentum flux of photons, which, when intercepted by the surfaces of a spacecraft, produce a pressure force over the incident areas resulting in a net torque about the spacecraft mass center. The radiation source in the orbital environment is primarily from direct solar illumination, with secondary sources being from earth reflected sunlight and earth emitted infrared radiation. Radiation intensity varies as the inverse square of the distance from the source, thus, solar pressure is effectively constant for earth orbiting spacecraft, whereas the effects of radiation from the earth will decrease with altitude. Radiation pressure is often modelled using the wave theory of light, or analogously to the free molecular approach to aerodynamic pressure, where a careful assessment of the incident surface shape, constituents and optical properties is important for a detailed and accurate analysis. It will suffice, however, in our preliminary analysis to model the radiation disturbances as essentially constant average or maximum pressures acting over the exposed surface area of the vehicle:

$$\vec{F}_r = (P_r\ A) \cdot \vec{r} \tag{2.8}$$

$$\vec{\tau}_r = \vec{e}_r \times \vec{F}_r \tag{2.9}$$

Where: A = instantaneously exposed area (m^2)

$\vec{r}$ = unit vector in a direction parallel to photon flux

$\vec{e}_r$ = center of pressure to center of mass eccentricity (m)

and maximum P_r is given by:

$(P_r)_{max} = P_{sr} + P_{er} + P_{ee}$

With:

P_{sr} = solar radiation pressure:

$4.5\ x\ 10^{-6}\ N/m^2\ (6.5\ x\ 10^{-10}\ lb/in^2)$

P_{er} = earth-reflected radiation pressure:

$2.0\ x\ 10^{-6}\ N/m^2\ (2.9\ x\ 10^{-10}\ lb/in^2)$ (LEO-max)

$3.0\ x\ 10^{-8}\ N/m^2\ (4.3\ x\ 10^{-12}\ lb/in^2)$ (GEO-max)

P_{ee} = earth emitted radiation pressure:

$(\approx \frac{1}{3})\ P_{er}$

P_{sr}, as mentioned, is relatively constant for earth orbits, varying in magnitude by less than 1% over the orbit and 6% seasonally. Considering the other uncertainties in the calculation, primarily the determination of effective area and center of pressure, the value of P_{sr} may well be considered constant. The value for P_{er}, on the other hand, will vary greatly, not only with altitude, but with latitude and longitude due to the rather complex behavior of reflectance from the earth. Maximum values are given above, corresponding to the subsolar point. P_{ee} will also vary as the inverse square of the altitude, but is independent of latitude and longitude, ie. P_{ee} is earth-generated. The effect of radiation pressure disturbances is handled in the same manner as aerodynamic torques, with the strong dependency on spacecraft orientation and incident area. One additional solar pressure effect that will be noted is the transient behavior during eclipse, particularly as the vehicle transgresses the penumbra, where an unusually large pressure gradient may arise. For a more detailed analysis of radiation pressure disturbances, see references [20,31,34].

2.2.4 Magnetic Torque

From the same effect that orients a compass needle, a space vehicle with a net magnetic dipole moment within the influence of the earth's magnetic field will experience a torque according to:

$$\vec{\tau}_m = \vec{\mu}_{s/c} \times \vec{B}_E \tag{2.10}$$

Where: $\mu_{s/c}$ = *net* magnetic dipole moment of the spacecraft ($A\ m^2$)

$\mu_{s/c}$ per unit mass = $(1\ to\ 3)\ x\ 10^{-3}\ (A\ m^2/kg)$

B_E = earth's magnetic flux density (Tesla) (see Figure 2.3)

(ex. $B_E\ =\ 3\ x\ 10^{-5}$ Tesla, at 400 km)

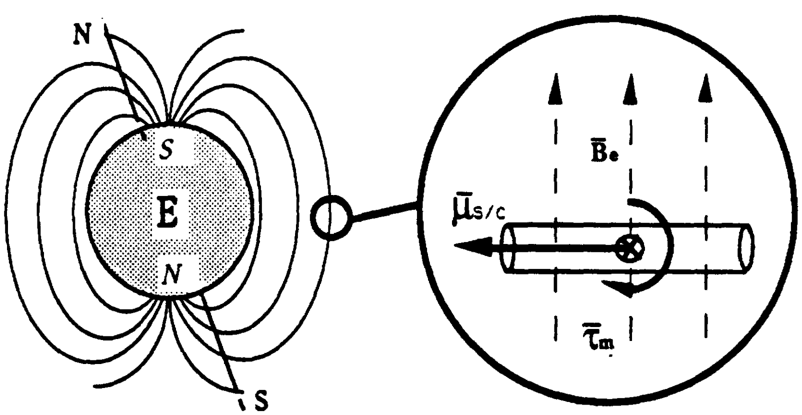

Figure 2.2: Schematic of the Basic Dipole Model for Earth's Magnetic Field

In this case, the dipole moment vector acts as the compass needle that tends to align itself with the magnetic field. The dipole in Eqn. 2.10 represents the sum of residual dipoles from each of the spacecraft elements, induced dipoles from current loops and electronics, permanent magnets and perhaps magnetic dipoles from torque rods. The latter element (torque rods) will not be considered here, as it is not an undesirable disturber, but rather an actuation device. The earth's magnetic field is generally modelled as a simple dipole at the Earth's center, as in Figure 2.2. It has field intensity, I (= $10^7\ Tm^3$), with the magnetic North pole coinciding with the earth's South, and skewed approximately 11 degrees from its spin axis. For low earth orbits, the field is generally stable, however, it tends to be rather unsteady at geostationary altitudes due largely to the flux of solar plasma. In our preliminary analysis, it will suffice to consider the field constant with magnitudes from Figure 2.3, and direction per the basic dipole model. According to this dipole model for the earth's magnetic field, the field strength will decrease as R^{-3}, therefore, as with aerodynamic torques, their effect will diminish rapidly altitude.

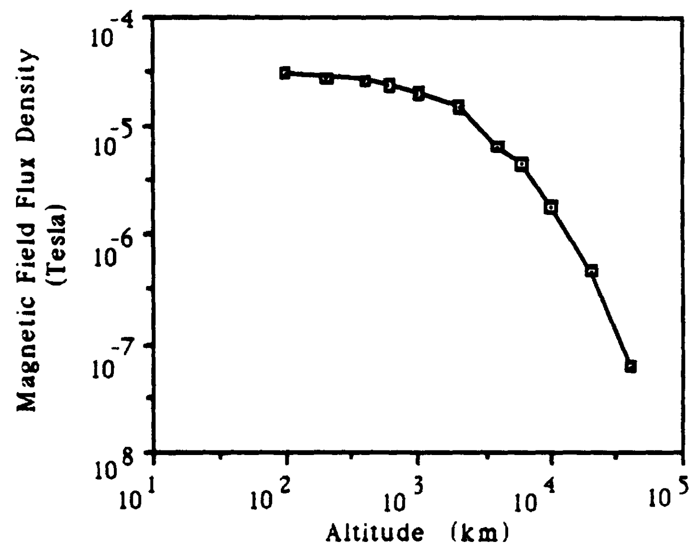

Figure 2.3: Earth's Magnetic Field Intensity at the Magnetic Equator.

2.2.5 Other Environmental Disturbances

All of the previously discussed environmental disturbances are deterministic in that they arise from the "known" physical properties of the orbiting bodies. The truly stochastic process of meteoroidal impacts presents another possible disturber with the potential not only to induce vibrations through impulsive impacts, but to produce catastrophic damage to critical spacecraft components, rendering the spacecraft useless. Fortunately, the incidence of larger (>1 gram) meteoroids is rare, with most in the range of magnitudes from 10^{-9} *to* 10^{-6} kg. Statistical models are available for the average meteoroid mass and flux [54] for various orbits and time of year for earth orbiting spacecraft. And the impulse imparted to a spacecraft component can readily be approximated from the above mass values and an assumed average particle speed in the vicinity of earth of approximately 20 km/s.

Another environmental influence which must be considered is that due to solar thermal and pressure transients during earth eclipse. For low earth orbiting spacecraft in low inclination orbits, eclipse spans roughly one third of the orbit, or nearly 30 minutes, with transient effects arising both upon entrance into and exit from the eclipse darkness. These transients may be considered effectively as an instantaneously applied load, both solar thermal heat flux and pressure forces, with specific periods depending on the orbit. Pressure forces can be computed from information previously discussed, and thermal transients may be estimated using an average solar flux of $1353\ Watts/m^2$. The warping and deformations produced by these effects can be significant, particularly from thermal gradients in large flexible structures and appendages, and therefore must be given consideration. Higher altitudes and steeper inclinations can reduce the frequency and duration of eclipse, but carry other mission constraints and must be considered within the entire system design.

For low earth orbiting spacecraft, gravity gradient and aerodynamic effects are highly dominant, with gravity gradient usually greater for spacecraft to date. However, as will be seen in Chapter 5, when space vehicles become larger both of these effects increase proportionately, where aerodynamic forces may dominate depending on the specific spacecraft geometry. For higher altitudes, geosynchronous and beyond, gravity gradient, aerodynamic and magnetic disturbances decrease rapidly, and solar radiation pressure becomes the major effect.

2.3 Internal Disturbances

As indicated previously, those disturbances which are most likely to interact with the flexible modes of the various spacecraft components, and which typically cannot be compensated for within the bandwidth of the rigid body attitude control system are the most troublesome indeed for spacecraft designers. These are the disturbances generally orders of magnitude higher in frequency than the environmental effects, generated on-board or "internal" to the spacecraft system, and acting typically in a more discrete, rather than distributed fashion. A 'jitter' specification is often cited for observatory class spacecraft, which indicates the allowable effect of these onboard, high frequency vibrations on the telescope line of sight or other performance metric [10,11,23,40]. It is helpful to classify or group these sources of internal vibrations, where disturbance sources are broken down to the spacecraft subsystem level. This permits a system perspective of the disturbance spectrum, and develops an understanding of where and how disturbance minimization may proceed. It should be noted that the disturbances and models discussed include many of the primary sources and is not entirely inclusive, providing a good first order assessment of disturbances for a typical CST-class vehicle. Disturbance sources, or disturbers, are discussed under the following subsystems:

- Attitude Control
- Propulsion
- Thermal
- Power
- Data and Communications
- Optical

The optical subsystem includes disturbance elements which are unique to astronomical spacecraft, characterizing this class of precision vehicle.

2.3.1 Attitude Control Subsystem

The Attitude Control Subsystem (ACS) contains sensors and actuators to detect and correct for errors in the desired orientation or attitude of the spacecraft, more specifically, the attitude of the spacecraft payload. It is the operation of these actuators and sensors that produce unwanted disturbances. The control system bandwidth (BW) is typically a compromise between maximizing the BW to provide control authority over actuator and other spacecraft disturbances and minimizing the BW to exclude sensor noise. Of ACS disturbers, control actuators tend to be the greatest contributors, and potentially generate the largest vibrations in the spectrum of spacecraft disturbances, as with Hubble and other observatory-class spacecraft [10,40,56]. Disturbances are produced by control flywheels, such as reaction wheels (RWA) and control moment gyros (CMG), and mass expulsion devices, or thrusters. Chapter 5 discusses ACS subsystem elements in greater detail, and thruster disturbances are covered in the Propulsion section.

Spectra of the mechanical disturbances from control flywheels have been extensively investigated [10,18] both analytically and experimentally, and shall merely be summarized here. Vibrations from a spinning flywheel (RWA, CMG) are generated in the form of axial forces and torques, in line with and about the spin axis, and radial forces and torques, normal to the spin axis. Sources of these wheel disturbances are: electromagnetics and electronics, such as torque motor ripple and cogging (torque); rotor and wheel static and dynamic imbalances (radial torques and forces); and imperfections in the ball bearings and raceways (axial and radial forces). The power spectrum, then, is typically characterized as narrow band force / torque "spikes" at many harmonics of the rotational speed, covering a wide frequency range, and dependant on the rotational velocity. Therefore, for reaction or momentum wheels, the disturbance forces (torques) sweep the frequency spectrum as wheel speed is run up and down. CMG force spikes, on the other hand, will remain relatively stationary due to a nominally constant operating speed. For lower frequencies (below $\approx$100 Hz), it is shown [10] that the amplitude of these disturbances is proportional to the wheel speed squared, except where RWA dynamics enter in, and proportional to the mass of the rotor: $F_d \propto m_r \omega_w^2$.

A candidate model is derived from empirical vibration data from the hard-mounted Hubble Space Telescope (HST) reaction wheels[10,44]. The HST RWA's represent the current state of the art in RWA design and manufacturing for minimum disturbance. Some important characteristics are as follows: HST RWA:

- 25 in (0.635m) diameter
- 0.84 kgm^2 rotor inertia
- 264 Nms max momentum
- 400 W peak
- 105 $lbs.$ (47 kg)
- 0.9 Nm max. torque
- 3000 rpm max wheel speed
- 45 W steady state

Experimental data shows that the $2.8\omega_w$ and $5.2\omega_w$ harmonics of the wheel speed (ω_w) dominate the vibrational spectrum (arising from bearing and raceway imperfections), thus only the first four harmonics are included in the model (N=1, 2, 2.8, 5.2). Using a least-squares fit to the data, where amplitudes are modelled as constant multiples of the wheel speed squared, the force and torque models are described by the periodic functions:

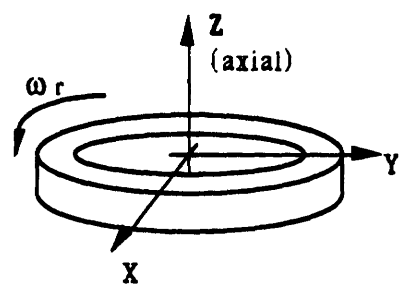

$$F_x = (Cr\omega_w^2)\ Sin(N\theta)$$
$$F_y = (Cr\omega_w^2)\ Cos(N\theta) \qquad (2.11)$$
$$F_z = (Ca\omega_w^2)\ Sin(N\theta)$$
$$\tau_z = (C\tau\omega_w^2)\ Sin(N\theta) \qquad (2.12)$$

Where the constant values (C) are given by ($C_r, C_a :\ x10^{-8}$ N; $C_\tau : x10^{-9}$ N m):

Harmonic $No.$	Radial Force (C_r)	Axial Force(C_a)	Torque (C_τ)
1	4.17	1.70	5.34
2	2.19	2.51	4.18
2.8	4.71	8.59	21.06
5.2	2.38	10.77	40.52

Because the angular velocity of the wheel varies with time, ie. as control torque is applied or momentum is offloaded to torque rods, the angular wheel displacement is determined from: $\theta = \int \omega_r dt$, where ω_r is the wheel speed in rad/sec.

The HST Reaction Wheel operates at a nominal zero wheel speed bias (ω_w=0), but is designed for excursions up to 3000 rpm (50 Hz), at which speed it saturates. Nominal operation of the wheel is expected to see speeds of up to 600 rpm (10 Hz), but a typical analysis may use ω_w=1200-1500 rpm (20-25 Hz) max for a reasonable estimate. The model may also include a low magnitude, broadband random component (a few percent of the maximum amplitude) to account for photon noise and friction induced disturbances from electromechanical devices.

CMG's, as indicated, will display a similar disturbance profile to reaction wheels, being another form of spinning flywheel. However, CMG's operate with a much higher and relatively constant wheel velocity, typically at least twice the maximum RWA speed. They thus will have their disturbance spectrum shifted upward in frequency accordingly, with the potential for larger disturbances according to: $F_d \propto m_r \omega_w^2$. With CMG's operating at a fairly constant rate, however, the force/torque harmonic spikes will remain relatively stationary in the frequency domain, compared with the sweeping nature of RWA's. This comparison will be illustrated in Chapter 5. Another deviation from the RWA spectrum is a potential disturbance from friction in the gimbal mechanism. Friction disturbances have previously been investigated [39], indicating nonlinear CMG gimbal friction generates a random disturbance arising from, for example, tachometer brush friction and hysteresis drag in the brushless DC torque motor. Following are general characteristics of the Sperry single gimbal model M225 CMG [40] and peak magnitudes for its primary disturbances:

- 52 kg
- 300 N m max torque
- 20 Hz control BW
- 6000 RPM max speed
- 300 N m s max momentum

Disturbance	Off the Shelf Version	"Quieted" Version
Static Unbalance	13 N	0.4 N
Dynamic Unbalance	5.5 N m	0.12 N m
Rate Ripple Torque	$(3\%)T_c$	$(0.5\%)T_c$
Torque Ripple	10 N m	1.5 N m

T_c is the commanded torque. Here, it can be seen that disturbances for the quieted version are greater than the maximum values expected for RWA's. But, extrapolating the disturbance model for RWA's to 6000 rpm displays disturbances equivalent to and much greater than those shown here, at frequencies up to 500 Hz. However, the RWA model was shown to break down at frequencies above a few hundred hertz max, where the greater forces arise. So for this bandwidth, extrapolations for CMG disturbances based on the RWA model seem justified.

Disturbances from attitude sensors arise either mechanically from gimballed or scanning devices, or electrically as attitude errors from signal noise. Mechanical vibrations from a gimballed or scanning sensor are typically small, and must be considered on an individual basis. Rate gyroscopes are another source of disturbance, with vibrations produced mechanically by gas flow around the spinning flywheels and low frequency wheel hunt, and electrically in the drive and rebalance circuitry. Rate gyros on the Space Telescope were evaluated for these disturbances [12], and electrical and mechanical design improvements lead to a qualified low noise instrument. Sensor electrical noise can be described as a zero-mean, uncorrelated random error in the sensed variable (voltage, θ, ω), having some variance (rms value), σ_e^2, over the useful bandwidth of the sensor. This is effectively treated as a mechanical vibration disturbance by the attitude control system, and must be accommodated in the control design, typically by constraining the upper bound of the control bandwidth.

2.3.2 Power Subsystem

The primary function of the spacecraft power subsystem is to provide electrical power throughout the life of the spacecraft. This includes power generation, storage, conditioning, regulation and distribution to critical spacecraft components. The generation and handling of electric power, in general, does not manifest itself in the form of mechanical vibrations. It is the generating devices and their physical properties which produce unwanted disturbances, including thermal energy and electrical interference.

Solar arrays are the most commonly used power generation devices due to their well advanced and proven technology. To obtain maximum solar conversion efficiency, it is desirable to have direct solar incidence on many solar cells. Thus, arrays are generally large, flat, flexible appendages, which are cantilevered off of the spacecraft main body, and actively driven to track the sun. Often, solar arrays account for the lowest bending modes of the spacecraft dynamical system, placing an upper constraint on the ACSbandwidth if it is desired to ignore flexible effects.

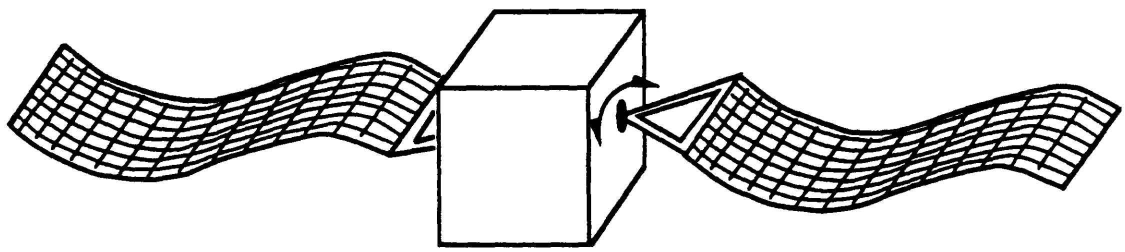

As large, flat appendages, solar arrays are quite susceptible to environmental disturbances, namely aerodynamic and radiation pressure forces. However, as discussed in the first section, these effects are of such low frequency, that they will generally not excite flexible behavior. Solar arrays are also subject to thermal distortions (warping) from variations in the incidence of solar energy. In the extreme, a periodic dynamic 'flutter' can arise from the combined distortions and changing angles of incidence. Also, as the spacecraft transgresses the umbra and penumbra regions of orbit (see Figure 2.4), thermal gradients are high and the potential for unsteady transient deformations in the array exist. This is true in general for large space structures experiencing solar eclipse.

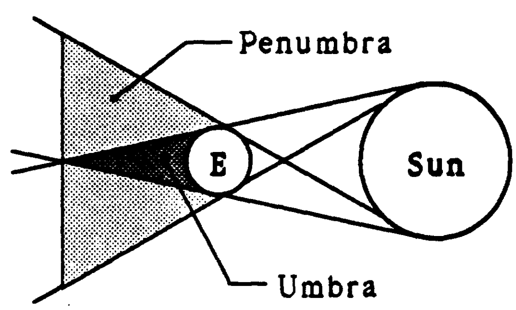

Figure 2.4: Eclipse Regions of Earth Orbit Showing Umbra and Penumbra

Spacecraft slew maneuver and solar array drive commands are generally 'shaped' by a command generator to avoid unstable excitation of these low frequency modes, where the reaction torque is compensated for by the vehicle ACS actuators (eg. reaction wheels).

Aside from the sheer exchange of momentum between the array and spacecraft, this flexi-body interaction may produce a damping torque on the main body following a vehicle maneuver or a solar array tracking slew. The torque is a low frequency, decaying sinusoid dependant upon the amount of damping and the stiffness of the array and support structure. The "settling time" for this disturbance to damp to acceptable values can thus have a large impact on the scientific objectives, and must be dealt with accordingly. As an example, results from a Space Telescope / solar array interaction study show the following [52], for sequences of applying solar array brakes at various times during and following a telescope maneuver with different levels of array damping:

Max Torque at Brake Application (N m)	*Time (sec) to Settle to 0.003 N m* ζ=0.005	ζ=0.02
0.004 to 0.043	2.7 to 19.8	0.7 to 4.8

Where, again, the frequencies of oscillation are dependant upon the array dynamics (typically < 1 Hz). The actuators to drive the position of the arrays are also potential disturbers. Solar array drive mechanisms are generally a brushless DC torque motor or a stepper motor. DC torque motors produce torques on the order of approx. 0.1-30 N m. Primary disturbances from these motors are ripple and cogging torques. Ripple is a torque disturbance parallel to the spin axis caused by motor winding imbalance with magnitudes being a percentage of the command torque (1-5%), and at multiples of the motor speed. Cogging torque is caused by magnetic variations in the motor and is also along the rotation axis. Its magnitude is invariant with the motor torque (1-2%), and at much higher harmonics. Stepper motors, on the other hand, create disturbances from the quantization of their torque commands and the inherent lack of damping. These motors generally produce lower magnitude torques, on the order of 1 N m, and have quantizations as low as a few degrees. To avoid many of these flexible body and drive mechanism disturbances during critical spacecraft operations, science taking mode, for example, the solar array actuators may be locked, fixing the panels at a modest power penalty.

With all of the current carrying wires (harness) snaking throughout the spacecraft, to and from critical electronic components, sensors and actuators, a large dipole moment can be created if care is not taken to sufficiently balance the net effect on the spacecraft. This can be the primary contributor to the net torque from reaction of this dipole against the earth's magnetic field, as previously discussed. Additionally, if cabling is not sufficiently shielded, electrical noise can be picked up which manifests itself as disturbance spikes (current, voltage) at harmonics of the AC current source. This can potentially be a problem for sensitive sensor and actuator signals, however good design, proper grounding and shielding of cables, usually handles it.

Other available power generation devices include nuclear generators and solar dynamic power systems, as discussed in Chapter 5. These are primarily heat generators which can produce disturbances from handling of large amounts of thermal energy and during the dynamic thermal to electric conversion. Static conversion systems have efficiencies up to 15% and dynamic systems may approach 40%, with the residual heat requiring dissipation which can generate thermal distortion errors. Dynamic converters are heat engines with inherent high frequency rotating and pumping equipment, and high rate transport of the working medium. They are therefore subject to dynamic imbalances, friction vibrations, and high rate fluid turbulent effects. Fluid transport produces a random disturbance dependant on flow rate, and is discussed in the Thermal subsystem. Efficient designs include non-contacting gas bearings and dynamically balanced piston arrangements [60] to lower vibration levels. However, disturbances from these devices have not been well characterized, and are currently considered as major vibration sources.

2.3.3 Propulsion Subsystem

Many of the precision spacecraft, toward which this document is principally aimed, fall within the observatory class (telescopes, interferometers,...) which typically have optical components very sensitive to contamination, including the contaminating effluent from thrusters. Therefore, it is likely, as for several current 'Great Observatory' programs, HST and SIRTF, that a propulsion system be eliminated from consideration. However, as mission requirements may otherwise dictate, or contamination issues improve, a discussion of these potential disturbers is included.

In orbit, thrusters, or control jets, are actuators for spacecraft attitude control, altitude control, N-S (E-W) stationkeeping (for higher orbits), and momentum desaturation of attitude control flywheels. Their operation can be characterized by the frequency of actuation thrust: a pulsed, bang-bang impulsive mode (at many pulses per second); on-off step-like mode (many seconds to hours); or continuous operation (low thrust). Aside from the intended control thrust applied to the vehicle, disturbances can arise from either the operation of the thruster, or from the storage and transport of propellant to the thrust nozzle. A primary disturbance from thruster operation is the transient effect from a pulsed or stepped thrust, ie. instantaneously imparting energy at the nozzle location, as it is not possible to 'shape' this actuation thrust. Subsequently, undesirable excitation of spacecraft flexible modes may occur. This may be modelled simply by an impulsive or square wave force input at the thrust nozzle location or a force couple (torque) at the vehicle c.g., of magnitude equal to the thruster rating and depending on the intended duration of thrust. Typical attitude control thrust ratings are approximately < 1 lb to 10 lbs (≈1-50 N) for chemical, and on the order of milli-lbs to a few lbs (milli-N to 10 N) for electrical thrusters. Generally, the higher the control thrust, the shorter the duration of required thrust.

Additional disturbances arise from reaction of propellants in the nozzle, turbulent expansion, plume impingement, nozzle misalignments and imperfections, leakage, etc.. They may be characterized as low magnitude, wideband uncorrelated random vibrations at a magnitude of a fraction (few %) of the desired control thrust. The effect of fluid slosh in a propellant tank (or cryogenic dewar) is a complex problem, depending largely on factors as the propellant mass fraction, tank geometry and surface properties, tank baffling or damping, etc.. A simple method to model fluid slosh in a torroidal tank was developed at Lockheed, and utilized for preliminary dynamic analyses on the SIRTF program [40], and is shown schematically in Figure 2.5. The model uses a rotating pendulous mass inside a cylindrical body to simulate a large mass of fluid, m, rotating about a major spacecraft axis (longitudinal, X, here). Spacecraft motions about either the Y or Z axes, in this configuration, will excite pendulous motion and generate disturbing reaction forces.

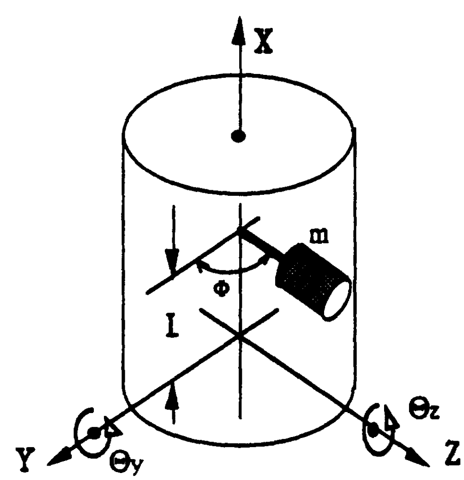

Figure 2.5: Simple 2-DOF Dynamic Fluid Slosh Model (Courtesy Lockheed).

The other fluid effects, dynamic forces from flow turbulence through lines and flow noise through valves and regulators are also complex phenomena. These disturbances are characterized as low amplitude, random vibrations covering a moderately high bandwidth (kHz). The magnitude of these turbulence induced vibrations is highly dependant on the flow rate, path geometry and shaping of the flow field. For further quantification of these disturbances and a discussion of experimental data, see the Thermal Subsystem section on fluidic heat exchangers.

2.3.4 Data and Communications Subsystem

The Data and Communication (D&C) subsystem consists of equipment necessary to collect, store and transmit engineering and scientific data; receive, process and return spacecraft telemetry information; and handling of general spacecraft communications. Mechanical vibrations are generated by electromechanical components such as data storage devices (eg. tape recorders) and servo mechanisms for positioning of antenna dishes and booms, and flexi-body interaction disturbances arise from flexible antenna appendages, such as dishes and omni-directional booms.

The disturbance characteristics for engineering and science data tape recorders have been investigated [15,40], and are included here as characteristic for spacecraft data storage devices. Tape recorders, as typical for electromechanical devices, produce mechanical noise in a spectrum consisting mainly of discrete force/torque spikes at multiple frequencies, dependant upon the speed or frequency of operation. Vibrations are caused by unbalanced parts, gear meshing, synchronization pulses and capstan noise. These are manifest as forces and torques parallel and normal to the axes of rotating parts (reels, gears, etc.), similar to reaction wheel disturbances. Table 2.1 is reduced disturbance data from a series of tests conducted by the manufacturer (Odetics) on the Hubble ESTR development model [15]. The table showsmaximum force and moment peaks at each frequency from the data, and do not include potential design improvements to reduce noise output, and therefore represent conservative bounds.

Table 2.1: Vibration Data for Hubble Space Telescope Tape Recorders (ESTR) in Science Recording Mode (41 in/sec tape speed).

Disturbance	*Magnitude*	*Frequency (Hz)*	*Source*
Axial Force (lb):	0.0017	3.1	reel unbalance
	0.0036	15.0	
	0.0046	16.4	
	0.0041	21.0	
	0.0024	44.4	synch. pulses
	0.0041	58.0	
	0.0043	60.0	
Normal Force (lb):	0.0119	3.1	reel unbalance
	0.0022	16.4	
	0.0044	19.0	capstan noise
	0.0016	29.0	
	0.0134	44.4	synch. pulses
	0.0097	58.0	
	0.0040	60.0	
Axial Moment (in-lb):	0.037	3.1	reel unbalance
	0.032	14.4	
	0.043	16.4	
	0.057	17.5	
	0.049	19.0	capstan noise
	0.041	21.0	
	0.093	44.4	synch. pulses
	0.021	60.0	
Normal Moment (in-lb):	0.067	3.1	reel unbalance
	0.014	21.0	
	0.016	44.4	synch pulses
	0.011	58.0	
	0.016	60.0	

Mechanical vibrations from antenna positioning devices, brushless DC torque motors or stepper motors, are identical in characteristic to the solar array drive mechanisms. For greater pointing accuracy, DC torque motors will typically be used due to the lack of fine quantization of stepper motors ($\approx$1 degree at best). Disturbances from DC torque motors arise from bearing friction, motor cogging and ripple torque, bearing roughness, etc., with ripple and cogging torques being dominant, as previously discussed. The same modelling approach as solar array drive servos is used here, where noise scales generally as command torque, dependant on the inertia and stiffness of the antenna. As antennas become larger, so do the flexi-body interactions with the spacecraft main body. Not only does this present a difficult control task, but also introduces disturbance torques on the main body in the form of momentum exchange during a spacecraft maneuver or antenna tracking slew, and oscillatory damping torques following. These, again, are similar to the flexi-body interactions of the solar array, with a strong dependance on the actual dynamics of the appendage. See the Power Subsystem section for further discussion. An important difference from solar arrays, however, is the need to continuously track antennas, for data transmission and vehicle telemetry, for example. This then stipulates that the associated disturbances are active and must be considered in the minimization scheme.

2.3.5 Thermal Subsystem

The thermal subsystem is responsible for maintaining operational temperature ranges for all spacecraft subsystems, payload and other critical components (the entire vehicle, in other words). It therefore possesses a distributed nature, with strong interdependencies from all of the other subsystems. Primarily a passive system overall, relying on surface coatings, multi-layer blanketing, radiation paths and configurational zones to isothermalize and maintain critical temperatures, mechanical disturbances are typically not inherent. However, as power requirements increase and temperature specifications for scientific payloads tighten, active thermal control techniques become necessary and potential disturbers exist.

Generally, and particularly for spacecraft with precision pointing requirements, it is critical to equilibrate structural subsections to control warpage and prevent undesirable distortions due to CTE mismatch between mechanically-coupled components. Allowable deflections are budgeted from the performance objectives, thus placing a requirement on thermal stability. These disturbances associated with gross thermal deformation are very dependant on the structural characteristics of the vehicle: materials, geometry, spacecraft configuration, and the operating and orbital characteristics. They are therefore entirely mission specific. Temperature fluctuations from operation of on-board equipment, or active cycling of electric heating elements induce localized thermal strains. These disturbances may be generalized as low frequency deformations (on the order of 10^{-3} to 10^{-1} Hz, dependant on the cycling rate of the equipment), and magnitudes, again, which are very dependant on configuration and the temperature excursions.

For missions with exacting requirements on thermal stability of scientific equipment (sensors, optics, laser systems, etc.), or missions exploring the infrared spectrum, cryogenic cooling is often required to achieve very low, stable temperatures, approaching $0°K$. A cryogenic system generally consists of a large dewar of cryogenic fluid (eg. superfluid helium), surrounding or closely coupled to the critical components, with associated plumbing to maintain pressure and provide transport of cryogen. Disturbances are generated from the effects of fluid storage (slosh) and transport (turbulence), similar to propellants, or from fluid pumping and regulation equipment.

For an active fluidic heat exchanger, or flow processes in general, turbulence-generated disturbances are produced. The principle source of excitation in this situation are dynamic jitter forces imposed on the cooled element (mirror, sensor, ...) as the coolant flows through the heat exchanger portion of the assembly, with various inlet and exit plumbing configurations [38]. The turbulent nature of the coolant produces a random disturbance profile in the flow direction and transverse to the flow field from the fluctuating cross flows, as predicted from basic isotropic turbulence theory. This is characteristic, in general, for all flow other transport processes (eg. propellant). From extensive experimental data on various plumbing configurations, flow rates, and flow straightening devices, expected RMS magnitudes of these jitter forces in the bandwidth, 12.5 - 500 Hz, are as seen in Figure 2.6. The figure also shows how RMS magnitude increases with fluid flow rate.

To reduce the transverse turbulent effects, flow straightening devices "shower heads", screens, etc.) are utilized to decrease nonuniformity of the flow field. Additionally, various"no load fittings", basically vibration isolation plumbing connections, have been used effectively to limit transmitted vibrations through the flow lines. The effectiveness of these is shown roughly as the lower range of values given in Figure 2.6. Heat pipes may also be considered as passive or active fluidic heat exchange devices, with relatively low rate fluid transport.

Louvers and mechanized sun shades are occasionally utilized to modify thermal emittance characteristics or shield from thermal energy input, respectively, in certain mission scenarios. As mechanized devices, they are inherently less attractive from a reliability standpoint, and will also introduce mechanical vibrations upon operation. Disturbances

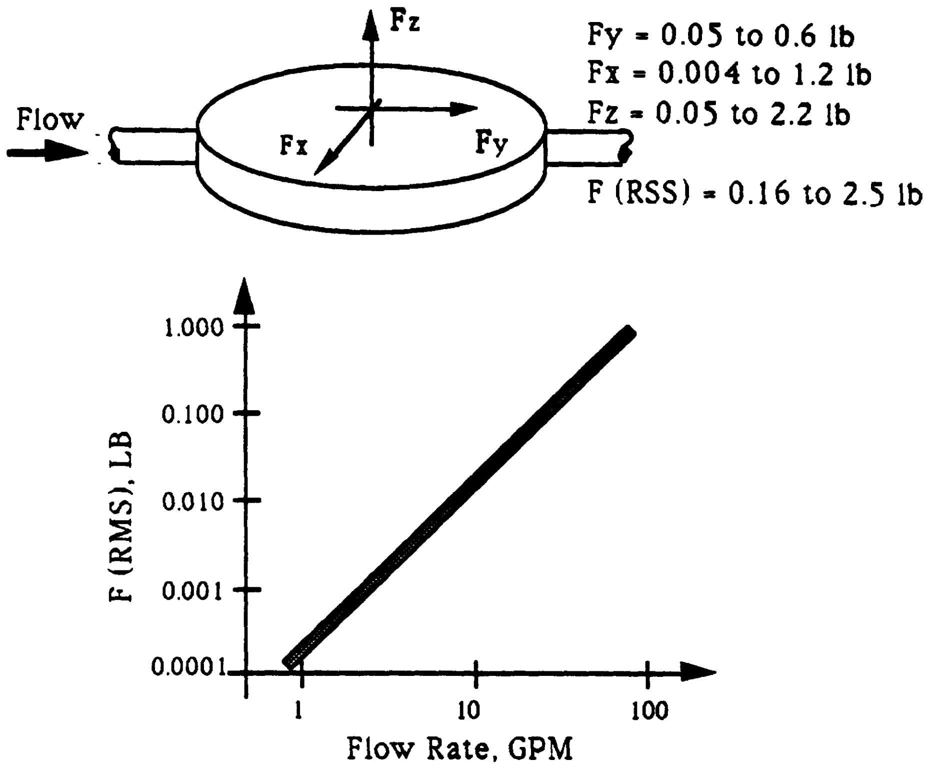

Figure 2.6: Lateral and Flow Direction Dynamic Forces for Coolant Flow Through a Heat Exchanger-Mirror.

are produced, as with other mechanical devices, typically in the form of sliding friction vibrations, electromechanical motor variations, momentum exchange and transient impacts. These are most effectively evaluated on a specific basis.

2.3.6 Optical Subsystem

The optical subsystem, as discussed in this context, includes elements which are typical for observatory-class spacecraft: primarily telescopes and mirrors, and the mechanisms for positioning them with respect to the vehicle. Chapter 5 discusses specific optical system components for an interferometer spacecraft, of which disturbances are outlined here. To collect light from various portions of the sky without rotating the entire vehicle requires gimballing of a flat planar mirror to direct photons into a collecting telescope. The electromechanical drive motors for these "siderostats" are potential vibration sources, as well as friction and mechanization noise in the gimbal assembly. Another means for collecting stellar photons with a stationary spacecraft is to translate the telescope to different locations on the platform. This requires some form of telescope carriage assembly, a drive mechanism and rail system to guide it along the vehicle. Disturbances here, again can arise from the electromechanical drive motor and mechanization of the carriage/rail system, but also may generate significant inertial torques which must be reacted by attitude control actuators. This torquing through the vehicle, as with any slewing appendage, will deform the flexible structure, at magnitudes dependant on the required torque amplitude and structural characteristics between the inertial load and control actuator. Other translating optical assemblies are possible, such as for compensating light path differences in an interferometer, with similar disturbance characteristics to the translating telescope assemblies, scaled by their relative mass ratios.

Precision laser measurement systems will most likely use gas lasers (over solid state) due to good frequency stabilization and high resolution (1 nanometer). These lasers are quite inefficient with respect to the energy required to produce the nominal milli-Watt laser beams, and produce large amounts of waste heat. In start-up operation, the thermal transients induced may produce significant localized deformations in the optics and supporting structure. However, in steady-state operation, thermal equilibrium is achieved and residual temperature fluctuations should be small.

Since no actual data for space-based versions of these mechanized components are available, correlation with earth-based systems may provide representative information. Measurements taken from the interferometric optical components (translating trolleys and gimballed siderostats) at the Mt. Wilson Observatory [26], indicate vibration spectra typically expected for electromechanical devices. These include a broadband, somewhat random component overlayed by discrete high amplitude spikes. For a motion including acceleration and deceleration, the spikes tend to smear, indicating a velocity dependance not unlike reaction wheel vibrations. Peak amplitudes were seen to be on the order of maximum reaction wheel vibrations and greater, for low rate motions (<5 mm/sec). These, however, will depend on the specific application for a prescribed velocity and mass for the translating element, but as indicated, are expected to be at least on the order of reaction wheel disturbances.

Figure 2.7 shows a summary and general categorization of internal disturbances. Categories include the very low frequency and *exponential* effects, *low*, *medium* and *high* frequency periodic, and a group of all *random* disturbances.

Figure 2.7: Summary and Categorization of Internal Disturbances

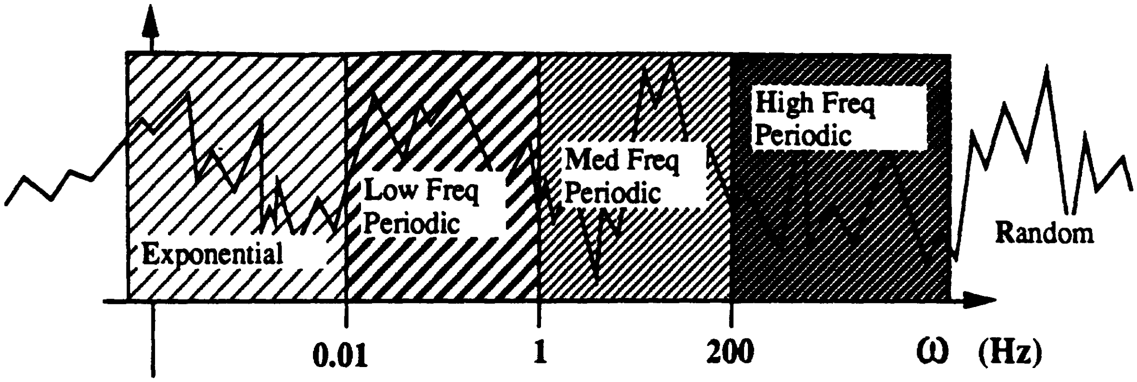

I. Exponential (E): $10^{-6} \Rightarrow 10^{-2}$ Hz
   A. Environmental disturbances
   B. Gross thermal-mechanical deformations

II. Low Frequency Periodic (L): $\sim 10^{-2} \Rightarrow 1$ Hz
   A. Flexi-body interaction torques (damping), and momentum exchange with flexible appendages and movable elements; vehicle fundamental modes
   B. Internal thermal-mechanical fluctuations: active cycling of electric heaters; cyclic operation of dissipating devices
   C. Fliud slosh: propellant, cryogenics
   D. Low frequency electromechanical

III. Med. Frequency Periodic (M): ~1 => 200 Hz
   A. Electromechanical devices: RWA/CMG's, data recording devices, servomechanisms, pumps, displacement actuators, active mounts,etc.
   B. 'Stiffer' flexi-body interactions
   C. Higher harmonics of fluid slosh

IV. High Frequency Periodic (H): ~200 => + Hz
   A. Higher harmonics of electromechanical devices
   B. Electrical noise: AC current

V. Random (R):
   A. Fluid turbulence: broadband
   B. Friction
   C. Sensor / electrical noise (photon, thermal, shot): broadband
   D. Micrometeoroid impact: very low freq
   E. Non-periodic gimballing (thrusters, sensors, antennae): low freq
   F. Thruster firing - transients: low-high freq

Chapter 3

Overview of CST Techniques

The goal of this chapter is to give a brief overview of the CST techniques, or "tools" currently available to the spacecraft systems designer. The discussion follows four major groups defined as: passive structural techniques; passive damping; vibration isolation; and active structural control. This also represents a loose organization of the approach to design of large flexible space vehicles from the more traditional passive design approaches to the high performance actively controlled methods. Basic performance capabilities are covered, as well as other major impacts to the system such as relative mass efficiency, physical parameters, power demands and the general categories of disturbances confronted. The term "CST tool", as used in this document, represents any technique which can enhance the structural performance of large precision space structures. A brief overview is given here, where material is gathered from a wide array of sources, of which the major reference is [9].

3.1 Passive Structural Techniques

One of the fundamental criteria for spacecraft systems design is to create a functional system which operates passively and autonomously while efficiently and reliably meeting the mission performance criteria. This is particularly true of the vehicle structure, which is traditionally passive for smaller, more rigid and less demanding vehicles. Many of these passive techniques for stabilizing the structure, however can be applied to the current class of spacecraft, and are discussed in this section; namely, basic structural design methods for desirable stiffness and dynamic behavior, thermal stabilization measures and thermal expansion tailoring, and dynamic tailoring techniques to create a friendly host for structural control.

3.1.1 Structural Design

Typical design goals for space structures attempt to achieve low mass, high stiffness, linear elastic and dynamic behavior, thermal and environmental stability, and configurations which are deliverable to orbit. Unfortunately, many of these demands are conflicting, and the resulting "optimal" design is a balance of some level of each of these. Traditional high stiffness to weight materials, such as aluminum, and graphite epoxy, are used in efficient, statically determinate and non-redundant configurations of lightweight honeycomb panels, shell structures and lattices. Even so, as dimensions become large, mass constraints drive the design toward flexible structures. Linear dynamic behavior is challenged by the need for deployable/constructible designs where tolerances and mechanical joint assemblies may lead to nonlinear slip and backlash. This issue has been greatly reduced by innovative joint designs such as the NASA-LaRC space station joint, however, uncertainty still exists for the microdynamic behavior of these designs in a weightless vacuum.

Environmentally and thermally stable materials are desirable as the basic building blocks. Composites tend to be the most thermally stable, but are also most susceptible to environmental degradation from outgassing, U-V and atomic O_2 degradation and stress relief in zero-g. Aluminum and other metals are fairly transparent to the environment but have higher thermal expansion rates. Improvements in new alloys and composite materials will be beneficial. However, for the near term, some form of external protection and/or compensation is needed for the sub-micron control of traditional materials.

3.1.2 Thermal Control Techniques

The spacecraft thermal control subsystem controls the temperature variations seen by all vehicle subsystems, including the structure, through passive and active mechanisms. It is the limitations of this thermal control system which permit temperature gradients and structural thermal deformations. Passive control includes paints and surface coatings (α, ϵ), multi-layer insulation (MLI) or blanketing, radiators, heat pipes, thermal isolation and vehicle operational constraints to limit incident solar variations. MLI provides the bulk of the thermal control system, being the interface to the external environment, where improvements are still needed for leaky seams and materials with stable thermal-optical properties. Flying in a sun-synchronous orbits and limiting vehicle rotations with respect to the sun can also provide major benefits by preventing thermal transients.

Active techniques may be employed when thermal energy is too great or temperature requirements are too severe. These are primarily actively controlled heating elements, such as resistive wire strip heaters, thermoelectric coolers and cryogenic systems. Strip heaters provide the only mass-efficient means for active control of a large, distributed structure, and may provide temperature control to within a fraction of a degree C in steady-state conditions, utilizing highly distributed sensors, accurate to 0.001°C. However, for the thermal controller to accurately characterize the structure (truss) and provide appropriate heat input would require 100's of temperature sensors per meter, and nearly continuous heating strips. This will incur a mass penalty and carries a substantial power demand. For example, Space Telescope, a relatively compact vehicle, requires approximately 200 watts (avg) of power for heaters.

3.1.3 Zero CTE

By strategically coupling structural elements with positive and negative thermal expansion rates (CTE), a net structure with very low or "zero" CTE may be produced. The metering truss of Space Telescope is configured with graphite epoxy struts for an overall, axial-direction CTE of $0.06\ x\ 10^{-6}\ in/in/{}^{\circ}F$. This, combined with $\pm 2^{\circ}F$ temperature control results in an overall stability within a few microns (10^{-6} m). These techniques are most effective in a single given direction, where other dimensions are permitted to deform, and increase in complexity with larger and more complex geometries. They are therefore not well suited for multi-directional control of large structures, and could be most effective as local structural elements supporting critical components.

3.1.4 Structural Tailoring

If accurate information on the expected disturbance sources (magnitude and frequency) and their locations, and required control bandwidth are available early in the design of large space structures, then it may be possible to implement structural tailoring. These include stiffness and mass tailoring techniques aimed at prescribing particular frequencies and modeshapes for the global vehicle. The result is not only to avoid major disturbance frequencies, but to provide a friendly host for accommodating structural control methodologies, by permitting a modally free region in the frequency spectrum for controller rolloff, as an example. The early analog to this are the structural stiffness bounds placed on traditional spacecraft to avoid excitation by the ACS. Research is continuing in this area [21], with experimental evidence yet to be shown.

3.2 Passive Damping

The use of materials with high specific stiffness and tight tolerance configurations result in a structure with inherently very little damping, where damping ratios of 0.1% or less are typical. The benefits of passive damping in the overall structural control problem, however, are many [9]. Damping provides the mechanism for removing vibrational energy from the system, lowering the resonant peaks of response and stresses to harmonic vibration and reducing the settling time from transient disturbances. Without stiffening the structure, reduction of the modal time constant, ($\tau_m \approx (1/(\zeta\omega_n))$, requires improved damping. Passive damping also enhances performance of a structural control system by reducing the required control effort, padding stability margins, and simplifying model reduction methods and the controller design. Methods for improved damping, outlined here, are: inherent material and structural mechanisms; strain dampers including viscoelastic materials, friction devices and dissipative electrical networks; and resonant dampers for directing energy to dissipative elements.

3.2.1 Material Damping

The cheapest means for adding damping to the system is to use the natural dissipation in existing structural materials. Internal friction for elastic materials produces a hysteretic strain energy loss which is proportional to the square of the displacement amplitude for a harmonic excitation [25]. Unfortunately, the loss factor of a material is generally in conflict with its stiffness properties. The most commonly used materials, such as aluminum and graphite epoxy, possess material damping ratios of 0.01 to 0.1% max. Whereas ferromagnetic alloys and special damping materials, Teflon impregnated aluminum for example, may approach a few percent. However, ferromagnetics are very heavy, and development is required for specialized materials before they are able to display the stiffness of conventional materials.

3.2.2 Structural Damping

Other than material damping, natural structural dissipation also arises in bonded interfaces, from backlash and slop in joints, and slipping at mechanical interfaces. These processes are inherently nonlinear and produce damping mainly through friction and impacting cycles. As much as 1% damping improvement is typical, however the general attempt of precision structural design is to eliminate these undesirable nonlinearities which complicate the dynamical behavior. Microdynamic behavior of these mechanisms is not well characterized, and is likely to exist even for the best structural designs.

3.2.3 Space Viscoelastics

Viscoelastic materials, typically plastics and rubbers, have good damping characteristics, but are not practical for use as primary structural elements. They are used either in a parallel or limited series arrangement with the primary structure to dissipate energy hysteretically through elastic strain elongation and viscous strain rate dissipation. Viscoelastics are therefore employed in areas of greatest strain on the structure. A layer of viscoelastic material may be applied effectively to large area components such as panels, arrays and antenna dishes, in a parallel arrangement. And adding a rigid constraining layer improves energy transfer to the viscoelastic. Lattice structures are better suited for a viscoelastic material in series with a structural element. A series arrangement offers high damping but at a reasonable stiffness penalty with a viscoelastic in the load path, whereas a parallel configuration produces less damping but does not sacrifice stiffness. Experiments with constrained layer viscoelastics on simple beams have shown a few percent damping improvement, and extensional shear dampers (strut) have seen up to 5% structural damping, with an equivalent reduction in stiffness.

Limitations of viscoelastics include their susceptibility to environmental degradation and outgassing if not properly protected. Viscoelastics are also highly temperature and frequency dependant, with maximum loss factor at an intermediate, transition region between its glassy (low temp, high freq) and rubbery (high temp, low freq) phases. Mass efficiency for viscoelastics have been estimated [58] at approximately 5-10% increase in structural mass per % damping (ie. ζ=0.01) for unconstrained, and 2-5% mass increase per % damping for constrained, while operating in its transition region.

3.2.4 Friction Dampers

The dissipation properties of sliding friction may be exploited with friction tube sleeves or restraining plates in parallel with a load bearing member. This is another nonlinear mechanism, with high potential damping levels approaching 10%. For maximum effectiveness, friction dampers are tuned to a specific forcing level, requiring *a priori* accurate knowledge of the forcing environment. The high performance and mass efficiency offered by friction dampers is offset by nonlinear and uncertain behavior in vacuum and at nanometer displacement levels.

3.2.5 Vibration Absorbers

Vibration absorbers utilize dynamic effects of the vibrating structure to locate or create areas of maximum strain for placement of dissipating materials.

Resonant Dampers

Large strains can be created by adding a secondary spring-mass-damper system to the structure which dissipates energy through its damping element during resonant excitation [14]. Large strains, and therefore dissipation are achieved at a particular frequency to which the secondary system is tuned, up to 5% damping improvement for the targeted mode. Little damping is gained at frequencies below the tuned mode, and residual damping, an order of magnitude below resonant damping, is seen for higher frequencies. Resonant dampers are therefore very sensitive to mistuning and require accurate knowledge of the targeted mode(s) to which damping is prescribed. They are also more effective with increased mass ratio with respect to the structural mass or modal mass at their attach point. Extrapolating experimental results to a space structure [58], a mass penalty of <1% per % *modal* damping (ie. ζ_i=0.01) is expected.

Viscous Dampers

Large strains and strain rates in a vibrating truss structure are found in the joints and in certain, highly stressed members. These are efficient locations for viscous damping devices, which dissipate energy through fluid shear of a viscous fluid, silicon for example, in forced flow during vibration. Damping rate is determined by the dimensions of the damping chamber and the fluid viscosity, and is optimized for the particular stiffness and damping characteristics of a structure. Reasonable broadband behavior over a sensitive frequency range is provided, and linear damping has been shown over micron-range displacements (Honeywell D-struts). Linear behavior has yet to be shown for nanometer displacements, however. Potential contamination and temperature control constraints from the damping fluid must be considered. With continued developments, viscous damping elements, could offer significant structural damping enhancement, as much as 10% or greater, for nanometer precision structures, and little added mass to the system.

3.2.6 Shunted Piezoelectrics

By taking advantage of the mechanical/electrical energy transforming capability of piezoelectric material, dissipative electrical networks can be used to provide structural damping [14]. Through resistive and inductively shunted circuits, solid-state viscoelastic or resonant damping elements are created, with comparable performance to the mechanical equivalents. Electrical shunting is simple to implement, anywhere a piezoelectric can be integrated with the structure, again in areas of greatest strain. And piezoelectrics are relatively temperature invariant, add little mass to the system (a fraction of the equivalent mechanical component), and have good performance at the nanometer level. These devices also carry the limitations of their mechanical counterparts, with relative frequency dependency for viscoelastics, and accurate modal tuning required for resonant dampers.

3.3 Vibration Isolation

Vibration isolation does not attempt to control all spacecraft vibrations, but acts as a local disturbance filter between noisy parts and elements requiring a quiet environment. This indicates that isolation may be implemented either at a disturbance source, to limit vibrations into the global structure, or at the mount of a sensitive element, shielding it from the noisy vehicle. This is achieved through passive and active means, with the general goal to modify the transmissibility, or input-output behavior, of disturbances across this stage. The extreme of isolation is a free-floating element with zero transmissibility at all frequencies. However, system dynamical limitations, the need to pass electrical cabling and coolant lines, and perhaps the requirement to transmit control torques place realistic constraints on this ideal.

3.3.1 Passive Isolation

Passive isolation techniques have as their objective the creation of a dynamical system with transmissibility that is "soft" in the frequency range of the expected disturbances by the addition of passive spring, damper and mass elements to the isolated mass. Figure 3.1 shows typical transmissibility functions for the two types of passive isolation: soft mount isolation and tuned mounts.

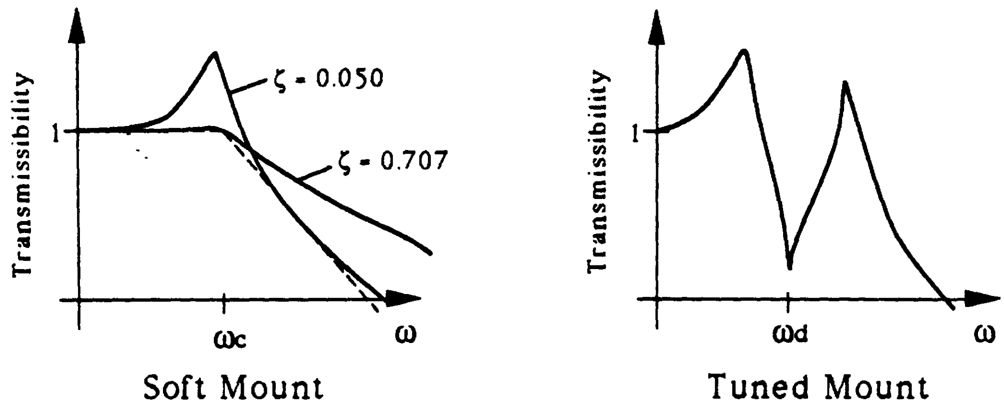

Figure 3.1: Typical Transmissibility Functions for Passive Isolation

Soft Mounts

A passive soft mount is effectively a low pass filter with break frequency at the resonance of the isolated system. At low frequencies, a factor of about 10 below resonance, transmissibility is unity with no attenuation or amplification. For frequencies above resonance, disturbance attenuation is according to the inherent rolloff of the transfer function. However, at resonance, amplification is seen which is dependant on the level of isolator damping. For no damping, amplification is infinite at resonance and the function rolls off at 40dB/dec. Increasing isolator damping lowers this resonant peak, and rolloff flattens toward 20dB/dec. A trade therefore exists between required high frequency attenuation, allowable resonant amplification and low frequency performance, as seen in Figure 3.1 for damping ratios of ζ=0.050 & 0.707. Soft mounts offer simple and reliable operation with proven space heritage, as demonstrated with the Space Telescope reaction wheels [10,15,18], where performance was shown for input amplitudes down to 5 nanometers. Their viscous damping elements, however may be susceptible to leakage and contamination in a vacuum, and developments are required to reach reliable linear behavior at nanometer displacements. A modest mass penalty is also incurred, which is highly dependant upon the application (isolated mass and required corner frequency). The Hubble isolators, for example required approximately 20% additional mass to the reaction wheel assemblies for a 20 Hz corner frequency.

Tuned Mounts

If a single disturbance frequency is particularly troublesome, a tuned spring-mass-damper system can be added to the soft-mount isolation, which introduces a zero into the transmissibility function at the targeted disturbance frequency. Good narrowband performance can be achieved, but is very sensitive to mistuning errors, much like resonant dampers, and adds two resonances to the system.

3.3.2 Active Isolation

If the physical limitations of passive isolation mounts do not permit the necessary transmissibility characteristics, a closed-loop active isolation system may be employed. Information on the sensed force and motion across the mount are used by a feedback control law to drive actuators in the load path to behave like a passive soft or tuned isolator. In this manner, transmissibility may be tailored to cancel disturbance forces in the targeted frequency range. Both active softmount and hardmount isolators are available for confronting various disturbance types. Active soft mounts simulate their passive counterparts, with actuation typically provided by non-rigid mechanical voice coils or magnetic suspension. Rolloff rates as high as 100dB/dec may be designed in the compensation without resonant amplification, but with added complexity and greater mass to the system. Active softmount systems are also generally bandwidth limited to a few to tens of hertz depending on the relative mass of the isolated element.

Hardmount active isolation systems employ inherently rigid actuation, such as piezoelectrics to provide narrowband and possibly broadband disturbance isolation. The narrowband approach uses compensation to implement effectively a notch filter in the transmissibility, targeting disturbances at a specific frequencies [46]. This notch can be fixed for a well "known" disturbance or commanded to track a variable peak through an adaptive network. The narrowband isolator thus requires information on the specific disturbance, and general characteristics of the plant. The broadband approach relies on a detailed model of the structural dynamics in an attempt to zero disturbance transmission over a prescribed frequency band, and is therefore very sensitive to perturbations and uncertainty in the model and the actual plant dynamics. Both of these approaches offer high performance and potential mass efficiency with piezoelectric actuation. But research is still young in this area, and developments are required before a space qualifiable system is available.

3.4 Active Structural Control

Active structural control uses sensors, of sufficient type and sensitivity, to provide information to actuators, of sufficient type and authority, which deliberately modify the properties of the structure [9]. The two major objectives of structural control are to add damping and to maintain a defined position metric through shape control. Structural control is, in general, made challenging by several factors. In addition to their inherent flexibility, large space structures are lightly damped, as previously discussed, and contain high modal density from complex geometry and many, coupled elements. The large number of structural eigenfrequencies also indicates the need for reduced numerical models in order to capture a reasonable bandwidth in the control design. Design of an adequate controller thus not only must rely on a reduced set of modelled modes, but must account for inaccuracies in estimates for the retained modes. Additionally, even if an exact model could be replicated per the engineering drawings, manufacturing, assembly and operational tolerances add up to uncertainty between the actual dynamical behavior and the "exact" model.

3.4.1 Active Damping

The benefits of damping enhancement have been previously discussed, where active damping is an additional tool to the passive techniques. For active damping, the structural control system must sense and feedback velocity to provide rate dependant dissipation in the modelled modes. Active control operates primarily on modes which are most sensitive to the performance metric, and as thus is a more efficient means than passive for providing damping to the important modes. It is inherently more complex, however, requiring the necessary complement of sensors, actuators, electronics and cabling, power and computing capacity, and should be considered after passive means are exhausted. Although, active damping is quite simple to implement once the equipment for a structural (shape) control system is in place.

3.4.2 Shape Control

To control shape, position feedback is used, which effectively adds stiffness to the modelled modes in locations defined by the performance metric. In other words, the disturbances are not permitted to vibrate the sensitive elements (in the performance metric) because actuators are commanded to drive these locations in opposite directions, zeroing the critical displacement. Many control strategies rely on a detailed model of the plant dynamics, and therefore are dependant on accurate state estimation or system identification techniques to provide this information. Other methods attempt to model the uncertainties, or to meet performance without complete dynamical information, and as thus are more robust to potential error sources. Active structural control is an area of current intense research, with significant developments required before actual implementation is realized. The potential performance benefits are tremendous, however, and may enable an even more demanding class of space vehicles.

Chapter 4

Conceptual Design and Modelling of OPTICS

The goal of this chapter is to develop a model point design for illustrating the systems approach for minimizing disturbances: a space-based optical imaging interferometer. This chapter reviews the basic principles of interferometry, derives major mission and system level requirements, describes the conceptual design and operation of the OPTICS vehicle, and formulates a numerical model for use in the following chapter. As is characteristic for the aerospace community, a catchy acronym is required to be able to contend for tax dollars, thus the Orbiting Precision Tetrahedral Interferometric Controlled Structure spacecraft, OPTICS is born. It also permits a degree of brevity.

Many of the future civil space missions envisioned by NASA and the scientific community include instruments requiring large spacecraft configurations with multi-body or slewing appendages, and precision requirements on surface shape and multi-point alignment [28,51]. These have thus been generally chosen as pacing missions for research in controlled structures technology, as they represent missions of current relevance which are potentially enabled or enhanced with CST, and which can subsequently drive the development of this technology. Optical interferometry is chosen as the present focus as a candidate CST spacecraft, based on its precision alignment demands and inherent need for large structural dimensions. Much of the development for the basic tetrahedral interferometer concept was derived from the MIT SERC Interferometer Testbed project, including valuable contributions from those listed in reference[47]. Portions of this work are summarized here, providing the groundwork for design of the OPTICS spacecraft.

4.1 Interferometry

4.1.1 The Basic Interferometer

The fundamental operation underlying the space-based optical interferometer is the creation of an interference pattern from the coherent combination of light samples collected at spatially separated points of a common wavefront. This is illustrated in its simplest 2-dimensional form in Figure 4.1. Light from an interesting celestial object is collected by telescopes at (a) and (b) and sent to the detector at (e) via directing and combining optics at (a'), (b') and (c). The detector, then senses interference intensity fringes from the combined light beams, for extracting the valuable science data. For monochromatic light, the fringes are equivalent bands of light and dark interferences, effectively a sine wave across the detector. However, starlight is composed of many frequencies and therefore the fringes tend to diminish as a sinc function beyond the central fringe, as shown schematically in the figure. It is therefore critical to assure that the two light samples reaching the detector are from the same wavefront, to center the central fringe on the detector. Which is the same as saying that the path from the source through (b), (c) and (e) is equivalent to the path form the source through (a), (c) and (e). Relatively small errors at a fraction of a wavelength in the differential path lengths can produce significant degradation in image intensity, with the wavelength in the optical region approximately 500 nanometers. Typical *total* light pathlength stability goals are on the order of $\lambda/(10-50)$ for these missions. It is this requirement for precise alignments over very large baselines that presents the greatest challenge for an orbiting instrument of this type.

Two basic types of science are extracted from this fundamental operation: astrometry and imaging. Astrometry utilizes a minimum of two collecting telescopes to accurately resolve angular separation of celestial objects, with resolution proportional to baseline (D) and sensitivity along the line between the collectors. Imaging, on the other hand, uses measurements taken at a variety of different baseline separations and orientations to synthesize a large telescope aperture. Fourier domain techniques are utilized to reconstruct an image from the detected intensity profile. There is a great deal more complexity in the actual science of interferometric astrometry and imaging. However, for the fundamental structural control issue, the critical system requirements are for precision alignment. And both types place similar demands on structural stability, however, due to more complex operational needs, interferometric imaging is the primary focus.

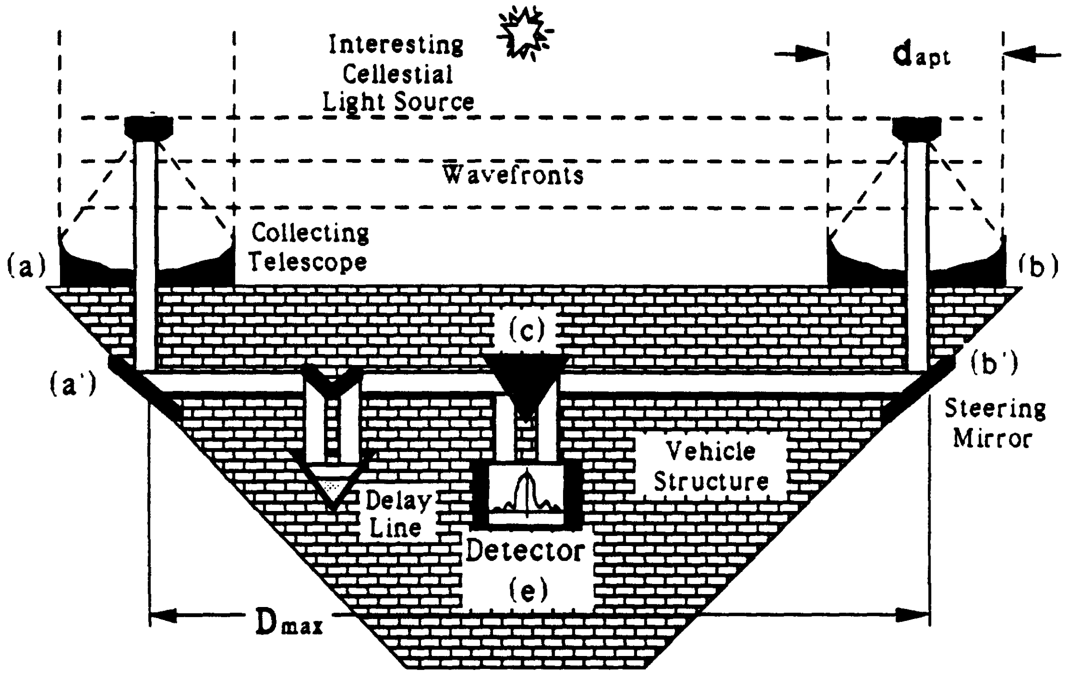

Figure 4.1: Schematic of the Basic 2-Dimensional Interferometer

4.1.2 Basic Relations for Mission Requirements

The top-level system requirements for a space based interferometer may be described with a few simple relations, correlating mission performance to operational and structural demands [47]. Details of the derivations are left out, displaying the principle relations important to the spacecraft system. A more rigorous discussion is included in reference [55] and radio interferometry sources.

Perhaps the most important performance measure for an astronomical instrument is its resolving power, as this determines the maximum angular accuracy for astrometry, and visual resolution for imaging:

$$R = \frac{\lambda}{D_{max}} \tag{4.1}$$

Where λ is the wavelength of light, and D_{max} is the maximum baseline for the instrument. The limit on observable stellar magnitude (M) is defined by the necessary photon flux, from the area of the collecting aperture (A_{apt}), the sampling interval (T_s), and the number of photons (N_{ph}) required for the measurement, by:

$$N_{ph} = A_{apt} \times T_s \times 10^{-0.4M} \times (1.273 \times 10^9) \tag{4.2}$$

For optical imaging, it is assumed that 1 milion photons are required for reliable phase information. This relation indicates that to observe fainter stars requires a larger light bucket, A_{apt}, and/or a greater interval over which photons are collected, T_s. The diameter of the collecting aperture (d_{apt}) also places a limit on the field of view (FOV) of the interferometer:

$$FOV = \frac{2.44\lambda}{d_{apt}} \tag{4.3}$$

For an imaging interferometer, FOV determines the allowable net wavefront tilt error, given scientific constraints on the size of the celestial object which must remain in view at all times. These are the relations which specify the basic instrument performance. As indicated, the principle structural requirement is to maintain precise alignment to assure equivalent paths for the combining light beams. Pathlength errors can be separated, reflecting low and high frequency effects with respect to the sampling interval. Pathlength measurement errors at frequencies less than the inverse of the sample time (1/(10 sec)) produce phase errors in the intensity function. For imaging, this error should be less than $\lambda/20$. Pathlength differences at frequencies above the inverse of the sample time produce a degradation in the measured intensity, by:

$$I_{meas} = \left(1 - \left(\frac{\pi\sigma}{\lambda}\right)^2 \right) \times I_{act} \tag{4.4}$$

Where σ is the RMS pathlength error over the sample interval (T_s). These relations form the basis from which the OPTICS system-level requirements are derived for precision structural stability.

4.2 The OPTICS Spacecraft

The OPTICS spacecraft is an imaging optical interferometer with movable collecting telescopes riding on three legs of a symmetric tetrahedral truss, which capture each of the unique baselines for synthesizing a 35 meter aperture in a stationary vehicle attitude. Each leg, and the maximum baseline are 35 meters long, with spacecraft subsystems, lumped symmetrically at the apexes in a highly modular configuration. The tetrahedral configuration provides several important system benefits in addition to the triangular telescope array. The tetrahedron represents the most efficient use of space for a completely determinate element, and is thus inherently rigid. Its symmetric construction coupled with a balanced layout of spacecraft subsystem elements at the apexes create as isoinertial a structure as is possible for a vehicle of such dimension, limiting the influence of gravity gradient torques on the vehicle. And the measurement of multiple points on the spacecraft to the nanometer level, specifically, the relative displacements of the collectors, requires an out-of-plane, laser metrology reference which the fourth vertex naturally provides.

The spacecraft structure is constructed in low earth orbit (LEO), much as the proposed Space Station structure, with major subsystem modules mounted to equipment platforms forming the apexes. Figure 4.2 is a cartoon of the overall architecture for the OPTICS vehicle, showing baseline subsystem components, the modular construction and general nomenclature used throughout this report.

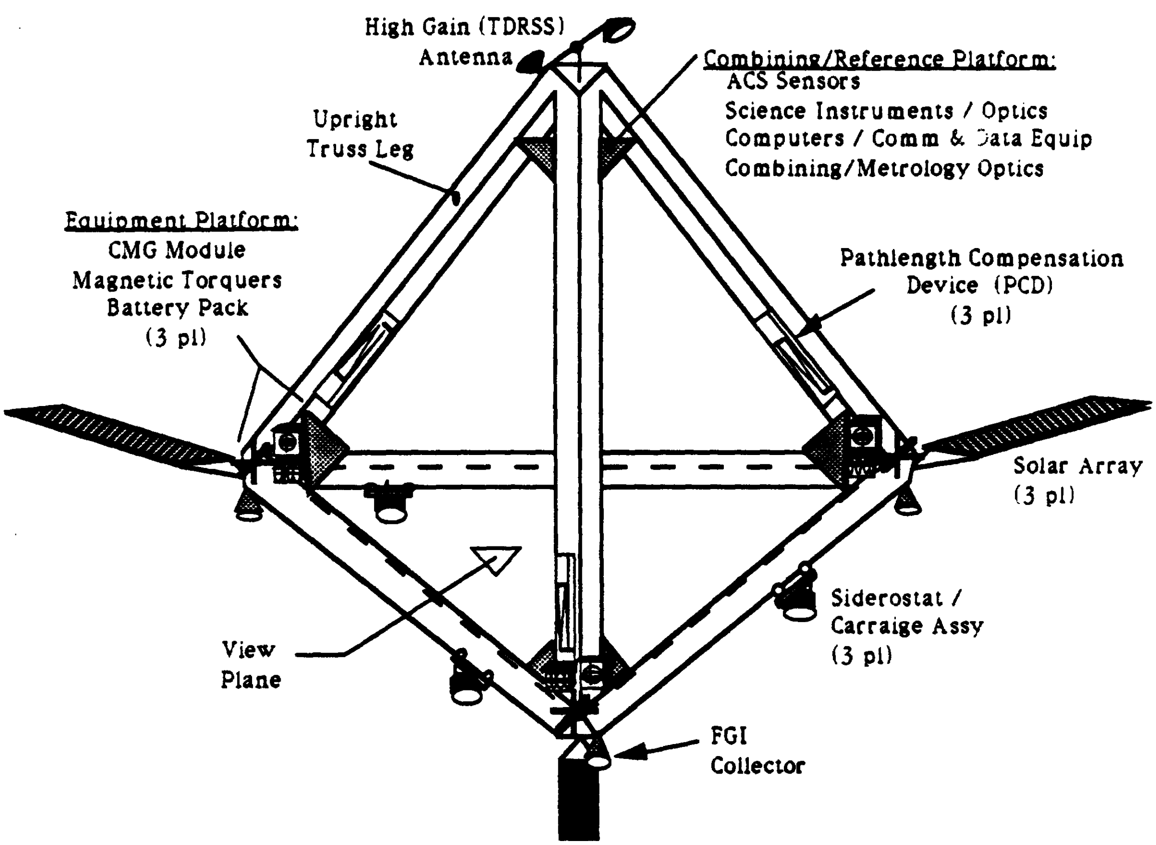

Figure 4.2: Schematic of Overall Architecture for the OPTICS Spacecraft

The overall architecture is driven by the need to mass balance the vehicle, to modularize the assembly of this large spacecraft, and to utilize the dynamically rigid apex "nodes" as a stable mount for sensitive equipment and reduced global disturbance response. A seen in Secition 5.2, the environmental disturbances for OPTICS are relatively large, due to the highly separated geometry. The gravity gradient torques from an inertia imbalance can therefore be quite large if constraints are not imposed on vehicle mass balancing. Therefore, through evaluation of achievable iso-inertialization and the resulting gravity effects, the requirement for equal primary vehicle inertias within $\approx 10^5\ kgm^2$ is levied. This also applies to inertia coupling terms, off-diagonals in the inertia tensor, which must be less than this value. Table 4.1 is a breakdown of first order estimates for major components of OPTICS, showing distribution by subsystem and corresponding mass and power estimates. For the configuration of Figure 4.2 and mass values in Table 4.1, worst-case balancing of tetrahedron apexes is achieved within 650 kg, biased to the top apex, for siderostats midway along their legs. This results in a delta-inertia of $10^5\ kgm^2$, and coupling terms of approximately $10^4\ kgm^2$, both within spec.

This vehicle configuration is adequate to capture the first order dynamical characteristics for evaluation of the effects of disturbances previously discussed. Following, the specific requirements for the vehicle are outlined and error sources are discussed for formulation of an appropriate numerical model and performance metric.

4.3 System Requirements for OPTICS

The underlying purpose of the OPTICS spacecraft in this study is to take a first order cut through the system formulation of an interferometric space vehicle, with typical mission performance, focusing on the critical parameters which make this class of spacecraft unique. Specifically, the requirement for precision alignment, and subsequently, the need for disturbance minimization.

4.3.1 Top Level Requirements

Table 4.2 summarizes top-level requirements for the OPTICS spacecraft, many of which are derived from the preceding basic relations. From Equation 4.1, the required 3 m-arcsec resolution determines the maximum baseline at 35 meters. With a stellar magnitude (M) of 10, and 10^6 photons required for imaging, Equation 4.2 indicates a trade between sampling time and collector area. As will be seen, nearly 2000 samples are required for a "full" image, therefore to limit the net sampling interval, a balance is chosen of 1 meter diameter science collectors and 10 seconds per sample. With this collector a 250 m-arcsec field of view is obtained; thus to capture an object subtending 100 m-arcsec, a net wavefront tilt less than 75 m-arcsec must be maintained. For this imaging instrument, Equation 4.4 provides the fundamental stipulation on pathlength stability. To limit detected intensity, and thus image quality degradation to less than 10%, requires high frequency (>0.1 Hz) pathlength stabilization to 50 nanometers RMS. Whereas, pathlength fluctuations at frequencies below 0.1 Hz need only be *measurable* within $\lambda/20$, or 25 nanometers.

4.3.2 Image Plane Coverage

With this net pathlength jitter budget prescribed, it is appropriate to discuss the basic operation of the OPTICS interferometer and contributing sources to the total error. Three science collecting telescopes, or siderostats[1] are configured in a triangular array in the view plane to map an image in the Fourier domain. To obtain each of the unique baseline vectors[2] required for this U-V plane mapping, the siderostats are permitted to translate along their truss legs, thus eliminating the need to rotate the vehicle and gimbal siderostats over large angles during an image reconstruction. The U-V plane map from this triangular array is a hexagonal pattern as seen in Figure 4.3. Assuming discrete samples of 10 seconds each, as previously shown, each 1 meter diameter siderostat has 35 possible locations along its respective leg. Taking all of the possible combinations for three siderostats with 35 choices shows a great deal of redundancy of unique baseline vectors. Eliminating duplicate pairings and noting the symmetry of the U-V plane, reveals approximately 1800 discrete siderostat baselines are required for a relatively "full" image map. This translates into 5 hours net sampling time per image for continuous science collecting.

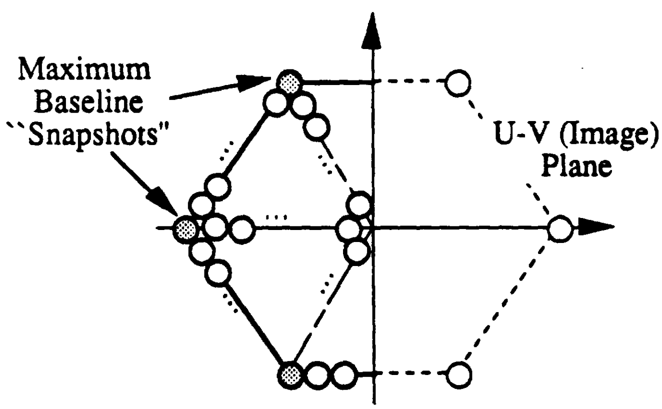

Figure 4.3: Fourier Domain (U-V plane) Mapping From Three Translating Collectors in a Triangular Array.

Operational factors can potentially constrain the available science time, such as earth obstruction in LEO, time required to slew the vehicle to a new target, time allotted for repositioning of siderostats and time required for transient vibrations to settle within

[1]The word *siderostat* is used here to include the entire science collecting telescope assembly, although the collector for OPTICS does not necessarily require a steering mirror, or siderostat.

[2]The baseline vector includes the distance between collecting telescopes and the orientation of a line joining their midpoints with respect to the celestial object

acceptable levels. Given an accessible low earth altitude, the mission must design around constraints due to earth shielding. And, as seen in the next chapter, the maximum vehicle slew rate is limited by ACS actuator demands to $90°/60\text{min}$. Beyond these constraints, and to allow maximum (100%) science time, requires operation of the instrument in the face of moving siderostats and transient vibrations. This also presents a greater challenge to the disturbance minimization system, and is therefore adopted as the baseline approach. The nominal imaging scenario, then, is a situation in which two of three siderostats are operated in science collecting mode, while the third is repositioning itself for the next discrete sample. This sequence continues, alternating collecting and translating siderostats, throughout the net 5 hour sample interval. To avoid constraining science time, each siderostat translation, of 1 meter nominally, must be performed within the sampling interval of 10 seconds. As shown in Chapter 5, this imaging approach also places severely challenging requirements on the necessary disturbance minimization effort.

4.3.3 Pathlength Error Sources

The two dimensional interferometer schematic of Figure 4.1 is used to illustrate the basic contributors to the net pathlength error which must be controlled to 50 nanometers RMS for quality imaging. Three primary error sources exist as the photons make their way from the source, through the collectors, off of steering and combining optics to the detector:

- External Rigid Body
- Internal Flexible - Local
- Internal Flexible - Global

External rigid body errors, as the name implies, arise from attitude variations of the entire vehicle which tend to turn one collector closer to the source, modifying the relative pathlengths. Even if the spacecraft were completely rigid, these errors would exist due to attitude control limitations. The other two types of error are generated from elastic deformations on and within the vehicle. Local internal flexible errors are caused by the localized vibration or deformation of components which directly impact the light path. These could be the vibration of a steering mirror, or thermal deformation of an optical surface, where, on a large vehicle like OPTICS, there are potentially many reflecting interfaces between the siderostat and detector. Finally, the global flexible errors result from a gross deformation of the spacecraft structure, affecting both the internal light path through relative motion between reflecting surfaces, and the projected baseline vector.

Chapter 5 discusses how these errors apply to the 3-dimensional OPTICS interferometer, and the means for precision measurement of each of the contributing elements with laser metrology.

Because there are many sources of potential disturbances, as discussed in Chapter 2, the net pathlength error budget of 50 nanometers RMS must be divided such that the total error with all sources active will not exceed the specification. This should also include adequate margin for contingency, as they have found out with Space Telescope. This so called jitter budget for a precision vehicle is a highly iterative specification dependant on the net spectrum of potential contributors for a specific complement of subsystems and equipment. Where the total budget is dished out to each error source based on their relative magnitudes and performance sensitivity [10,11,15,43]. However, the present investigation shall budget 10 nanometers RMS per source as characteristic of performance levels for these instruments. With this budget, the spacecraft can manage 25 uncorrelated disturbance sources producing 10 nanometers RMS degradation each (RSS), which is not unreasonable for the large OPTICS spacecraft.

4.4 OPTICS FE and System Modelling

Figure 4.4 shows the overall architecture of the modelling approach used for the OPTICS system. Design of the truss structure, and characteristic mass and inertial properties for subsystem components are utilized to formulate a finite element (FE) approximation of the structural "plant". A reduced set of modeshapes and eigenfrequencies are then available for a modal state-space representation.

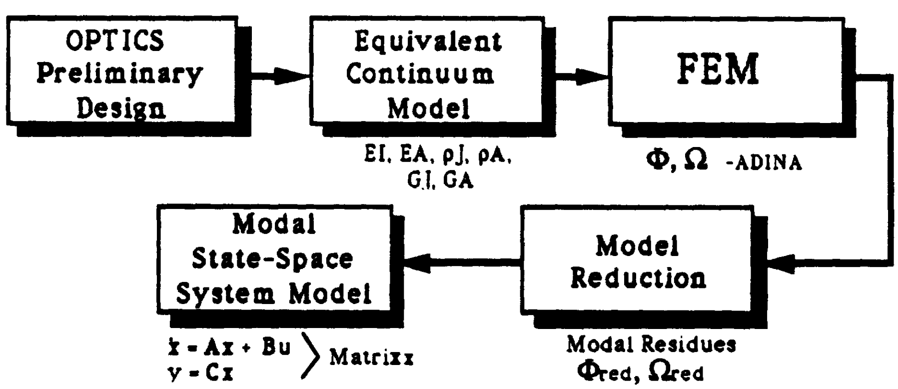

Figure 4.4: OPTICS Modelling Flow Diagram

4.4.1 Structural Design

The structural design of the OPTICS vehicle is a scaled version of the SERC testbed truss structure [47], with re-sized sectional properties and greater mass efficiency for reduced space loads, approximating the Space Station truss members. The tetrahedron is formed from six equivalent truss "legs", each with an overall length of 35 meters and triangular cross section at 2.5 meters on a side. Figure 4.5 shows the truss structure design for the OPTICS tetrahedron. Each leg is constructed from 14 equal truss bays of nominally 9 struts in a determinate pyramidal lacing, 2.5 m nominal length per strut, 3.5 m for diagonals. Struts are modelled after the Space Station design, of 2 in dia (50.8 mm) graphite epoxy tubes, 0.060 in (1.52 mm) wall, with the NASA/LaRC quick-connect end fittings and corresponding attach nodes. Mass properties for struts and nodes, and element count are seen in Table 4.1.

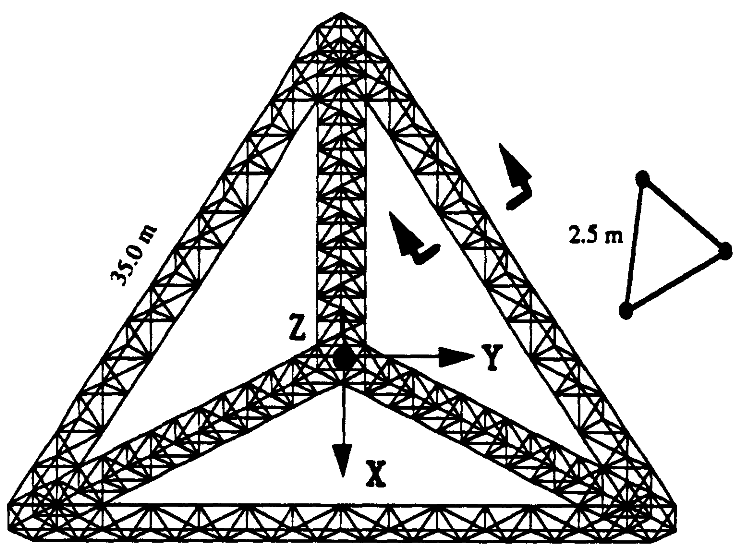

Figure 4.5: Tetrahedral Truss Design of the OPTICS Spacecraft

4.4.2 Finite Element Model

A finite element model for the OPTICS vehicle is formulated to estimate eigenfrequencies and modeshapes of the structural plant for incorporation into the modal system model in the following section. The complete OPTICS truss includes 696 truss members and 228 nodal joints in the symmetric 6 leg tetrahedral configuration. It is therefore inappropriate to model the dynamics of the structure to this localized level of detail for a preliminary investigation as this. Thus, an equivalent continuum modelling approach is used, where the repeating bay elements of the truss legs are approximated as Timoshenko beam elements[3] for incorporation into a global finite element model. The continuum approach used here is adopted from the preliminary SERC testbed FE modelling of Leonard Lublin and Ron Spangler [47], which utilize the equivalent modelling method discussed in [53,9].

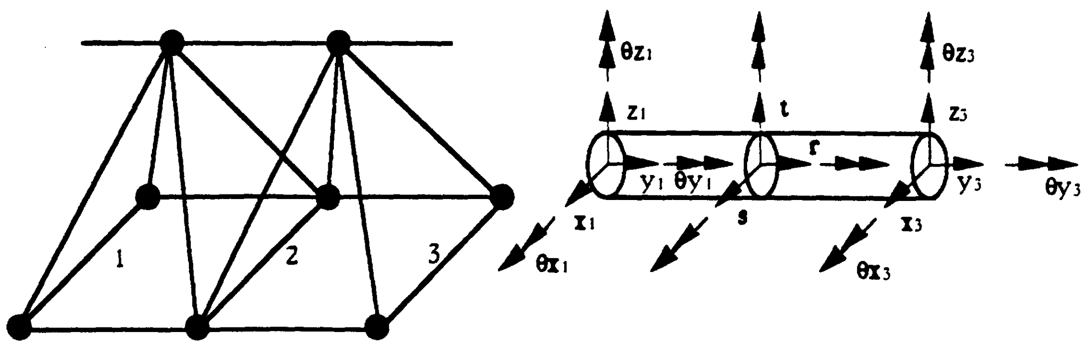

Figure 4.6: Repeating Truss Section and "Equivalent" Beam Elements

Figure 4.6 shows the repeating truss section and "equivalent" Timoshenko beam element. The basis for the continuum approximation follows that equivalent sectional and elastic properties can be inferred from calculations of deformations for the repeating truss section to known loads applied in an appropriate manner, assuming a linear model. This permits estimates for EA, EI_{ss}, EI_{tt}, GJ, GA_s, and GA_t according to the fundamental relations in Figure 4.7. A simple FE representation of the repeating section, with appropriate end and loading conditions, provided deformation data from the applied loads. Equivalent mass and rotational inertia per unit length, ρA and ρJ respectively, are also approximated by evaluating these properties as a function of distance along the truss section, and averaging over the length of the element.

Table 4.3 lists the resulting equivalent properties from this continuum approach. By assuming a Young's modulus (G/E: $2.76x10^{11}$ N/m^2), values for all of the variables are available for input into the ADINA finite element program. Note that the resulting constitutive values do not necessarily correspond to a physically realizable structure, but this permits a simple means to *coax* the ADINA program into believing it is handling the OPTICS tetrahedral truss. The global FE model is then constructed from 14 equivalent elements per truss leg, with end conditions at the apexes simulated by connecting simple strut elements between the second to last nodes of each leg. The net model, then has 84

[3] 12 DOF beam elements: 2-axis bending (θ_s, θ_t), shear (x_s, x_t), axial (x_r) and torsional (θ_r) degrees of freedom

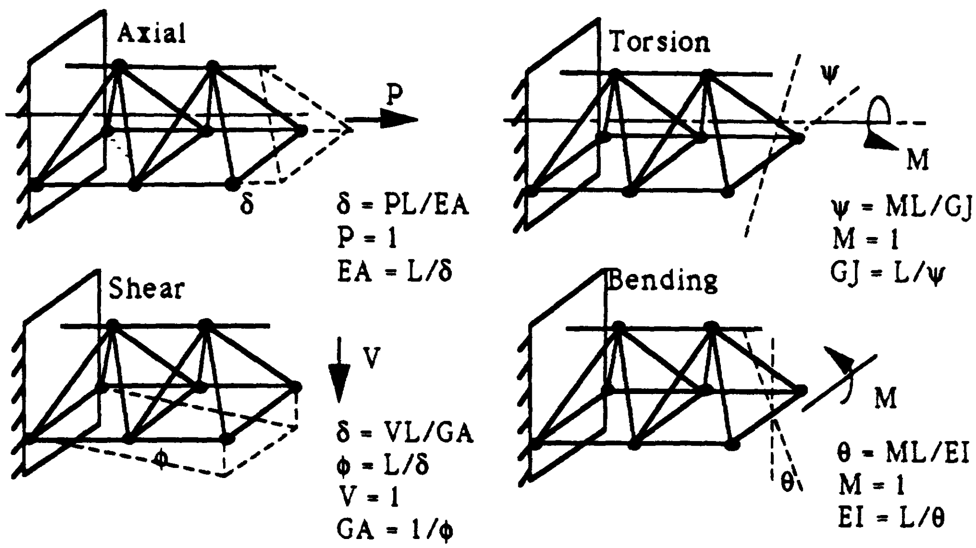

Figure 4.7: Equivalent Property Relations for EA, EI, GJ, and GA

equivalent Timoshenko beam elements, 12 strut elements and 82 nodes, for a total of 492 degrees of freedom (3 displacements and 3 rotations at each node).

Comparison of the measured fundamental frequency of the SERC testbed with that estimated from a similar equivalent model, show the continuum model with end conditions over-stiffens the approximation, in this case from 31 Hz measured to 45 Hz estimated. The simplified end conditions and neglected bending-twisting coupling effects in the equivalent approximation are believed to be the major sources of error. Nonetheless, they are of comparable orders of magnitude, and the continuum model shall suffice to investigate the global dynamics in this preliminary investigation.

Characteristic lumped masses from Table 4.1, and significant inertias (solar arrays), are included in the model at nodes corresponding to subsystem locations defined by the preliminary vehicle architecture discussed previously. Figure 4.8 displays the resulting eigenfrequencies for this configuration, with 94 flexible modes between 0.6 and 37.7 Hz. The bending fundamental of a typical truss strut (3.5 m) is estimated to be on the order of this upper frequency bound, thus the model is limited in this frequency range, but only borders on the local dynamics. These eigenfrequencies and corresponding modeshapes represent the structural plant for use in a modal state-space representation of the system.

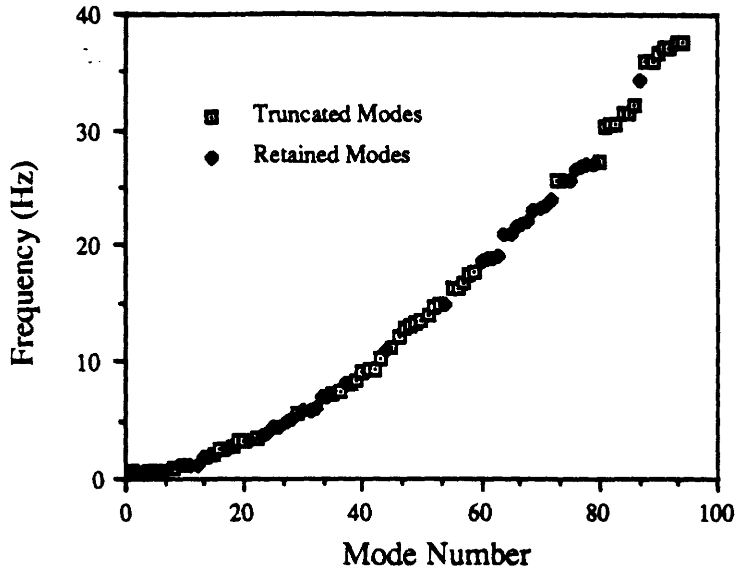

Figure 4.8: Eigenfrequencies of the Equivalent OPTICS Model Showing Truncated and Retained Flexible Modes.

4.4.3 System Model

Information from the ADINA finite element model permits a modal formulation of a state-space system for the input-output behavior of the OPTICS spacecraft, where the outputs correspond to the vehicle performance metric, pathlength errors, and the inputs include control effort and disturbances. A brief derivation of the system model is discussed, whereas a more rigorous treatment may be found in [25].

The generalized form of the undamped system may be written as:

$$M\{\ddot{q}(t)\} + K\{q(t)\} = \{Q(t)\} \tag{4.5}$$

Where the mass and stiffness matrices, M and K, are computed in the FE routine from geometric and physical properties included in the input file. Solution of the generalized eigenvalue problem, with $\{Q(t)\}$=0, gives:

$$M\Phi\Lambda = K\Phi \tag{4.6}$$

With Φ the modal matrix, and Λ the eigenfrequencies available as the FEM output. Here, Φ and Λ are mass normalized by:

$$\Phi^T M \Phi \;=\; I \tag{4.7}$$

$$\Phi^T K \Phi = \Lambda$$

The mass-normalized modal matrix then permits a transformation between generalized physical coordinates, $\{q(t)\}$, and modal coordinates, $\{\eta(t)\}$, according to:

$$\{q(t)\} = \Phi\{\eta(t)\} \tag{4.8}$$

Substitution of Equations 4.7 and 4.8 into Equation 4.5 gives the system of differential equations in modal form:

$$\{\ddot{\eta}(t)\} + \Lambda\{\eta(t)\} = \Phi^T\{Q(t)\} \tag{4.9}$$

A state-space representation may now be formulated, with the basic form:

$$\{\dot{x}(t)\} = A\{x(t)\} + B\{u(t)\} \tag{4.10}$$

$$\{y(t)\} = C\{x(t)\} + D\{u(t)\} \tag{4.11}$$

Substitution yields:

$$\begin{aligned} \begin{bmatrix} \{\dot{\eta}(t)\} \\ \{\ddot{\eta}(t)\} \end{bmatrix} &= \begin{bmatrix} 0 & I \\ -\Lambda & -2\zeta_i\omega_n \end{bmatrix} \begin{bmatrix} \{\eta(t)\} \\ \{\dot{\eta}(t)\} \end{bmatrix} + \begin{bmatrix} 0 \\ \Phi^T \end{bmatrix} \{Q(t)\} \\ \{y(t)\} &= C \begin{bmatrix} \Phi & 0 \end{bmatrix} \begin{bmatrix} \{\eta(t)\} \\ \{\dot{\eta}(t)\} \end{bmatrix} \end{aligned} \tag{4.12}$$

Where the outputs, $\{y(t)\}$, are in physical coordinates and are defined by the matrix, C, which defines the performance metric from the physical degrees of freedom of the structure. The modal damping term, $-2\zeta_i\omega_n$, was inserted at this point to simplify the derivation, where ζ_i, the modal damping ratio, is used as the damping variable in Chapter 5. Introduction of this modal damping term assumes that the added damping does not change the modes significantly. This assumption tends to break down at damping levels much above 10%, where the model must be reformulated to include damping terms from the outset. With the parameters in Equations 4.12 obtainable from the FE model, and specification of a suitable output matrix, C, differential pathlength response to an arbitrary forcing (disturbance), $\{Q(t)\}$, may be obtained.

The performance metric is the differential pathlength error between two science star light paths. Since flexible response is of primary concern here, rigid body modes are not included in the model, and performance is defined as the difference in two internal paths. Each of the three internal paths include the net distance along one view-plane and one upright tetrahedral leg. The differential pathlength error used here, therefore, becomes a linearized combination of the apex nodal displacements, which define the net flexible behavior of each leg. This is taken to be representative of the precision alignment task for the OPTICS interferometer.

Computational limitations restrict the FEM solution to 100 modes, 6 rigid body modes and the 94 flexible modes in Figure 4.8. Although this places an upper bound on the model bandwidth at 38 Hz, it also proves to be unwieldy to carry the computational burden of 94 modes with various levels of sensitivity with respect to the performance metric. Thus, model reduction is in order. Because this investigation is preliminary in nature and does not address structural control strategies, a rigorous model reduction is not imperative. Therefore, the model is truncated to a set of 50 modes selected through an evaluation of the residues from a transfer function between a characteristic disturbance input to the differential pathlength error. The distribution of retained and truncated modes is seen in Figure 4.8, which indicates the frequency regions of greatest sensitivity.

The nominal OPTICS model, then used in the following chapter to investigate open loop response to characteristic disturbances contains 50 modes with frequencies between 0.62 and 37.7 Hz. No rigid body dynamics are included in the model, and 0.1% modal damping is assumed for all modes, the "undamped" model.

Table 4.1: OPTICS Spacecraft Component Breakdown

Component & Description:	Quantity	Mass (kg) Unit	Mass (kg) Total	Avg Power (W) Unit	Avg Power (W) Total
Structure					
1. Primary truss: (G/E; S.Station-type)	1		**2740.0**		---
2.5 m strut (2 in dia, .060 wall)	624	3.5	2184.0	—	
3.5 m strut (&end ftg's)	72	3.9	281.0	—	
nodes (NASA/LaRC)	228	1.2	275.0	—	
2. Siderostat Carraige & rail struct:		150.0	**450.0**		---
3. Trombone sprt & rail struct:	3	50.0	**150.0**		---
4. Antenna support: (COSMIC)			**50.0**		---
5. Secondary structure:(assume 20% truss)			**550.0**		---
ACS					
1. CMG:			**1230.0**		**700**
Sperry M-1700	3 (1/axis)	155.0	465.0	75	225
2. Magnetic Torquers:					
Ithaco (3in dia, 100 in long,4000 Am**2)	12 (4/axis)	50.0	600.0	20	240
3. Sensors & Electronics:			165.0		235
Sun, FHST,Rate gyro,Magn't,FGI					
Power			**869.0**		
(5 kW load + batty's - 400km, 28.5 deg orbit)					
1. Solar Arrays: (~15 kg/kW)	3	76.0	228.0		**(13.3 kW)**
15 kW rating (2.5m X 18.0m ea)					(BOL)
2. Batteries: (Ni-H2; 30 Wh/kg; 60 A-hr; 25%dod)		45.0	136.0		
3. S/C Harness: (power/signal cable)			400.0		
4. Pwr Electronics (~8 kg/kW):			105.0		
Mechanisms					
1. S/A drives (~4 kg/kW):	3	20	**60.0**	10	**30**
2. Siderostat Trolleys:	3	50	**150.0**	25	**75**
3. Trombones (delay lines trolleys):	3	20	**60.0**	5	**15**
2 Science / 1 Guidance					
4. Antenna drives:	2		**63.0**	5	**10**
Comm/Data/Tele					
1. Computers:			**140.0**		**280**
RT Struct Control & Metrology	1		50.0		100
Data mgmt	1		50.0		100
Comm & bus	2	20.0	40.0		80
2. Antennae (2 HGA/ 2 LGA):			**8.0**		---
3. Comm & Data Equip:			**222.0**		**320**
Optics & Scientific Equip:					
1. Science Siderostats:	3		**585.0**		
3 X 1.0 m mirrors (HST scaled: 166kg/m**2)	3	130.0	390.0		
struct, gimbal, etc (assume 1/2 mirror)	3	65.0	195.0		
2. Guidance Siderostats:	2	30.0	**60.0**		
2 X 0.5 m mirrors (166 kg/m**2)					
3. Metrology system:			**155.0**		**1500**
Lasers	8	10.0	80.0		
Collectors (assume zygote-type)	12		25.0		
Mirrors, elec., etc.			50.0		
4. Secondary mirrors,misc optics & elec.:			**100.0**		
5. Scientific Instruments:			**500.0**		**750**
Thermal (Blankets, coatings, heaters,...)			**420.0**		**500**
SUM: (With ~25% Contingency)			**10,700 kg (23,550 lb)**		**5000 W**

Table 4.2: Top-Level OPTICS System Requirements

Science Mission Requirements:	
Orbit:	400 km; 28.5°; 93 min Period
Cellestial Coverage:	Full Sky in 6 Months
Optical Interferometer:	3 milli-arcsec Imaging
Imaging:	Full (100%) U-V Plane Coverage
	90% Image Quality
Stellar Magnitude (M):	10
Science View Time:	Uninterrupted (100%)
Optical Wavelength (λ):	500 nanometers (avg)
Structural Requirements:	
Net Pathlength Error Budget:	50 nanometers RMS (>0.1 Hz)
Low Frequency PL Errors:	Measure to 25 nanometers (<0.1 Hz)
Net Wavefront Tilt:	75 milli-arcsec
Transient Pathlength Errors:	Settle to 10 n-m within 10 sec
Vehicle Principle Inertias:	Equal Within 10^5 $kg\ m^2$
Metrology Requirements:	
Internal Pathlength Monitoring	
Siderostat and FGI Baseline Monitoring	
Laser Measurement:	1 nanometer Accuracy
Attitude Control Requirement:	
Spacecraft Slew:	90°/60 min or less
LOS Accuracy:	0.01 to 0.10 arc-sec
LOS Stability:	0.001 to 0.010 arc-sec
Power Requirement:	
Average Power:	5 kW (EOL)

Table 4.3: Summary of Strut and Truss Equivalent Properties

Property	*Value*	*Units*
Struts:		
(L) Length	2.5 / 3.5	m
(M) Mass	3.5 / 3.9	kg
(d, t) Section	2.0 (50.8) dia	in (mm)
	0.060 (1.52) wall	in (mm)
(E) Modulus of Elasticity	2.76×10^{11}	N/m^2
(r) Density	1744	kg/m^3
(I) Inertia (Bending)	7.15×10^{-8}	m^4
(J) Inertia (Polar)	1.43×10^{-7}	m^4
Nodes:		
(Mn) Mass	1.2	kg
End Fittings:		
(Mf) Mass	2.5 (/strut)	kg
Equivalent Elements:		
(EA) Axial Stiffness	2.66×10^8	N
(EIss) Bending Stiffness (s-dir)	4.00×10^6	$N\ m^2$
(EItt) " (t-dir)	2.79×10^6	$N\ m^2$
(GJ) Torsional Stiffness	1.64×10^7	$N\ m^2$
(GAs) Shear Stiffness (s-dir)	1.27×10^8	N
(GAt) " (t-dir)	8.05×10^7	N
(ρ A) Mass / Length	2.69	kg/m
(ρ J) Inertia / Length	0.43	$kg\ m^2/m$
(E) Modulus of Elasticity	2.76×10^{11}	N/m^2

Chapter 5

CST Spacecraft Subsystem Design

The purpose of this chapter is to investigate the design of primary spacecraft subsystems with respect to minimizing disturbances inherent to major subsystem elements, and the effects of these disturbances on the system performance metric. Three spacecraft subsystems are investigated in detail, characteristic of design for major system elements and representing the largest disturbance generators on the vehicle. In the first two sections, options for Power and Attitude Control Subsystems are evaluated; candidate elements are designed; performance response to specific disturbances are obtained; and methods for meeting subsystem performance are presented. The following section looks at elements of the OPTICS Interferometer &Metrology Subsystem as potential disturbers, evaluates performance degradation from these effects, and suggests measures for meeting specification. The chapter formulates a set of criteria and recommendations for design of each subsystem toward reducing these disturbances and their effects to levels consistent with the performance requirements for OPTICS, and provides data and motivation for the formulation of a general systems approach to disturbance minimization outlined in the following chapter.

5.1 Power Subsystem

This section investigates the design of a power subsystem for OPTICS as it relates to minimization of the disturbances and their effects which are inherent to power subsystem elements, and interactions with the flexible control of this large precision space structure. The power subsystem is responsible for providing electrical power to the vehicle throughout the mission lifetime, including capacity for storing energy for periods of eclipse or emergency, power conditioning, regulation and distribution to all spacecraft loads. Figure 5.1 is a simplified block diagram showing the major elements and top-level functional architecture for the power subsystem.

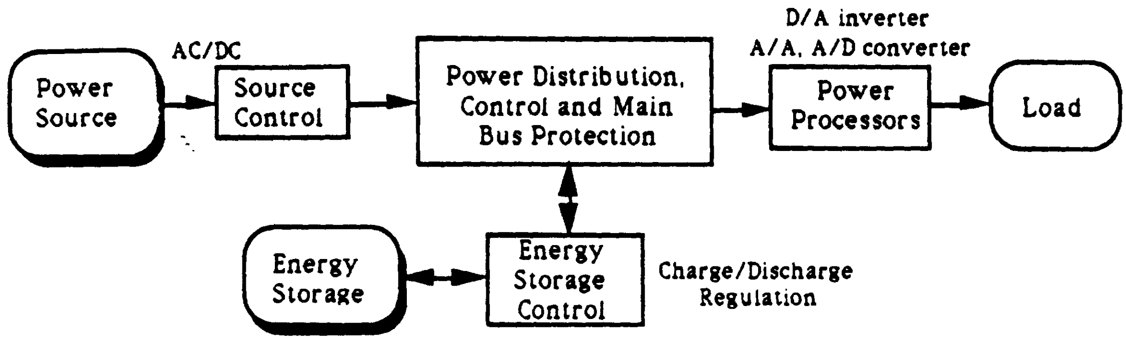

Figure 5.1: Power Subsystem Functional Block Diagram

Many key system level trades center around such power subsystem issues as the electrical bus architecture, regulated vs. unregulated power, centralized vs. distributed conditioning, and the wiring harness design and layout. However, this investigation is concerned primarily with the more mechanical and dynamical aspects of the power subsystem which tend to drive the interactions with large flexible space structures and the structural control system. The focus is therefore on the highlighted boxes in the block diagram: power sources and energy storage, where appropriate.

As a first step for investigating the power generation and storage options, the primary system design drivers are identified. Table 5.1 lists the major system requirements imposed on the power subsystem.

Table 5.1: Power Subsystem Requirements

Power Requirements:	
Avg Power Load:	5 kW
Orbital Altitude:	400 km nominal
Inclination:	28.5°
Period:	93 min
	(57 min sun / 36 min eclipse)
Structural Requirements:	
PL Jitter Budget:	10 nano-meters RMS
Transient Vibrations:	Settle to 10 n m in < 10 sec

Orbital parameters come directly from the mission requirements, and are critical mainly for solar power sources and those with large area components (eg. atmospheric drag).

Table 5.2: Interferometer Power Budget

Subsystem	*Avg Power (W)*
Attitude Control	700
Communication and Data Management	600
Scientific Instruments	130
Mechanisms	750
Thermal Control	500
Metrology and Optics	1500
CST	500
TOTAL (incl. contingency)	$\approx$ 5 kW

The average power load is derived from preliminary estimates of power consumption for the major components of OPTICS, as seen in Table t-comp. A summary of the power budget by major subsystem is shown in Table 5.2. The budget includes power for a Space Telescope complement of scientific instruments, scaled by 50% to reflect a more demanding scientific spacecraft. Also in the table is power budgeted for the CST subsystem elements. The power required for this equipment is generally low, however 500 Watts is allocated based on an estimate for a reasonably active structural control system consisting of 2 active truss bays per leg, 36 active struts, distributed sensors, a dedicated processor and associated electronics. Also note the high level of power budgeted for the laser metrology system required to drive the frequency stable gas lasers.

5.1.1 Power Generation and Storage Options

This section discusses suitable options and the rationale for selection of power generation and energy storage elements meeting the above listed requirements. In addition to fundamental system criteria, such as: performance, mass, cost, reliability, etc., the parameters of greatest concern for a CST vehicle with respect to power design are the disturbances brought to the system, how these disturbances are manifest in the form of performance degradation, and the dynamical interactions with the system "plant". Disturbances are discussed in detail in Chapter 2, and are quantified for this subsystem following selection of candidate options. Certainly, those options which are inherently "quieter" are more

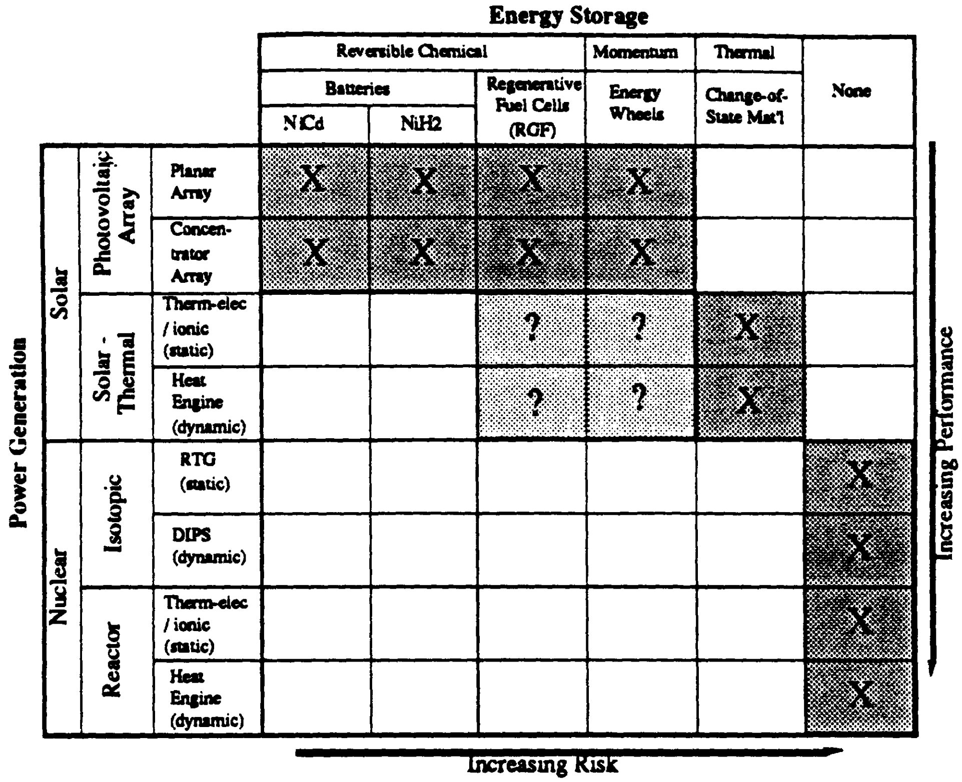

Figure 5.2: Potential Power Generation and Energy Storage Options Showing Appropriate Combinations.

desirable, assuming they pose no adverse design considerations. However, the manner in which the component is physically integrated with the spacecraft, ie. how the disturbances couple in with the plant dynamics, is the more demanding issue, as this determines how the disturbances may be dealt with. Also, the physical properties of the subsystem elements and integration with the system influence the net dynamical properties of the vehicle.

Many options exist for the generation and storage of electrical power for the demands placed by the OPTICS system [41,57]. It is assumed that the technology choices for OPTICS will be made within the next 5-10 years. Thus, a somewhat reduced set of candidate technologies are considered. Combining the generation and storage options into a matrix, as in Figure 5.2 [41], it is evident that only certain combinations are appropriate. The figure shows the major combinations organized by technology, and arranged from lowest to highest potential power output performance. This same arrangement also corresponds to a matching progression from lowest to highest risk to the mission, as currently envisioned.

The primary candidates are thus: solar photovoltaic or thermo-electric systems. The photovoltaic or solar arrays (SA) may be planar or concentrator-type which track the sun for direct solar-to-electric conversion. These must be combined with batteries, regenerative fuel cells (RGF) or flywheels for energy storage. Thermo-electric systems, on the other hand, range from solar-thermal to nuclear-thermal heat sources, coupled with a static (thermo-electric / thermionic) or dynamic (heat engine) thermal-to-electric energy converter. Solar dynamic systems will most likely use thermal storage in phase-change (latent heat) materials during eclipse. And nuclear power sources, not relying on the sun, do not require energy storage.

Table 5.3 is a summary of the primary options and associated performance parameters, disturbance types, physical / dynamical characteristics and additional CST - power subsystem considerations. Clearly, each of the options can meet the modest power requirements for OPTICS. A nuclear reactor, however is beyond the power regime of this vehicle, has a high specific mass (kg/kW) for this power range, and a radiation fluence which may generate unacceptable doses to sensitive electronics over the 10 year life [60].

Selecting a power subsystem with minimal vibrational input primarily means selecting the system with the least amount of moving elements, and that which does not introduce significant individual dynamics. A photovoltaic system is a good candidate as a minimal disturber, functioning passively except to track the sun during a vehicle maneuver. Photovoltaics are by far the most developed of the power technologies, and with projected improvements in array efficiency, radiation tolerance and structural technology, will remain a competitive choice up to the 100 kW range. To the first order, a solar concentrator is similar for a photovoltaic or a solar-thermal system: both require smaller arrays, roughly 1/3 the area of a planar array, but pose greater geometric and optical stability constraints. For example, solar concentrators require $0.1° - 0.7°$ pointing stability versus a few degrees at best for planar arrays.

For solar-electric storage, batteries provide the obvious choice, based on their proven heritage and benign operation. Regenerative fuel cells and, more so, energy flywheels are potentially more mass efficient and can provide auxiliary benefits as well[1]. However, their operation generates mechanical vibrations: pumping and flow noise for reactant supply to electrolyzer-fuel cell systems, and electromechanical flywheel disturbances, similar to ACS actuators. The primary constraint on batteries is their limited lifetime in low earth orbit, with over 5500 charge/discharge cycles per year. But, short of any flight heritage and new technical developments, the other options cannot currently promise superior life

[1]Eg., it is possible to use energy flywheels as ACS actuators.

performance.

A desire to eliminate the storage requirement leads to another highly passive power option: the radioisotopic thermoelectric generator (RTG) with a static thermo-electric or thermionic converter. Natural radioisotopic decay, of Plutonium-238 for example, provides a heat source for the thermal-to-electric conversion process. The only potential disturbing elements in this system are the transport of coolant fluids for dissipating the large amounts of thermal energy associated with inefficient static conversion (10-15% max). A thermodynamic heat engine (eg. Rankine, Stirling, Brayton) offers much better conversion performance for an isotopic heat source [4], up to 3 times more efficient, but holds the potential for larger disturbances due to the inherent rotating and pumping engine equipment, and high rate transport of the working medium.

Based on these criteria, and in order to explore the essential CST - power subsystem interactions, two of these design options are thoroughly investigated: the photovoltaic-battery and radioisotope thermoelectric generator (RTG) systems.

5.1.2 Power Subsystem Preliminary Design

Utilizing the performance parameters from Table 5.3 and first order design techniques, preliminary sizing of SA-battery and RTG-thermal power subsystems are derived. A summary of the resulting system parameters is displayed in Table 5.5, and Figures 5.3 & 5.4 shows the vehicle layouts for solar photovoltaic and RTG power subsystems.

Photovoltaic

The first cut architecture has the SA-battery system evenly distributed at the apexes of the three view-plane legs. Solar array's extend outward from the apex with their long, rotational axes in the view plane, normal to the opposing truss leg (see Figure 5.3).

In this arrangement, with a single gimbal axis, the SA's have a worst-case sun angle[2], θ_S, of 35° (82% efficiency), with the view axis[3] 180° to the sun line. However, the arrays are sized for the extreme case of a 90° view angle, with two arrays operating at 87% (θ_S = 30°). For any pointing angle, then, the vehicle attitude must be such that any two arrays are equally illuminated, with equivalent gimballing. Thus, the third array acts primarily for system redundancy. Introducing a second array gimbal axis reduces the required array area and mass by ≈13%, only half the mass of the additional gimbal

[2]The cosine of the sun angle (θ_S) approximation for illumination efficiency is valid up to ≈ 45°.

[3]The view axis is defined as the line normal to the view plane.

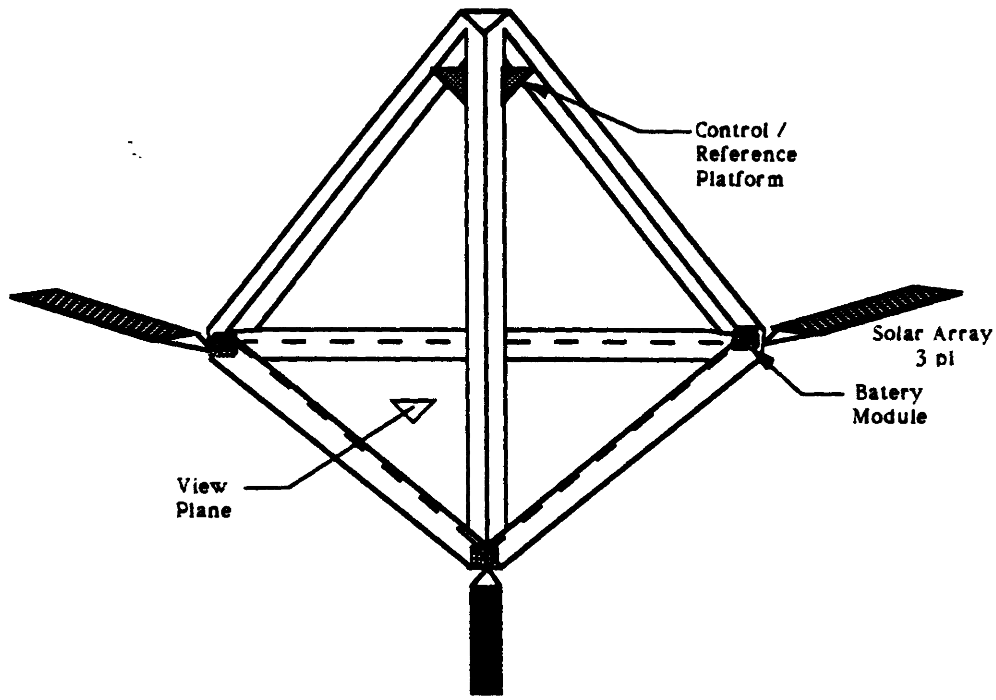

Figure 5.3: Solar Array - Battery Power Subsystem Layout on the OPTICS Vehicle.

mechanism, but with added complexity. Thus, a single axis is maintained. An alternative configuration has the arrays mounted with their short axes gimballed, 90° from the nominal orientation. This yields an arrangement and sizing equivalent to the Space Telescope SA's. No major benefit exists for this orientation, therefore the baseline configuration is used to minimize potential interactions from array inertia about the torque axis. However, data from the HST SA's will be used as a worst- case scenario for tracking slew and interaction torques [52].

RTG

The RTG system is also designed to be located equivalently in three distributed vehicle locations, as seen in Figure 5.4. Each module consists of approximately five 350 W RTG generating units, static conversion components, electronics and planar radiators. Note that this system requires roughly 1/3 of the basic power processing and conditioning electronics, due to the lack of storage and high power processing that a solar array must contend with.The system does suffer, however, from the requirement for large radiators to dissipate the 41 kW_{th} of power from the inefficient conversion process, and an overall greater system mass contribution.

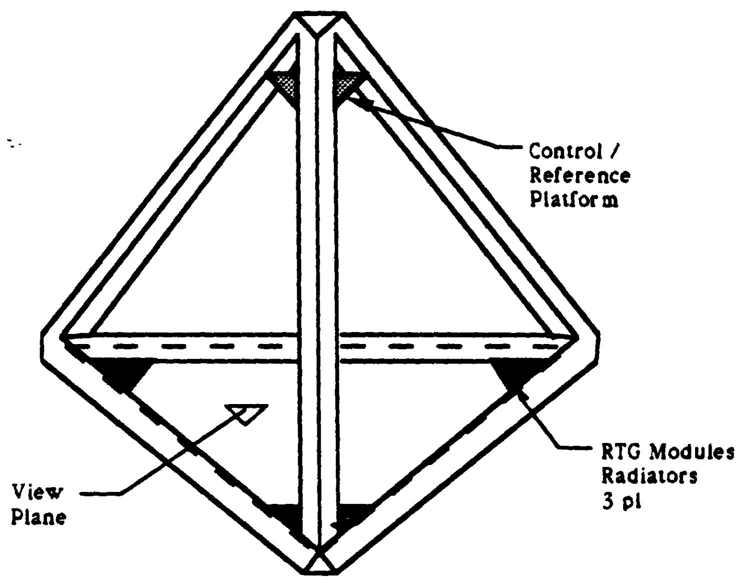

Figure 5.4: RTG Power Subsystem Layout on the OPTICS Vehicle.

Based on the need to radiate large amounts of heat, the baseline RTG locations are chosen at the intersections of the view plane legs to permit a guaranteed view to "dark" space, since the viewing requirements of science siderostats in this plane are always away from the sun. To avoid flexi-body interactions, and to facilitate more efficient heat transport, the radiators are "hard-mounted" to the inboard edges of the view plane truss legs, facing outward and forming a web at the truss leg interface. RTG modules are then mounted to the inboard side of the truss structure at leg intersection nodes where they conveniently interface with the radiators. Additionally, inboard locations are selected to permit ample room for siderostats to traverse the maximum baseline, and to limit thermal energy to these critical elements. The remote location at the view-plane apex is also beneficial to provide adequate distance from the harmful radiation products to sensitive electronics on the reference platform. Although, at this modest level of power, and with good encapsulation, radiation doses are a minor concern [4].

5.1.3 Power Subsystem Disturbances

With understanding of the required elements for the power subsystem and their relative sizings, disturbance sources are quantified for the power subsystem options. Refer to Chapter 2 for a detailed discussion of the various potential disturbance mechanisms.

Photovoltaic

Disturbances from the SA-battery system arise primarily as environmental effects from the addition of large area arrays, torque interactions between the vehicle and the large flexible appendages, and vibrations induced by the SA drive motors. In the extreme case with the view axis in the orbital plane, the arrays are in their maximum area configuration and account for ≈(30-50)% (max) of the incident spacecraft area. This results in the addition of the following atmospheric effects:

- $(F_{aero})_{SA} \approx$ 0.12 to 0.20 N (max)
- $(T_{aero})_{SA} \approx$ 0.21 to 0.35 N m (max)
- $(H_{aero})_{SA} \approx$ 180 to 300 N m s (max)

As previously discussed, these additional environmental disturbances are handled much as DC influences, and result in a 30-50% scaling of those system elements driven by their magnitude. For example, this would mean the addition of one Space Telescope RWA per axis. The baseline for OPTICS carries solar arrays which are used in the total environmental disturbance sizing.

The command torque to slew the SA's relative to the vehicle must be sufficient to overcome the array inertia, motor drag and bearing friction, and retarding torques from the electrical harness, all reacted by the spacecraft. For the array slew requirement of 90° in 60 min, the required constant torque to overcome the array inertia is on the order of a milli-N-m max. The dominant torque is due to cable stiffness and demands over an order of magnitude greater torque. Because of the similarity of OPTICS arrays to those used on Hubble, typical array command torque values from HST are used in the model [52], and to calculate drive motor disturbances, which depend on the command torque. The array flexi-body, or damping torques following an array or spacecraft slew depend greatly on the torque command shaping and oscillate at harmonics of the array fundamental, approximated at 1 hz (max). Following is a summary of SA drive and damping torque disturbances:

- $T_{Command} \approx$ 0.25 N m (max)
- $T_{Ripple} \approx$ (5%) $T_{Command}$ @ 0.01 Hz
- $T_{Cogging} \approx$ (2%) $T_{Command}$ @ 0.1 Hz
- $T_{Damp} \approx$ 0.004 to 0.04 N m @ $(f_1)_{SA}$=1 Hz

These disturbance torques act primarily about the drive axis, whereas the lower order disturbance torques and forces are neglected. The magnitude and behavior of the damping torque is highly dependant upon the specific dynamics of the array. Since the model does not include dynamics from these appendages, flexible interactions are approximated here as "external" torques oscillating at the estimated natural frequency with magnitudes commensurate with the HST data. Torques from solar array thermal warping, particularly the transient effects from eclipse, can also disturb the vehicle. These torques are generally low magnitude and exponential in behavior, and therefore pose no additional problem to the drive and damping disturbances listed above.

RTG

The RTG power subsystem disturbances are primarily additional environmental effects and flexible interactions from the large radiators (similar to SA's), the transport of coolant fluids, and the effects of thermal "pollution". Environmental disturbances, again are a function of the incident area, which for the RTG radiators are 60% of the worst case SA total area, and the disturbances listed above. Potential flexi-body interactions and tracking vibrations are eliminated by hard mounting the radiators to the truss structure, with the resulting radiator fundamental estimated at above 10 Hz. For each RTG module, consisting of multiple generators, it is assumed that a common thermal system is employed, thus the coolant disturbances are representative for each module. The transport of coolant fluids is modelled as a random, white disturbance, scaled from flow noise data given in [38] and discussed in Chapter 2, representing a range of lower coolant mass flow rates between 1-10 GPM[4]:

- Coolant Flow Rate: 1 to 10 GPM
- Force: $F_{RTG} \approx$ 0.0004 to 0.04 N RMS (12-500 Hz)
- Force PSD: $S_f \approx$ 1.6E-10 to 1.6E-6 N^2/Hz

The assumption here is that the flow noise is band-limited white for the frequencies modelled (0.1 - 100 Hz), ie. constant power spectral density. The frequency range indicated for the flow force is the bandwidth of the force transducer used to extract the data, and is used only to compute the constant PSD value, which is then smeared over

[4]GPM: gallons per minute = 6.31E-05 m^3/sec

the frequency range of interest, according to the following relation [25]:

$$\sigma^2_{\omega_1-\omega_2} = \left(\frac{1}{\pi}\right)\int_{\omega_1}^{\omega_2} S_f(\omega)d\omega \tag{5.1}$$

$$S_f = \frac{\pi\sigma^2}{(\omega_2 - \omega_1)} \tag{5.2}$$

Where S_f is the force power spectral density, and σ the RMS value. The actual flow noise behavior will tend to be more dominant at higher frequencies, however, depending on the flow rate, but is modelled here as worst-case white within the model bandwidth.

The large amounts of thermal energy that must be radiated away from the RTG system, or from any thermal-electric system for that matter, must be directed properly to avoid a substantial view factor to sensitive components. For the RTG system, the radiator view is largely unobstructed in the siderostat view direction, limiting the heat flux to the coupled structure, and at times to neighboring siderostats. Standard thermal design practice will limit the thermal energy absorbed by the siderostat modules and surrounding structure. However, with the RTG system operating primarily in steady state, the residual thermal deformations, producing pathlength errors as large as a few microns, have time constants within the bandwidth of the optical pathlength compensators (PCD's), at up to $\approx$10 Hz.

One additional point to note here is that, due to the large additional mass of the RTG system over photovoltaic, $\approx$ 400 kg total from three locations, the system fundamental frequency is reduced by nearly 5%. However, this is a small change compared to the SA fundamental, and not nearly as significant as the system cost incurred from the mass penalty of the RTG system.

5.1.4 System Response to Power Subsystem Disturbances

This section investigates the response and degradation of performance, the differential pathlength errors, of the OPTICS system model to the disturbances introduced by the power subsystem options. The magnitudes and behavior of the disturbance responses are quantified for evaluation in the following section. As previously indicated, the environmental disturbances associated with the large areas for both options are effectively distributed DC forces and torques. Their influence must be reacted by the attitude control system, and affect the orbital parameters, but will not directly excite flexible response of the vehicle. The effect of rigid body control is a factor in evaluating other subsystems, ACS for example where control of the rigid body can excite flexible motion. However the model does not include rigid body modes and these effects are not further evaluated.

Photovoltaic

Since the interferometer is inertially fixed for nominal science operations, SA tracking is required only during or following a spacecraft maneuver, indicating that the transient behavior is of importance. It is therefore of benefit to know the maximum response experienced during a tracking maneuver, and more importantly, how long it takes to contain the residual vibrations to the specified 10 nanometer pathlength error. System requirements for this subsystem dictate 10 seconds to settle within the 10 nm.

Torque commands are typically shaped to avoid flexible excitation, ramped up and down to their maximum values during the maneuver. Figure 5.5 shows this general form over one slew cycle, and the command and disturbance torques input to find the maximum pathlength response. The front end of the characteristic torque command (a sine ramp) is implemented, plus the additional disturbances previously outlined, as representative of the maneuver. These are implemented at each of the three SA locations about the respective drive axes, with the command torque reacted at the three ACS actuator locations. Figure 5.6 shows the pathlength error response during the first 100 sec of a 90° array slew, for the nominal "undamped" model (0.1% structural damping ratio). The majority of the response is the low frequency component associated with the command torque. Figure 5.7 shows how the linear model responds to a static torque command, indicating the relative pathlength errors associated with various SA command torque amplitudes.

The jitter response is generally of greater concern, as the higher frequency vibrations are inherently more difficult to compensate, and produce the peak responses which must be minimized. Figure 5.8 displays the first order potential for lowering this response through damping augmentation. The two curves represent peak responses in the time domain associated with increasing levels of damping for an expected range of driving torque levels for the OPTICS arrays [52]. As the figure indicates, the maximum response may be significantly attenuated, by $\approx 50\%$ for a few percent damping.

Errors during an array slew are not critical. The important measure is the time required for the pathlength response to damp to acceptable levels following a slew. As indicated, the torque commands are typically shaped to avoid flexible excitation, but to look qualitatively at the system time constant, a torque step is imparted to the vehicle, of magnitude equal to the maximum command torque. The pathlength response is then observed for varying levels of structural damping included in the model. Figure 5.9 shows the typical undamped response for a 0.25 Nm torque step, and Figure 5.10 displays the time required to settle pathlength errors to 10 nanometers for increased structural damping. Again, an upper and lower torque step magnitude (0.10 and 0.25 Nm) are shown. This figure indicates that with reasonable amounts of structural damping, less than 10%, the response can be held to desired levels within the allotted 10 seconds to not impinge on the scientific objectives.

Consistent with the numerical model, this damping time, or time constant is associated with the entire spacecraft plant from an instantaneous torque step. The more efficient approach is to prescribe damping augmentation at the source: the solar array structure and drive mechanism. To the first order, damping in the structure simply lowers the peak response as the arrays continue to vibrate. Whereas damping in the array reduces the maximum vibration amplitude and rapidly dissipates energy by placing the dissipation mechanism in the region of greatest strain energy, lowering the response time constant. However, the current model does not replicate array dynamics, and therefore the above calculations for vehicle settling time are assumed to be commensurate with that for the solar arrays.

RTG

The RTG's operate in an unregulated, steady-state mode to produce electrical power, thus the random flow vibrations will exist at all stages of the mission. It is critical to understand the maximum amplitudes of differential pathlength error and frequency content of the response in order to gage how these disturbances may be confronted. The frequency domain is therefore employed to estimate the maximum jitter response expected at each frequency, and the power spectral density from which RMS values may be extracted and compared with the 10 nanometer RMS specification.

To obtain the maximum jitter response, the composite of frequency responses, or transfer functions, from RTG disturbance input locations to the differential pathlength is multiplied by the expected maximum flow force at each frequency. This disturbance is taken to be the "3-sigma" value of the RMS force within the bandwidth of the model (0.1-100 Hz). To calculate this value, equation 5.1 is used with the model frequencies (0.6-37 Hz) and the previously calculated force PSD. The maximum forces are then: $(F_{RTG})_{max} = 0.00018 \; to \; 0.018$ N (0.1-100 Hz), and Figure 5.11 displays the resulting maximum pathlength jitter profiles for 1 and 10 GPM flow. It is seen that even for the low flow rate disturbances, errors surpass the 10 nanometer specification, particularly around the fundamental frequencies.

As discussed in Chapter 4, peak response is important for determining the instantaneous quality of data taken by the interferometer. However, over a sampling interval, the time spent at one of these peak values is assumed to be quite small for a random process, and therefore averages out over the observation interval. This is why root-mean-square (RMS) values are of greater importance to interferometric imaging and the mission performance metric, and is estimated for the RTG disturbances. Within the sample interval, the random flow process is assumed stationary, and permits calculation of the RMS value through integration of the pathlength response power spectral density (PSD). Figure 5.12 displays the pathlength error response autospectra to the corresponding input flow noise PSD for 1 and 10 GPM disturbance flow amplitudes previously defined. Because the input is "white", this output spectrum corresponds to the square of the composite frequency response from the three distributed RTG modules, scaled by the force amplitude, and therefore is similar in form to the jitter response. Note the typical rolled off behavior of the response, consistent with frequency response, and significant modal sensitivity across the bandwidth modelled. RMS values are 14 and 1440 nanometers respectively for the 1 and 10 GPM flows, a large range indicating some compensation is required for either case. With understanding of the open loop response to disturbances, the approach for obtaining system performance is discussed.

5.1.5 Approach to Minimizing Power Subsystem Disturbances

From the above discussion and consideration of the types and levels of performance response obtained, a general approach for minimizing power subsystem disturbances is discussed. The primary focus is on limiting and attenuating disturbances where possible, guiding the physical properties and layout to lessen their influence, and indicating elements from the CST "toolbox" well suited to confront the residual behavior.

Environmental disturbances from large area arrays, either solar or radiator, are generally unavoidable and are minimized through balanced geometry and array layout with respect to the center of gravity, where possible. As highly distributed, very low frequency disturbers, they do not excite flexible resonance in the structure, which impacts the internal differential pathlength. But, rather they demand of the rigid body, attitude control and the external pathlength stability. As is seen in the following section (ACS subsystem), control of the rigid body motion can excite the flexible modes of the structure from both the selected control bandwidth and operation of control actuators. The feature of this section, then is minimization of the onboard or internal error sources.

Photovoltaic

Since the solar arrays are locked for science operations, the major concern is on reducing the settling time of the transient response following a relative SA-spacecraft maneuver, and keeping the peak response in check during the slew. Figure 5.10 indicates that 10% damping is required to contain the pathlength response to 10 nanometers within 10 seconds for a discrete torque step. Though, this is quite conservative because the damping is applied to the entire vehicle, and the actual torque command is shaped, as previously discussed. However, applying this data qualitatively to the solar array structure and recalling the similarity in bending fundamental to the spacecraft model (<1 Hz), it is evident that a few percent damping (10% max) at the source of vibration at the arrays will be sufficient to meet the performance specification of 10 nanometers in 10 seconds, assuming a well shaped torque command. This is the traditional approach to flexible array response, and can be maintained for the levels of power, and thus solar array sizes, demanded by astronomical spacecraft as this.

The estimate for solar array bending fundamental (0.1-1 Hz) shows that it is a likely driver for the lowest system fundamental, taking also into account the attachment flexibility. This is important in that they will contribute to the modal density at the low end of the bandwidth and push it lower, where the greatest sensitivity to disturbances exist. However, for OPTICS, the pathlength compensation devices (PCD's), with a bandwidth between 1 and 10 Hz should adequately compensate errors from these low frequency dynamics, as is seen for RTG disturbances. This also holds for the low magnitude, exponential-type torques induced by thermal transients as the vehicle enters and exits eclipse once every 93 minutes. Where the time constant of the thermal response is well within the bandwidth of the PCD's.

RTG

RTG disturbances are at the same time very similar to and quite different from the solar arrays, producing similar environmental effects from large area components, but also include a steady-state vibration field . The RTG option includes radiators which are large area, flexible appendages like solar array panels. By hard mounting the radiator arrays, the flexible-body interactions associated with a cantilevered configuration are significantly reduced. This will, however modify the local dynamics, depending on the specific mounting structure and attach locations, but pose no additional dynamical constraints on the vehicle with a bending fundamental estimated at greater than 10 Hz.

The steady-state random disturbance field for the RTG units cover a wide bandwidth. And as the responses confirm, all modes receive energy, driving them in resonance at levels consistent with the inherent frequency response. Indicated by the response to maximum flow levels, integration of Figure 5.12 displays that over a factor of 100 reduction in the RMS value is required. And Figure 5.11 shows that attenuation is needed over all frequencies modelled. The largest contribution to error is below 1 Hz at the fundamental eigenfrequencies, suggesting that the low frequency pathlength control be used. Figure 5.13 shows the RMS pathlength response to maximum flow vibrations for PCD corner frequencies between 0.1 and 100 Hz, and for structural damping ratios of ζ=0.1, 1.0 and 10%. For delay line compensation alone, it is clear that a bandwidth of nearly 100 Hz is needed for the undamped plant to meet spec at 10 nanometers. This is beyond the capability of this instrument, however, where a maximum bandwidth of 10 Hz produces 98 n-m RMS, an order of magnitude too great.

Increasing the structural damping ratio "smooths" over the peak jitter amplitudes as seen in Figure 5.14, where 10% damping provides a factor of 20 reduction in the uncompensated peak jitter response. This behavior over a range of damping is seen in Figure 5.15, showing peak response in the modelled bandwidth versus structural damping ratio. Again, the two curves in the figure represent bounds for a range of potential flow amplitudes, between 1 and 10 GPM. Here it is evident that, even for levels of damping approaching 10%, the peak response is over two orders of magnitude above the budgeted performance level of 10 nanometers for the maximum flow rate. A similar smoothing of response occurs in the power spectrum. And for a range of damping, the potential for reducing RMS response is seen in Figure 5.16, for coolant flow rates of 1 and 10 GPM. Again, we observe the excessive response for maximum flow disturbances, even for damping levels above 10%. Coupling damping with the pathlength compensators, as in Figure 5.13, it is seen that with lots of damping, around 10% or more, and fast PCD's, approaching 10 Hz, performance may be realized. This may be a bit aggressive for pathlength control, however, and requires significant structural damping, so additional augmentation is investigated.

Because the power subsystem exerts no physical control authority on the spacecraft, as an ACS actuator for example, a soft mount isolation system may be prescribed, which is bounded, to the first order, only by the global dynamics. The mount should be soft enough, ie. a low corner frequency, to filter to the desired response level, but stiff enough to not drive the low frequency dynamics of the vehicle. This is illustrated by filtering the RTG disturbances with isolators typical of those used on HST, and investigating the subsequent response. Isolator dynamics are simplified here, but may represent, to the first order, the transfer function from either a passive or active mount. Figure 3.1 shows the general transmissibility function utilized, typical of the HST RWA isolator characteristics [10], with an isolator damping ratio chosen (ζ_I=5%) to maintain the rapid rolloff characteristic (-40dB/dec) and contain the resonant amplification. The more heavily damped isolator curve (ζ = 0.707) is shown merely to illustrate the trade between isolator resonant response and rolloff slope with greater isolator damping.

Implementing this isolator, with corner frequencies ranging between 0.1 and 100 Hz, at the RTG module structural interfaces, produces Figure 5.17. This plot shows RMS performance of the uncompensated pathlength versus isolator frequency for structural damping ratios of ζ=0.1, 1.0 and 10%. The 10 nanometer requirement line is also shown for reference, a factor of at least 10 below all of the curves. Here it is evident, as with PCD control and additional damping, that performance is not achieved solely with this "tool", or even with isolation and a reasonable amount of damping (<10%). From the figure, it is also clear that a problem area exists around the structural fundamental frequencies just below 1 Hz, where it is desirable to position the isolation frequency well above this region to prevent driving the system dynamics. Including PCD control with damping enhancement and isolation results in Figure 5.18, showing RMS pathlength response versus isolator corner frequency various combinations. The 10 nanometer performance line is shown, indicating several combinations are possible.

Detail design of this system will determine an optimum system choice. But, to the first order, an isolator frequency above 1 Hz is desired to prevent driving the low frequency system dynamics. Therefore, a characteristic system is chosen to include 4 Hz isolation with a 1% structural damping ratio and pathlength compensation of 10 Hz. Maximum jitter response with this complement is shown in Figure 5.20. Again, multiple combinations of PCD control, isolation and damping exist which may satisfy performance specifications of 10 n-m RMS, where one solution is given above. The main difficulty here is in attenuating the lower modes of the system, where PCD control is struggling to push upward in the frequency spectrum and isolation downward to cover the frequencies around 1 Hz. This difficulty is illustrated in Figure 5.19.

Summary

Table 5.6 summarizes parameters for the power subsystem design options, photovoltaic and RTG, for minimizing system disturbances. The solar array - battery system is chosen as the superior candidate, based on a lower total system mass and easily manageable disturbances. Greater specific mass is achieved mainly through a more efficient conversion process, defined as that power available at end of life (5 kW) divided by the necessary power output of the generator (solar array / RTG). Also, the RTG system requires the additional mass of passive isolators at each structural interface, and a faster optical compensation system. As demonstrated, solar array transients will be contained within the required 10 seconds with command shaping and array damping (10% max), beyond which no performance degradation is expected. Compensation for the low magnitude errors produced by thermal transients, and from internal excitation of the low frequency array modes is provided by the PCD control loop.

Performance is also achievable with the RTG power system, although at a larger cost for the maximum expected coolant flow disturbances. Clearly, if the thermal control system can operate passively enough to limit coolant flow rates to a minimum (1 GPM), less than a factor of 2 in RMS response is required, as seen in Figure 5.16. This could be achieved through a small amount of distributed damping augmentation (a few % max). However, this only places the CST system complexity at par with the S/A's; the system mass penalty remains. And current expectation is that the higher flow rates will be required, resulting in greater disturbances and compensation complexity. Thus, the solar array - battery system provides the best alternative for minimizing system disturbances through power subsystem design.

Table 5.3: Design Parameters For Power Subsystem Options

Power Subsystem Option:	*Performance*	*Physical / Dynamical Characteristics*	*Disturbances*	*CST / Subsystem Interactions*
I. Photovoltaics: (arrays / concentrators)	40-200 W/kg 25-100 kW max 150-200 W/m2 10-15 years max ηcell ~15-20%	Large, planar area, flexible appendages; Drive mech; Tracking dynamics	E - Env't Disturbances (large area arrays) L - Flexible-body interactions M,H,R - Drive mech vibrations L - Thermal transients / warping Electric noise / EMI (all)	Sun tracking; FOV obstruction; DC power source; High volt / plasma interactions (Power storage) Heritage design
II. Thermal - electric:				
1. Solar - Thermal:	25-100's kW max ~5-7 X efficiency over photo ~1/3 area of photo	Large concentrator arrays of parabolic mirrors (~2kg/m2); Collector-receiver-converter-radiator; Tracking dynamics	E,L,M,H,R - Collector/radiator (similar to S/A) E - Thermal pollution L,M,R - Coolant transport (conversion)	Precise Sun tracking; 0.1-0.7 degree Radiators track anti-sun; FOV obstruction; High heat dissipation AC/DC power source No heritage; (Power storage)
2. Nuclear-Thermal / Isotopic: (static: RTG / dynamic: DIPS)	4-10 W/kg (RTG) ~500 W max per RTG 1-10 kW max - DIPS 10+ years	Heat generator unit - discrete; Large area radiators; (8 kg/kW; .6 kW/m2) Conversion system	E,L,R - Flexible radiators E - Thermal pollution L,M,R - Coolant transport (conversion)	Radiator tracking; FOV obstruction High heat dissipator; AC/DC power source Heritage design (RTG)
3. Nuclear-Thermal / Reactor: (static / dynamic)	10-50 W/kg 100's kW Long life	Reactor unit - discrete; Large area radiators; Conversion system	L,M,H,R - Reactor noise E,L,R - Flexible radiators E - Thermal pollution L,M,R - Coolant transport (conversion)	Radiator tracking; FOV obstruction High heat dissipation; High radiation intensity AC/DC power; source Limited heritage
4. Conversion:				
A. Direct (static): (therm-elec/thermionic)	10-15% maxc efficiency 10 year life	Small discrete unit (thermocouple,...)	E - Thermal pollution	High heat dissipation; DC power source; Limited heritage;
B. Thermodynamic: (therm-mech-elec)	Carnot efficiency limit ~5 X efficiency over direct	Thermodynamic heat engine:: turbine, pump, compressor, condensor, working medium	L,M,H,R - Rotating / pumping equipment R - Working medium transport E - Thermal pollution	High heat dissipation; AC power source; No heritage
III. Storage:				
1. Batteries: (secondary)	10-25 Whr/kg(NiCd) 20-40 Whr/kg(NiH2) 65% chg/dis (NiCd) - 80% (NiH2) 25% DOD (LEO) 5-10 yr life (LEO)	Battery cell packs;	E - Moderate thermal dissipation; (generator)	DC power source; Heritage design; Moderate heat dissipation (generator)
2. Fuel Cells: (regenerative)	100-120 W/kg 50-100 kW max 50-60% chg/dis 30-40% DOD	Fuel/electrolysis cell packs; Reactant (fluid) storage; Fuel and cooling fliud circuits; Plumbing	L - Reactant storage - slosh L,M,H,R - Reactant/product pumping and transport	DC power; source; No regenerative heritage (generator)

Table 5.3 (Con't): Design Parameters For Power Subsystem Options

Power Subsystem Option:	*Performance*	*Physical / Dynamical Characteristics*	*Disturbances*	*CST / Subsystem Interactions*
III. Storage (con't):				
3. Thermal Storage:	High efficiency =>90% More mass eff than batteries for therm-elec conversion	Utilizes latent heat of melting/ freezing salts; integral with therm-elec system	E - Thermal pollution	High heat dissipation; DC power source No heritage (generator)
4. Flywheels:	~20% efficiency improvement over Batty's; ~1/2 system mass of batt'ys	Large spinning flywheel; rotational excursions	L,M,H,R - Rotating flywheel E,L - Momentum exchange	DC power source; Interaction with ACS; No heritage (generator)

Table 5.5: Preliminary Power Subsystem Design

	Photovoltaic		
Solar Array:	$(P_{S/A})_{TOT}$	13.3	$(kW - BOL)$
	Area $(A_{S/A})_{TOT}$	114	(m^2)
	$(A_{S/A})_{EA}$	38	(m^2)
	Mass $(M_{S/A})_{TOT}$	228	(kg)
	$(M_{S/A})_{EA}$	76	(kg)
	$(M_{gimbal})_{EA}$	20	(kg)
	$(M_{pwrelec})_{EA}$	35	(kg)
Batteries (N_iH_2) :	$(M_{batty})_{EA}$	42	(kg)
Radiators:	P_{th}	1.25	(kW_{th})
(battery)	A_{rad}	2	(m^2)
	M_{rad}	10	(kg)
TOTAL MASS:	$(M_{photoelectric})_{TOT}$	528	(kg)
	RTG - Thermal		
RTG Units:	$(P_{RTG})_{TOT}$	5	(kW)
	$(M_{RTG})_{TOT}$	500	(kg)
	$(M_{pwrelec})_{TOT}$	40	(kg)
Radiator:	P_{th}	45	(kW_{th})
	$(A_{rad})_{EA}$	25	(m^2)
	$(M_{rad})_{EA}$	120	(kg)
TOTAL MASS:	$(M_{RTG-Thermal})_{TOT}$	900	(kg)

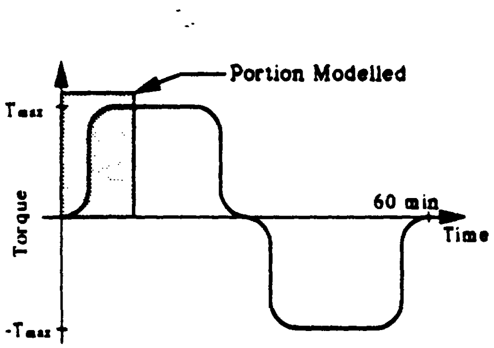

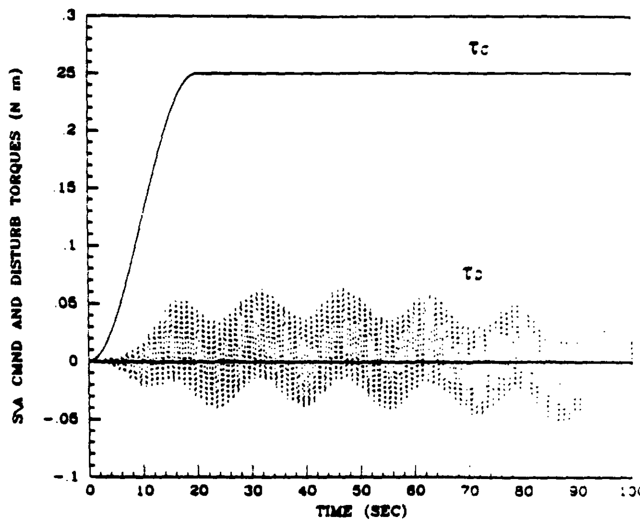

Figure 5.5: Typical SA Torque Command Over One Slew Cycle, and Modelled SA Command Torque and Disturbances.

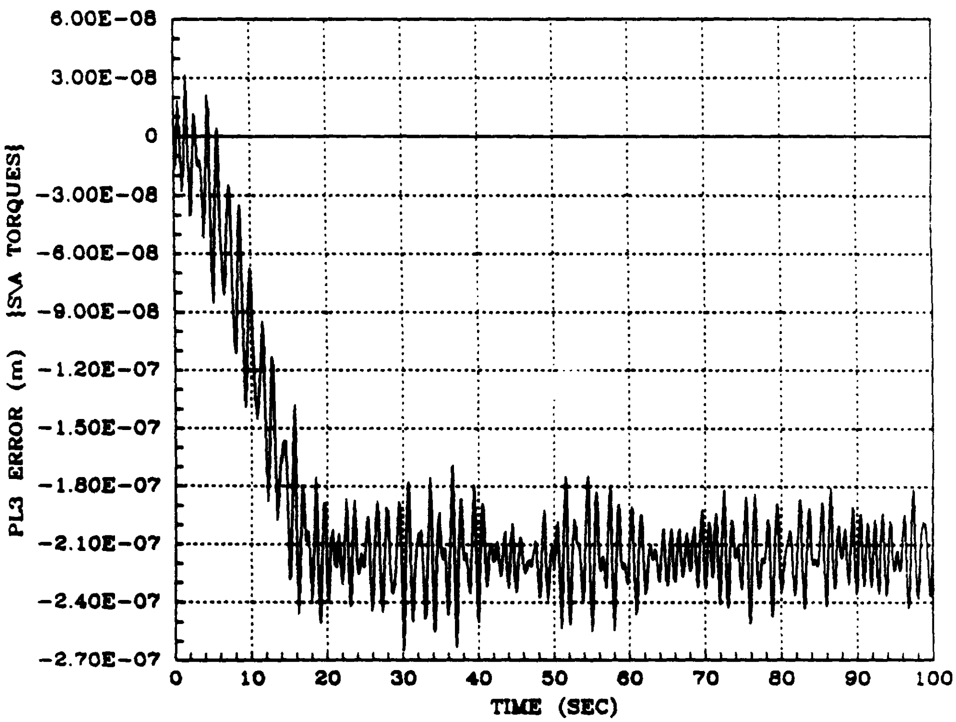

Figure 5.6: Pathlength Error Response to SA Drive Command and Disturbance Torques.

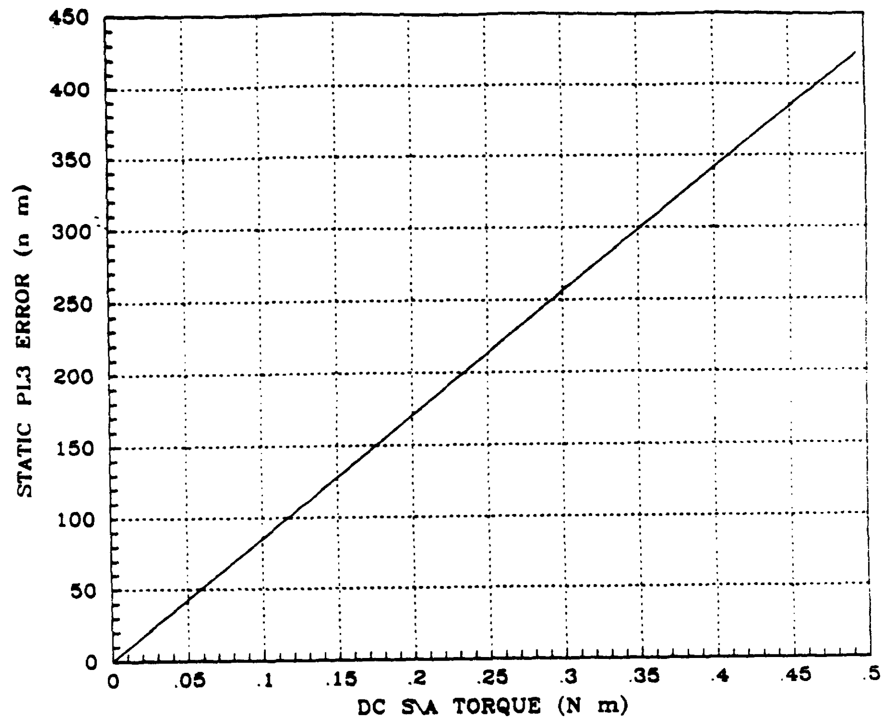

Figure 5.7: Static Pathlength Error to SA Command Torques.

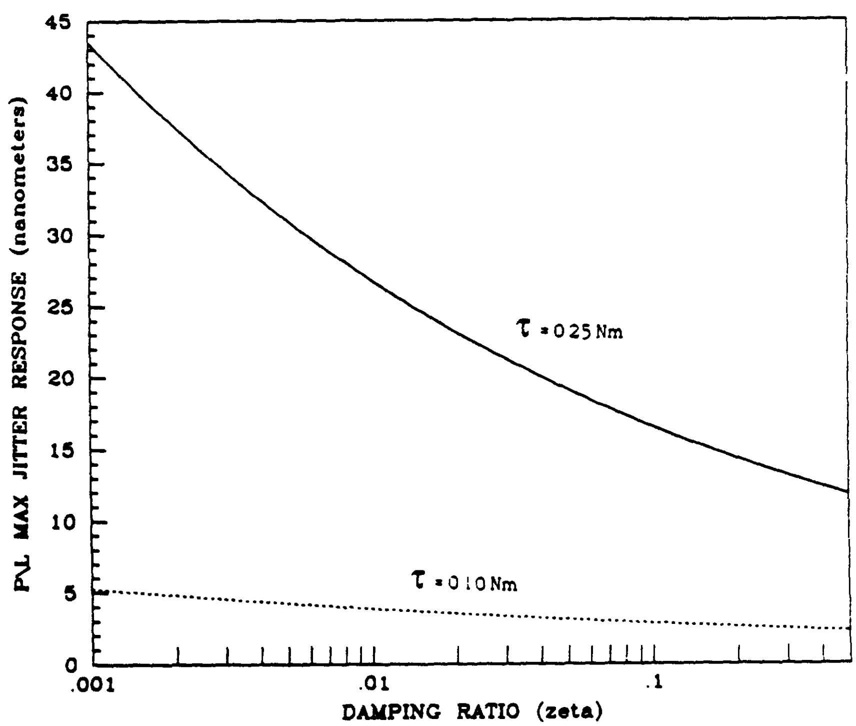

Figure 5.8: Pathlength Maximum Jitter Amplitude vs. Structural Damping Ratio for SA Command Torques of 0.10 & 0.25 Nm.

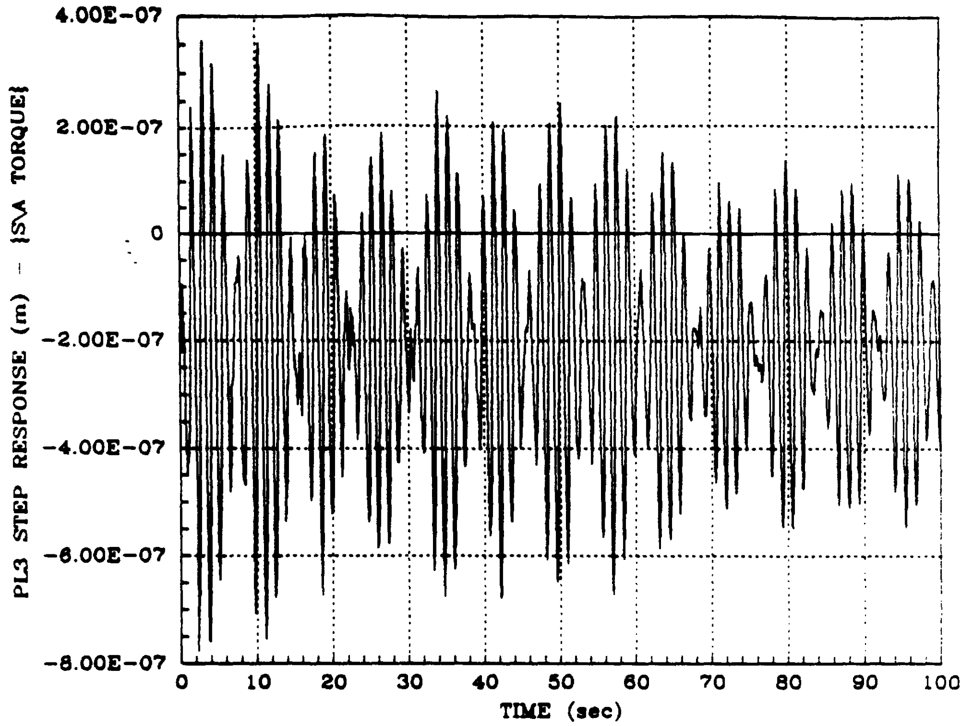

Figure 5.9: Pathlength Error Response to SA Torque Step Command: 0.25 Nm; ζ=0.1%.

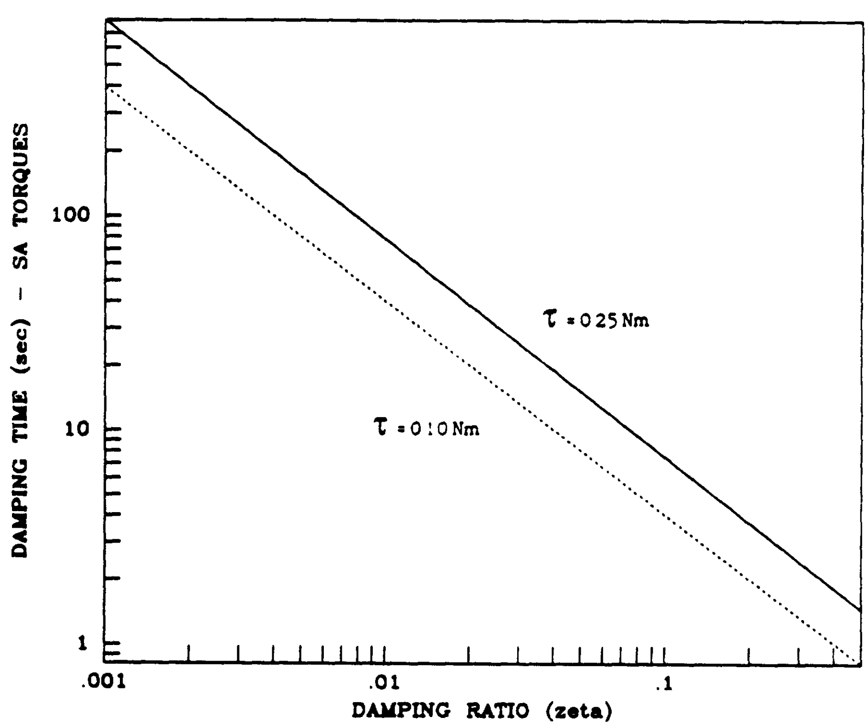

Figure 5.10: Pathlength Error Settling Time vs. Structural Damping Ratio: SA Slew Transients.

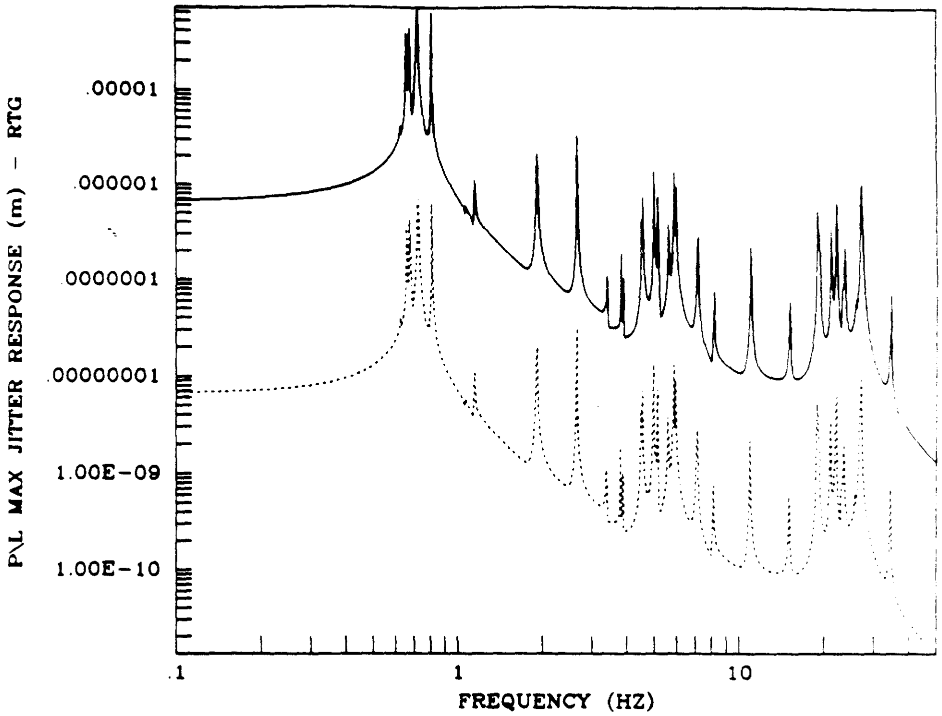

Figure 5.11: Pathlength Maximum Jitter Response to RTG Disturbances: 1 and 10

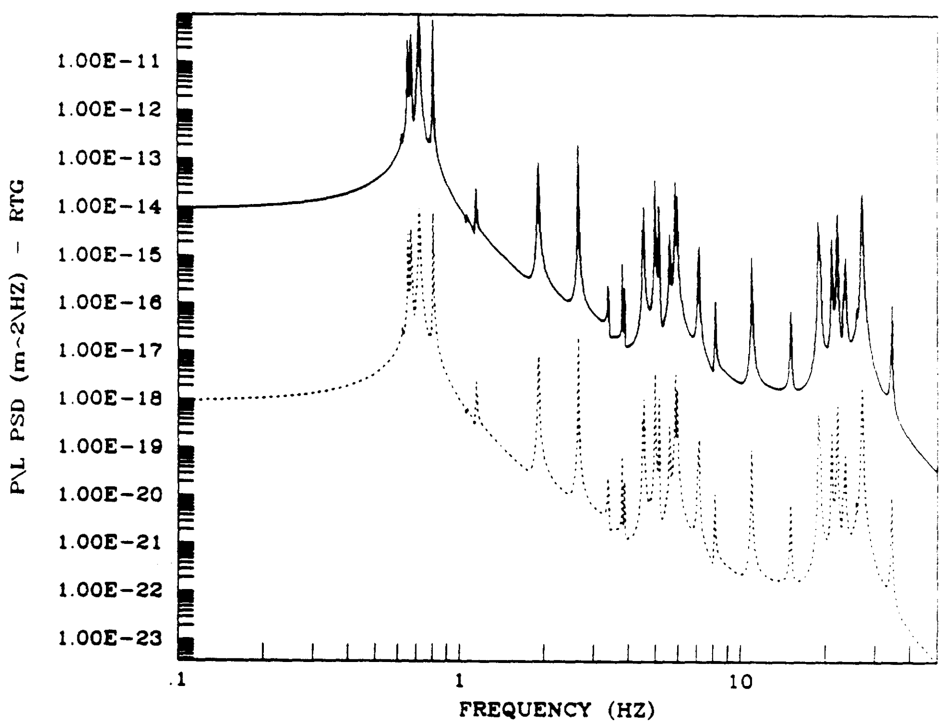

Figure 5.12: Pathlength Response Power Spectral Density to RTG Disturbances: 1 and 10 GPM Flow.

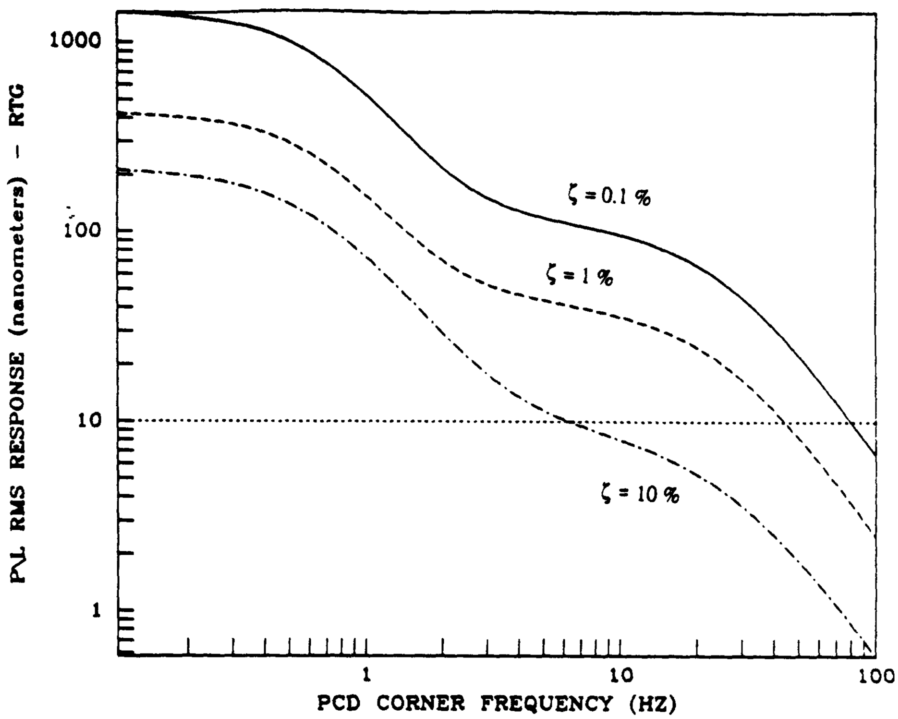

Figure 5.13: Pathlength RMS Response versus PCD Corner Frequency for Structural Damping Ratios of: ζ =0.1, 1 and 10%.

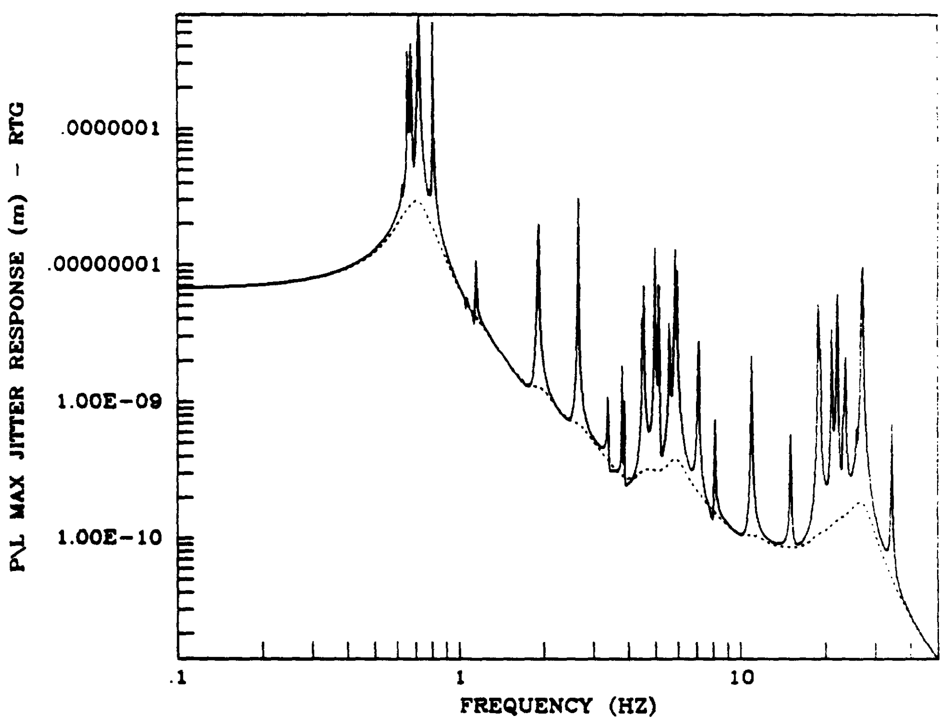

Figure 5.14: Potential for Maximum Jitter Response Reduction with 10% Structural Damping Ratio: 1 GPM Flow Noise.

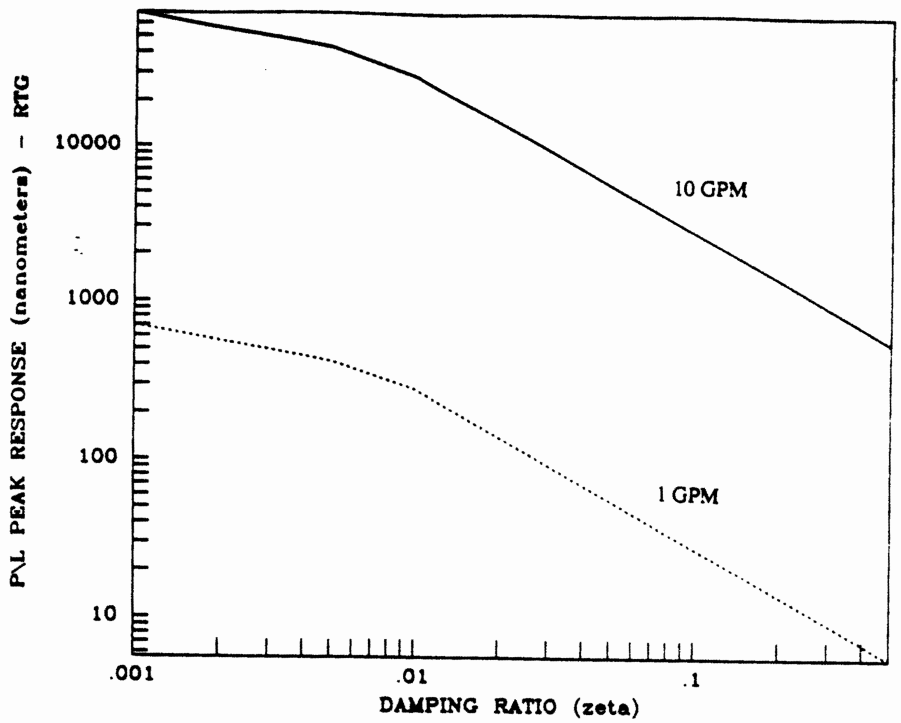

Figure 5.15: Pathlength Peak Jitter Response vs. Structural Damping Ratio: RTG Flow Noise at 1 and 10 GPM.

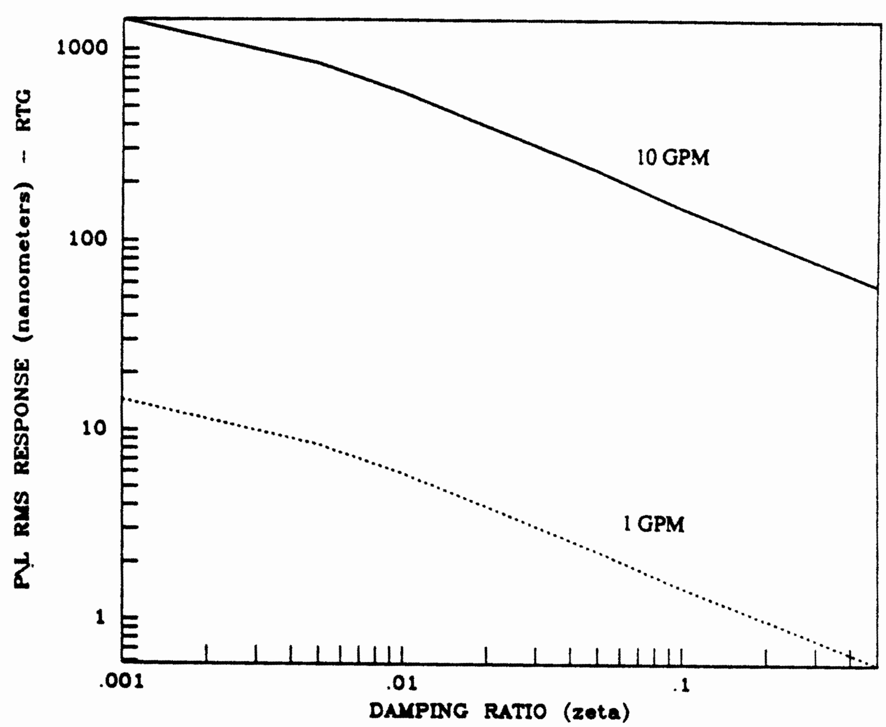

Figure 5.16: Pathlength RMS Response vs. Structural Damping Ratio: RTG Flow Noise at 1 and 10 GPM.

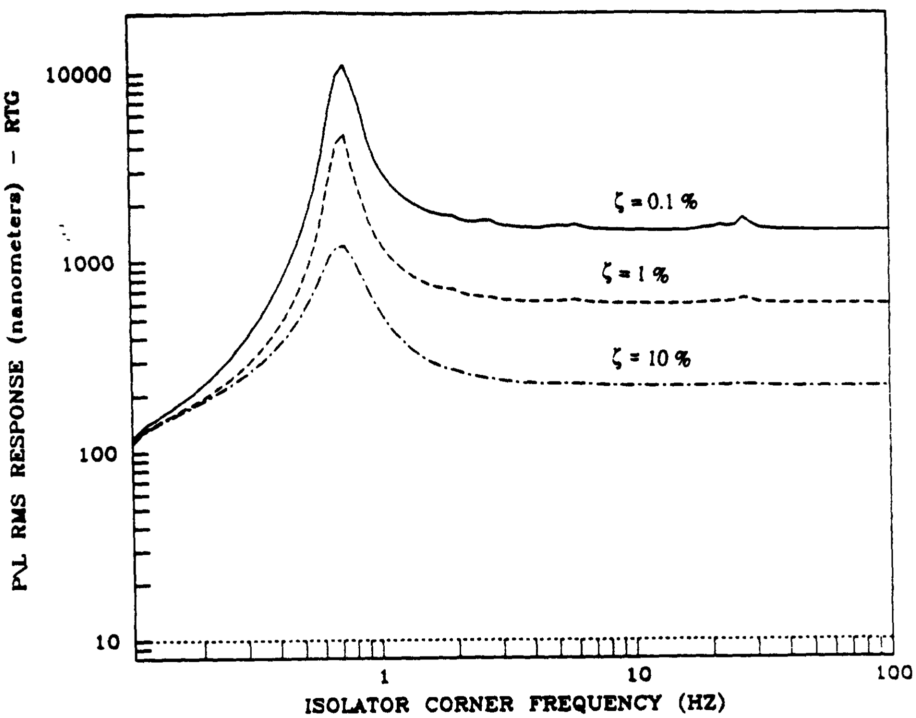

Figure 5.17: Pathlength RMS Response vs. Isolator Corner Frequency for Structural Damping Ratios of: ζ =0.1, 1 and 10%, and Maximum RTG Flow Noise.

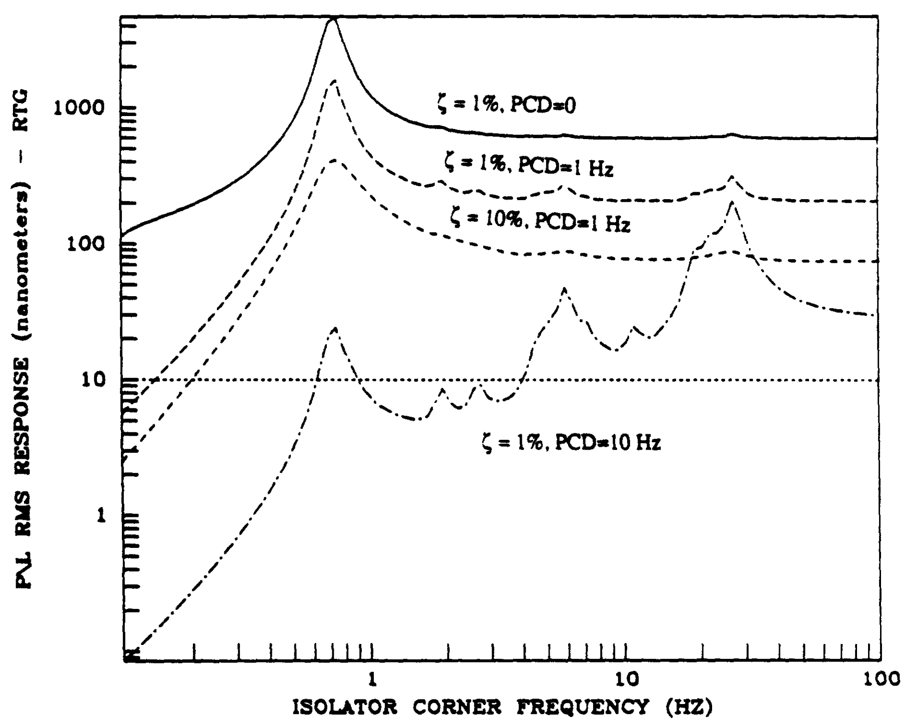

Figure 5.18: Pathlength RMS Response vs. Isolator Corner Frequency for Various Levels of PCD Control and Damping, and Maximum RTG Flow Noise.

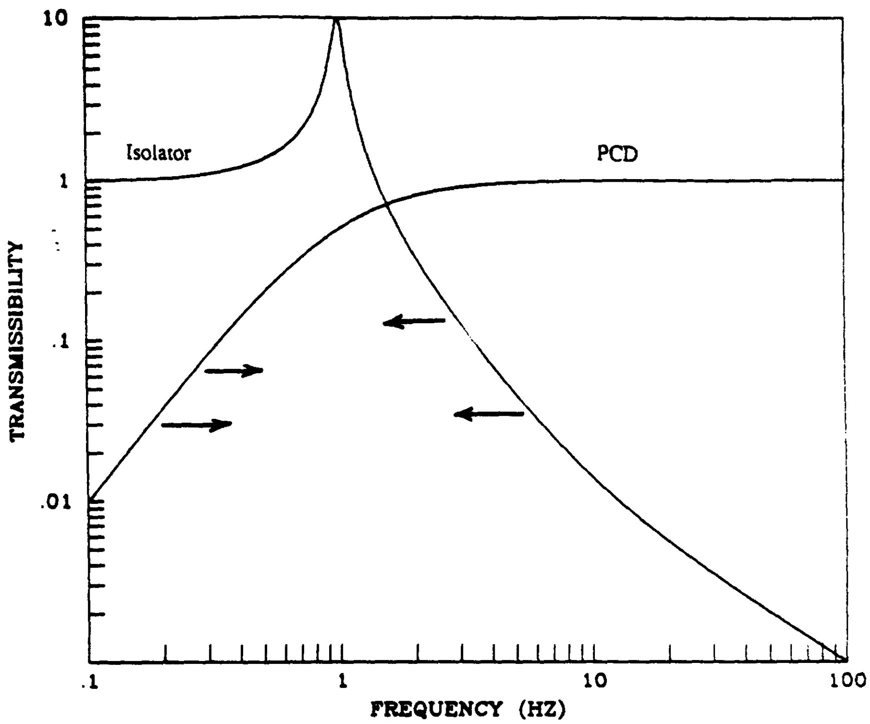

Figure 5.19: Typical PCD and Isolator Transfer Functions, Showing Overlap Region Near 1 Hz

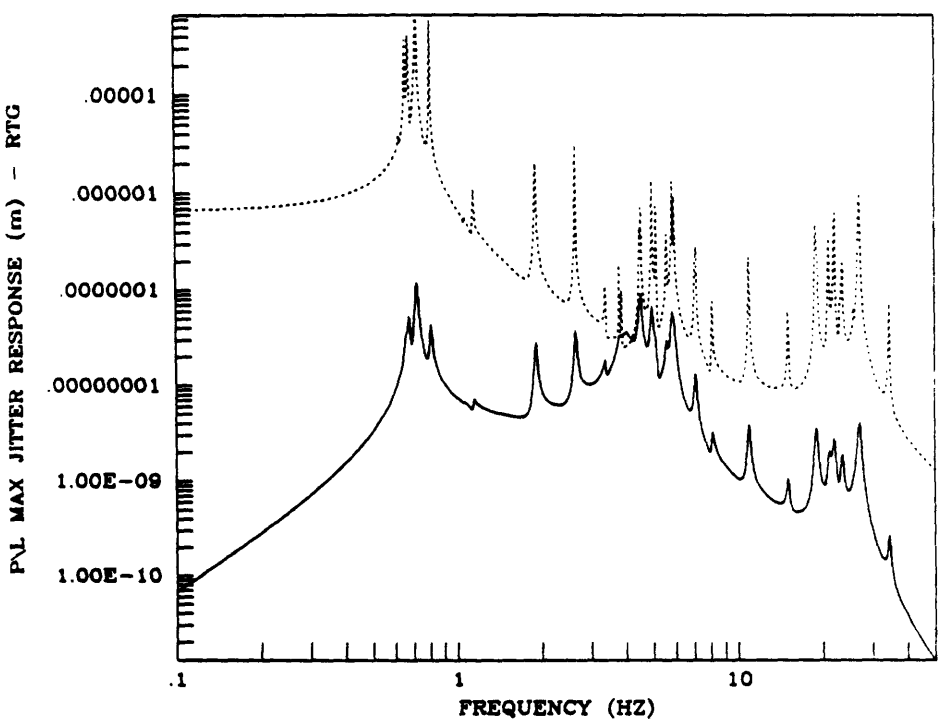

Figure 5.20: Pathlength Maximum Jitter for: 10 Hz PCD, 4 Hz Isolation and ζ=1%.

Table 5.6: Power Subsystem Design Summary

Parameter	*Photovoltaic System*	*RTG System*
1.Primary Elements (Qty):	Solar Arrays (3), Batteries (3)	RTG Generators (12), Radiators (3)
2.Total Subsystem Mass:	528 kg	900 kg
3.Total Array/Radiator Area:	116 m^2	70 m^2
4.Array/Radiator Bending Fundamental Frequency:	0.1 - 1.0 Hz	> 10 Hz
5.Total System Thermal Power:	8.3 kW_{th}	41 kW_{th}
6.Net Conversion Efficiency(η_{NET}):	0.38	0.11
7.Disturbance Types:	L,M,H - Transient Env't - Steady-State	R - Steady-State Env't - Steady State
8.On During Science:	NO	YES
9.Max Pathlength Jitter: Peak: (nanometers) RMS: Settling Time:	43 n-m NA 10 nm, 10 sec, 10% damp.	700-70,000 n-m 14-1440 n-m NA
10.Recommended CST Tools:	PCD Control: 1 Hz Array Damping Ratio: 10% max	PCD Control: 10 Hz Structural Damping Ratio: 1% Isolation: 4 Hz
11.Mass of CST System:	md	Md+Mi
12.CST Complexity:	Low	Low-Med

5.2 Attitude Control Subsystem (ACS)

This section investigates the design of an attitude control subsystem (ACS) toward the minimization of disturbances generated by ACS elements, in the similar format to the power subsystem. In a general sense, the ACS is responsible for acquiring and maintaining a prescribed orientation of the vehicle in space within allowable limits set by mission objectives. For an interferometric spacecraft, like OPTICS, the prescribed orientation is toward a targeted celestial object of interest in an inertial frame, within precision limits driven by optical quality and resolution demands. Attitude control is actually a subset of the broader subsystem including Guidance, Navigation and attitude Control (GNC). Guidance and navigation are not major challenges, given LEO as a stable orbit and tracking with the aid of TDRSS and GPS, particularly with respect to interactions with a CST vehicle. This assumes only that an adequate rigid-body spacecraft reference be provided. For OPTICS, the rigid body reference is provided at the control platform, which houses the primary attitude sensors and the metrology reference. Therefore, the primary focus here is on design of the attitude control elements.

Basic elements of the ACS are shown in the block diagram of Figure 5.21. Sensors are used to continuously monitor attitude and rate information that is compared with attitude specifications and provided to the controller which computes commands according to a control law. These commands are then issued to a torquing device or actuator to produce the appropriate control torques which act together with the sum of all disturbance torques to drive the vehicle to a new orientation. For a properly designed ACS, the new orientation will correspond to the specified attitude within the allowable tolerances. Thus, it is through the ACS that the spacecraft physically interacts with the external environment.

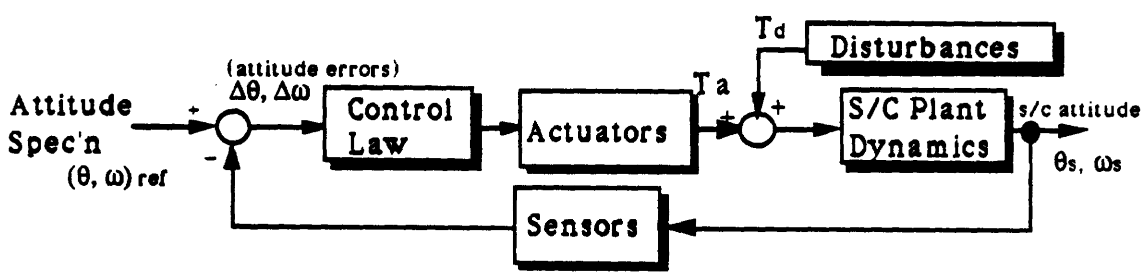

Figure 5.21: Attitude Control Subsystem Functional Block Diagram.

With respect to the challenge of flexible interactions, the ACS is the classic culprit, when energy from the attitude command bandwidth spills over to excite the flexible dynamics of large space structures [9]. The trend toward larger space vehicles with precision performance requirements, makes it increasingly difficult to prescribe the typical decade of minimum separation between the control bandwidth and structure fundamental [59]. Flexible modes of the structure push lower in the frequency spectrum, and performance mandates quicker response. Flexibility effects are exhibited either as superpositions of a high frequency signal or as the dominant component of attitude motion data, depending on the relative flexibility. Attitude errors can be present because of relative motion between attitude sensors and critical components, such as guidance siderostats, and may require additional sensors to determine the position of critical elements relative to the primary sensor. Figure 5.22 shows the first flexible mode of the vehicle and relative motions between the tetrahedron apexes, where is is clear that relative data is required to couple separated actuators, sensors and the reference platform at these locations. Laser metrology provides this link on OPTICS, and is discussed in the following section.

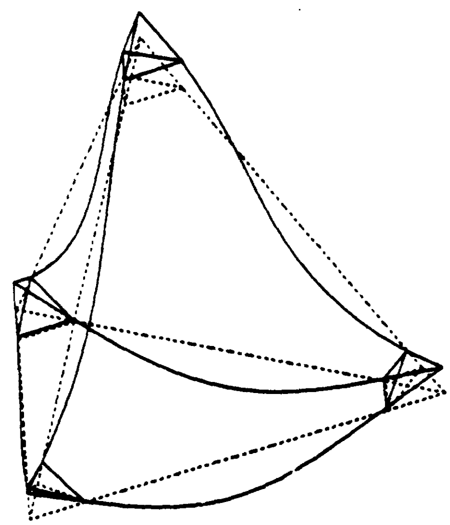

Figure 5.22: Vehicle Fundamental Bending Mode Showing the Relative Motion Between Tetrahedral Apexes Where Different ACS Components are Located. (Ref: Figure 5.24)

Selection of an ACS bandwidth is driven primarily by the need to provide sufficient control authority over the vehicle rigid body disturbances, while limiting the amount of control energy into the flexible modes of the structure. Environmental disturbances, vehicle slew maneuvers and internal flexible effects, including inertial torques from moving components and slewing appendages all affect the vehicle rigid body behavior, and should be included in the control bandwidth. Figure 5.23 depicts the rigid body disturbers in the frequency spectrum, as well as the appendage and structural modes. For this vehicle, with structural modes in the ballpark of the flexible appendage modes (0.1-1.0 Hz), an attitude control bandwidth below ≈0.01 Hz should allow flexible excitation from ACS commands to be neglected [59]. However, this will not provide adequate authority over the siderostat inertial reaction torques, discussed in the following section, which would like to be 0.1 Hz (1 m/10 sec) to prevent limiting science time. Figure 5.23 suggests a potential control bandwidth of 0.1 Hz, which includes appendage modes, but with sufficient rolloff to limit spillover into the structural frequencies. This is rather demanding of the control design, however, indicating that a more detailed system investigation is required.

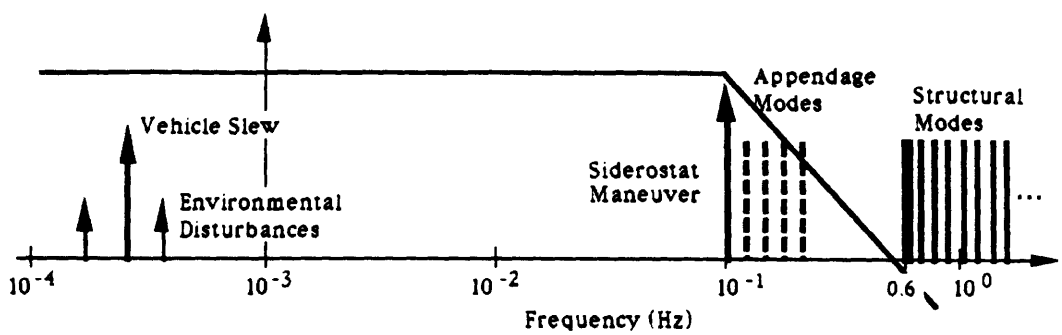

Figure 5.23: Attitude Control System Bandwidth Showing Rigid Body Disturbers and Interaction With Flexible Modes.

ACS requirements are imposed by the interferometer mission objectives, science instrument support demands and the vehicle architecture which drives ACS actuator requirements. These are outlined in Table 5.7. The tetrahedral interferometer is a free flying spacecraft in low earth orbit that is inertially oriented to view stars in the celestial sphere. Over a 6 month period, opportunity should exist to view the entire celestial sphere, given constraints from the sun, bright moon and limits of the earth's limb [37]. Pointing accuracy and stability requirements derive directly from particular science and instrument demands, thus a range is given to indicate orders of magnitude and show dependency on specific optical instrument design, which is not addressed in this thesis. As discussed in Chapter 4, the interferometer will view a target for periods up to 5 hours, and then maneuver toward another celestial object. To build up the total image requires approximately 1800-10 second "snapshots" taken for pairings of three siderostats corresponding to each unique location in the U-V plane. For each 10 second sample period, two siderostats are dedicated to collecting photons for the interferometer, while the third is simultaneously repositioned to a new location. Thus, throughout the 5 hour viewing interval, there are

Table 5.7: Attitude Control Subsystem Requirements

System Pointing Requirements:	
All Sky Coverage:	6 months
LOS Accuracy:	$0.01 - 0.10\ \widehat{sec}$
LOS Stability:	$0.001 - 0.010\ \widehat{sec}$
Attitude Hold:	5 sec *to* 1 *hr*
S/C Maneuvering:	90 deg / 60 min
ACS Actuator Requirements:	
Torque (τ_A):	20.0/0.4 N m
Momentum (H_A):	3500/2330 N m s (*cyclic/secular*)
Structural Requirements:	
PL Jitter Budget:	10 nano-meters RMS
Transient Vibrations:	Settle to 10 n m in < 10 sec

nominally two stationary, collecting siderostats and one mobile, providing nearly 100% available science time.

Although no general criteria exist for sizing of ACS actuators, they must provide control authority during all mission phases. This includes reacting net environmental disturbances, possessing sufficient capacity to handle vehicle and appendage maneuvers and with sufficient redundancy to avoid catastrophic single-point failure. Preliminary estimates of external disturbances are based on the information in Chapter 2 and physical parameters of the spacecraft. Magnitudes and general behavior of environmental torques and angular momentum are shown in Figures 5.25 and 5.26. Note the phasing shown in the plots is arbitrary, where the sum of maximum amplitudes are used for design. Clearly, the gravity gradient and aerodynamic effects dominate, with radiation pressure contributing due to the large area, and negligible magnetic torques.

Due to the large physical size of OPTICS, environmental disturbances play a significant role in sizing of ACS actuators, primarily from aerodynamic and gravity gradient sources. An inertial attitude precludes orienting the spacecraft primary axes within the orbital plane or toward the earth. Thus, atmospheric and gravity gradient disturbances are cyclic in nature, varying with attitude, and include considerable secular components (see Chapter 2). The large, distributed geometry of the tetrahedral spacecraft also results in great inertial properties, on the order of millions of kgm^2, where differences in principle inertias and cross terms, even for a reasonably well balanced vehicle, are high. Subsequently, the requirement for a balanced vehicle within $\approx 10^5$ kgm^2 is imposed to keep gravity gradient effects within the order of magnitude of the aerodynamic torques, which are also large due to the spatial properties of the tetrahedron and low earth altitude at 400 km. Chapter 4 shows that the general mass distribution of the vehicle meets this requirement.

Table 5.8 summarizes the ACS actuator torque and angular momentum requirements. The vehicle must be maneuvered quickly enough to permit maximum science time, but slowly enough to limit structural excitation and actuator authority. Figures 5.27 and 5.28 display the constant actuator torque and peak angular momentum vs. time required to slew the spacecraft 90°. Due to the large inertia, a vehicle maneuver demands great angular momentum, and it is desired to keep these within the order of the environmental momentum loads. This constraint is the primary impetus for selecting the maneuver requirement of 90°/60 min. Primary torque demands derive from the need to quickly translate siderostats to avoid science time constraints. To cover the U-V plane continuously with discrete science snapshots nominally requires siderostats to travel 1 meter in 10 seconds (0.2 m/sec max for a ramped velocity profile), resulting in 72 Nm constant torque reacted against the vehicle. As is shown in the following subsections, RWA's are torque limited, and designed for 0.1 m/sec max siderostat motion, or 20 Nm total torque. Natural precession of the orbit and attitude variation permits a situation with all environmental disturbances at their maximum amplitudes, the sum effect is thus used. However, a statistical (RSS) approach is utilized to compute the net effect from all contributors. Assuming 50% contingency, the total actuator torque/momentum requirement per vehicle axis is given.

5.2.1 ACS Design Options

This section reviews the major design options for elements of the attitude control subsystem, and selects candidates for preliminary design and investigation of disturbances in the subsections to follow. Referring again to the block diagram of Figure 5.21, elements within the realm of ACS design for addressing disturbance minimization are the control processor, sensors and actuators. This thesis in general does not attempt to design specific control strategies. Selection and design of an appropriate attitude control law, however, is integral to the system design of a CST vehicle, being inherently linked, and much work is currently devoted to attitude control of large flexible spacecraft [9,20,59]. The ACS control law is simplistically considered as a combination of proportional, integral and derivative control of three independent, SISO[5], axes: roll, pitch and yaw, at a bandwidth no greater than 0.1 Hz. Thus, as with the power subsystem, the parameters of principle interest to the selection of ACS components for OPTICS with respect to disturbance minimization are: the disturbances inherent in each ACS option, how these disturbances are manifest through physical integration with the vehicle, individual dynamical properties, and of course, sufficient performance capacity to meet subsystem specifications.

The component options for attitude sensors are primarily driven by the required attitude performance, on-board instrument demands and the operational characteristics of the vehicle. For OPTICS, the following complement of primary sensors is required:

- Sun Sensors
- Magnetometers
- Fixed Head Star Trackers (FHST)
- Rate Gyro Assemblies (RGA)
- Fine Guidance Interferometer (FGI)

Sun sensors are widely used to take advantage of this bright, stable and non-discriminating reference. It is also very important on spacecraft like OPTICS to know where to point solar arrays and to avoid sun-line orientations into sensitive optics. Magnetometers are necessary to provide information to a magnetic momentum management system, and to acquire coarse attitude information relative to the earth's magnetic field vector. Fixed head star trackers provide the first stage of precision star acquisition with its wide field of view ($\approx$8 X 8 deg^2). Stars are then captured by the fine guidance interferometer, not only by being within its field of view, but through active tracking of the central fringe of the interference pattern to provide the precision attitude information. The FGI also provides attitude updates to the rate gyro assemblies, which are used for angular rate data, and short term attitude information during slew maneuvers.

The only potential disturbers in this array are the RGA's [43]. With their rapidly spinning flywheels, rate gyros can display a disturbance spectrum similar to that of control moment gyros,which are investigated, but at much lower amplitudes. Therefore, sensor disturbances are purposefully overlooked, with attention toward the dominant ACS actuator disturbances. The effect that attitude sensors have on the net attitude dynamics is worth noting, however. Providing the feedback element of the attitude control transfer function,

[5] Single Input Single Output

sensors display their own dynamics basically of bandpass filters, which must be further filtered, smoothed and/or calibrated prior to use by the ACS control law. It is assumed that the sensor complement sufficiently acquires data within the control bandwidth, and no further consideration is given sensors.

Table 5.9 lists basic design parameters for the ACS actuator options grouped by stabilization approach, in the similar format to power options, showing performance parameters, physical characteristics and disturbance types. Clearly, with a variable inertial attitude, any form of gravity gradient or pressure stabilization may be excluded. Additionally, operational characteristics of OPTICS inherently precludes spin stabilizing the entire vehicle. Dual spin is also eliminated, because this drives the vehicle architecture away from isoinertialization. Beyond these considerations, active stabilization is the only alternative to achieve the stringent performance requirements.

It is the actuators for active attitude stabilization which present the more difficult choice of providing required control authority while limiting flexible interactions with the spacecraft from unwanted disturbances. ACS actuators generally fall into either of two categories: momentum exchange or torquing devices. Momentum exchange devices rely on the principle of conservation of angular momentum and must be able to provide the maximum torque needed for maneuvering and maintaining a prescribed spacecraft attitude, as well as storing the maximum cyclic angular momentum from environmental torques and appendage slews. These devices are momentum and reaction wheel assemblies (MWA, RWA[6]), and control moment gyros (CMG's). The RWA's and MWA's provide control torque from the rotational acceleration of a flywheel. The spin axis may be fixed in vehicle coordinates or gimballed to provide a variable torque axis, and is operated at a nominal zero (RWA) or non-zero (MWA) bias velocity. CMG's are gimballed flywheels which spin at a relatively constant, high angular rate that deliver torque by gimballing its angular momentum vector (the gyro effect). Single and double gimballed versions are available. Torquing devices react externally to the spacecraft system, and provide the means for counteracting secular momentum buildup. These include electromagnetic torque rods which react against the earth's magnetic field, and mass expulsion devices, or control jets which produce torque through thrust couples from engines which accelerate propellant molecules.

The choices thus come down to a form of spinning flywheel (RWA, CMG) with magnetic torque rods or propulsion for momentum management, or an all propulsive system

[6]The assembly includes drive motors and control electronics in addition to the flywheel

providing control torques. A propulsion system is a less complicated means for dumping momentum over magnetics, ie. a simpler control law, and provides the capability for autonomous orbital maintenance. However, propulsion adds the problem of effects from its contaminating effluent on sensitive optical components, and would have greater difficulty in meeting performance. In addition, a propulsion system is generally a highly complex system with distributed components, fuel tanks and plumbing network. Chemical propulsion requires storage of large amounts of fuel, and electrical propulsion typically demands substantial electrical power, on the order of 5 kW for 1 N thrust, for example. Thus, for OPTICS, control flywheels, RWA's and CMG's, with magnetic momentum control will be investigated; propulsion is excluded from further consideration.

5.2.2 ACS Preliminary Design

Table 5.10 shows system data for the complement of sensors needed by the interferometer spacecraft and two options for meeting the actuator requirements: Improved Hubble Space Telescope RWA's (I-RWA's) and advanced CMG's, both with state-of-art magnetic torquers for momentum management. The intent here, as we lead into the evaluation of disturbances, is to bound the problem by looking at a system based on current reaction wheel technology, and one on projected CMG capabilities, to address both types of disturbance spectra. CMG's are ultimately selected as baseline ACS actuators as the superior system option.

The I-HST RWA's are based on expected improvements of the current state-of-art RWA's, with approximately 2 Nm torque and 500 Nms angular momentum capacity each. Advanced CMG's derive from the Sperry M1700 series, and are projected at 4150 Nm / 2300 Nms. For 20 Nm torque and 3500 Nms cyclic momentum required of ACS actuators, 10 I-RWA's, driven by torque demands, or 1 CMG, driven by angular momentum, are required per axis. Clearly, the I-RWA's are harder pressed to meet spec, with over double the mass of CMG's to deliver 20 Nm torque per axis. It is this torque limitation for RWA's which constrain siderostat translations to below 0.1 m/sec, where these rapid translations along view-plane legs are reacted as torque by the ACS actuators. Greater velocities (eg. 0.2 m/s) are obtainable with CMG's, the baseline ACS actuator.

RWA's are known for providing precisely quantized torques for vehicle attitude stability. And with projected advancements in gimbal smoothness and accuracy, the CMG system should approach the pointing stability of reaction wheels [28,37], with reduced power levels and greater maneuver rates (higher torque). In either system, the flywheels are arranged in modules, corresponding to the number required per axis, and the number of discrete spacecraft locations: 1 CMG or 10 RWA's in each of three modules. Within each module, individual momentum vectors are arranged in a redundant configuration to allow control authority in each of the three independently controlled axes.

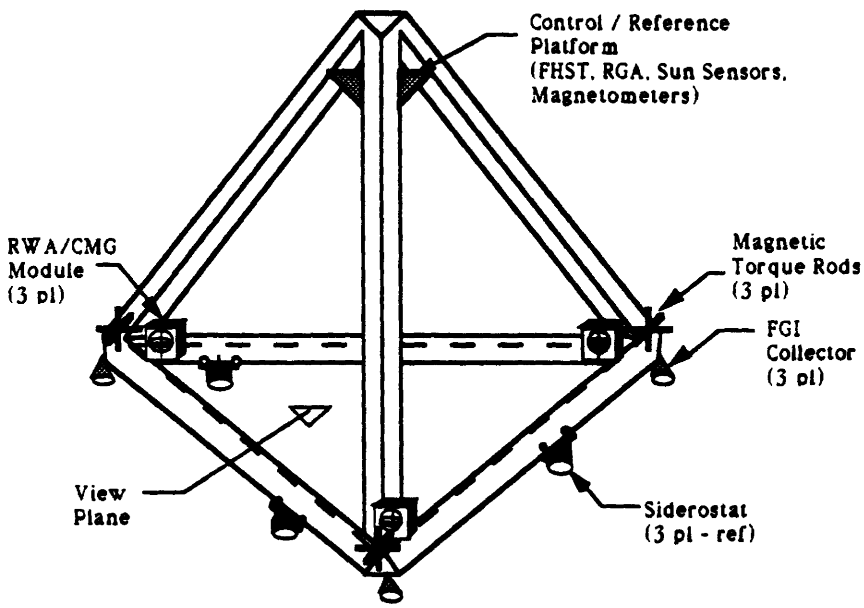

Figure 5.24: Vehicle Layout of the Major Attitude Control Subsystem Elements.

Referring to the spacecraft schematic of Figure 5.24, the baseline layout shows the CMG/RWA modules located symmetrically near the apexes of the view plane, the "sub-apex" locations, to help balance the mass of the control platform components at the fourth apex. Magnetic torquers are arranged symmetrically at the same apexes in a redundant orthogonal triad configuration to span the three-dimensional control space. Attitude sensors are primarily located on or near the control platform at the top apex for a wide available field of view (FOV) and close coupling with the spacecraft rigid body reference. Two sun sensors are mounted back-to-back externally at the extreme of the top apex for complete solar coverage, and the gyros and FHST's, requiring a highly stable vehicle reference, are anchored to the reference platform. FHST's obtain a convenient view through the view plane to the guidance star. The guidance interferometer collectors are positioned at the extremities of view plane apexes for maximum resolution separation, $\approx$ 35 m; guide star light from the collectors is directed up along the upright legs, through pathlength equalizers (PCD) and combined at the platform. Pathlength equalization is achieved similarly to science paths, with internal metrology measuring structural deformations from the collectors to combining optics, which are fed to the PCD's for compensation. External metrology fixes the platform reference with respect to the guide star, via the FGI collectors. This stable platform reference is thus used by the laser metrology truss for accurately fixing relative locations and orientations (displacements and rotations) of siderostats and FGI collectors throughout science operations. The interferometer and metrology systems are the topics of the following section. Metrology also provides a convenient reference for ACS actuators at the view plane apexes. The RWA/CMG modules, through a relatively stiff platform structure at the apexes, can rely on metrology data to correlate the vehicle rigid body attitude reference at the sensor platform with the attitude of their control axes: thus adequately coupling actuators with attitude sensor data. This collocated configuration should guarantee a stable closed-loop ACS system [59,9].

5.2.3 ACS Disturbances

Primary disturbances for the ACS, as outlined in Chapter 2, are from mechanical and electrical imperfections of rotating control flywheels, unshaped command thrust from control jets and vibrations from scanning or gimballed sensors. The complement of sensors required for OPTICS does not contain scanning or continuously gimballed sensors, and control jets are not included as a primary control actuator. Thus, flywheel disturbances from RWA's and CMG's are considered. In the current investigation, the wealth of data from the Hubble Space Telescope program on reaction wheel noise is adopted as characteristic for these devices. This "nominal" HST RWA model is then utilized for scaling and extrapolating to larger reaction wheels and CMG's.

RWA

Figures 5.29 and 5.30 show the nominal RWA model from relations given in Chapter 2, for maximum axial force of four dominant harmonics of the Space Telescope RWA as it is swept from 0 to 1200 RPM. Both maximum force and force power spectral density vs. frequency are shown. The lower curve is the nominal HST model, and the upper curve represents the I-RWA disturbance model. For a net imaging interval on the order of 5 hours, continuous, non-eclipsed sampling is seen over 2/3 of the orbit, on average, in discrete 10 second snapshots. From Figures 5.25 and 5.26, it is clear that the cyclic environmental effects, torque and angular momentum, reach a maximum within 1/2 an orbit. And in the following section (Interferometer and Metrology Subsystem), it is seen that reaction wheels are driven to their maximum torque values within a 10-20 second siderostat motion. Thus, considering built-in redundancy and contingency allowance, nominal RWA's are expected to traverse wheel speeds from 0 to 1200 RPM, and 0 to 3000 RPM for I-RWA's, within each science interval, resulting in the composite spectrum. Considering this net spectrum as stationary over the science interval, ie. the force PSD, may seem a bit-presumptuous. However, this provides a convenient means for estimating a worst-case RMS response from RWA vibrations, and is within $\approx$ 10% of a more correct RMS average utilizing a swept time response [44]. In a similar manner, the nominal HST RWA maximum torque model is estimated as shown in Figure 5.31.

For upgraded or larger wheels, the general relation for RWA disturbance force amplitude: $f_w \propto M_w \omega_w^2$, is employed, and similarly for torque. To obtain greater momentum and torque capacity from a RWA/CMG, to the first order, requires a larger flywheel (ie. one with greater inertia) and/or higher rotational velocities. The angular momentum of a spinning flywheel is given by: $H = I\omega$. So, the improved HST RWA design, with approximately 2X the momentum, requires some combination of increased inertia and wheel speed. For this disturbance model, 2 times the nominal mass and wheel speeds up to 3000 RPM are conservatively assumed. The resulting disturbance spectrum is seen with respect to the nominal model in Figures 5.29 and 5.30.

CMG

Because the CMG operates at a more constant angular rate, the frequency content of its disturbance will primarily be narrowband, with a broadband random gimbal friction disturbance at low amplitude [39]. For the advanced Sperry M1700 derivative CMG, nominal wheel speeds will be on the order of 6000 RPM or greater, indicating that the array of disturbance spikes will occur at 100 Hz and multiples thereof, with potential for lower harmonics. Except for the low amplitude friction component, this spectrum is beyond the useful bandwidth of the OPTICS numerical model, and therefore will limit evaluation of CMG disturbances to extrapolations from the RWA data. By utilizing the same relations, however, we may formulate a model for this disturbance spectrum, as shown schematically in Figure 5.32. This model assumes the Sperry M-1700 derivative, with approximately 3 times the mass of the nominal HST RWA, operating at a biased wheel speed of 6000 RPM (100 Hz), varying by plus or minus 200 RPM (3.3 Hz).

5.2.4 System Response to ACS Disturbances

Open loop responses of pathlength errors are investigated for the defined ACS disturbance sources: Nominal HST RWA model and Improved RWA model. As indicated, responses to the Advanced CMG model are not obtained, and discussed as projections from RWA responses. For all simulations, the nominal balanced, 50 mode reduced model is used with a reduced set of degrees of freedom based on necessary input and output parameters. Again, the model does not include local dynamics associated with mounts, support structure, and appendages, therefore the simulation represents first order effects of the disturbance models onto the global vehicle dynamics.

RWA

Utilizing the nominal HST reaction wheel model, open loop responses of this and the scaled version are implemented at model nodes corresponding to the RWA/CMG module locations at the sub-apexes of the view plane. As discussed, the normal operation of reaction flywheels produces the characteristic disturbance spectrum of force/torque spikes sweeping the frequency spectrum, approximated here as a stationary process. Therefore, the frequency domain is used for response simulations, where maximum and RMS pathlength errors are evaluated. The effect of transient response, and thus the time domain, is neglected.

In the first case, the nominal HST RWA force model, 0-1200 rpm, is implemented at the three sub-apex locations along each coordinate direction, corresponding to maximum axial and radial disturbances for a *single* wheel in each location. Pathlength responses to the I-RWA input spectra of Figures 5.29 and 5.30 are given in Figures 5.33 and 5.34 respectively, showing maximum jitter and power spectral density. Maximum jitter response, or jitter envelope, is the composite frequency response from the disturbance inputs to the pathlength error multiplied by the maximum disturbance force at each frequency, thus the close correlation with PSD. The heightened amplitudes with increasing frequency are due to the wheel speed squared dependency of the rotor imbalance force, resulting in significant pathlength response into the higher frequencies. Across the jitter spectrum, we see peaks on the order of 100 nanometers, with the maximum peak just over 1 micron. And integrating over the power spectrum produces 85 nanometers RMS, nearly an order of magnitude beyond the performance specification of 10 n-m RMS for this subsystem. In a similar manner, the nominal HST RWA maximum torque model of Figure 5.31 is implemented in the same locations, with the resulting jitter response shown in Figure 5.35. Note the similar response profile, and order of magnitude lower response amplitudes, indicating that force disturbances are the primary concern.

Next, disturbance spectra for RWA's characteristic of those required for OPTICS, I-RWA's, are implemented in the same model locations. The resulting jitter response is seen in Figure 5.36, displaying amplitudes at twice that of the nominal model at low frequencies, and nearly an order of magnitude greater at the high frequency maximum of $\approx$ 8 microns. Similarly, the pathlength error power spectrum of Figure 5.37 shows the increased response, with an RMS of 254 nanometers.

Responses presented represent the maximum disturbance model for a single reaction wheel at each of the three spacecraft locations. However, for a module of 10 RWA's, the net RMS response is estimated by taking the statistical average, a root-sum-square (RSS), of disturbances from each wheel in the module. For similar devices, this is equivalent to multiplying the RWA disturbance model for a single unit by the square root of the number of units, $\sqrt{10}$ in this case. For the nominal HST RWA model this produces 270 nanometers RMS pathlength response, and for the improved RWA model, 803 nanometers RMS, a factor of 80 over the required performance for this subsystem.

CMG

From the projected disturbance profile for control moment gyros, and knowledge of the pathlength behavior similar to the RWA inputs, responses to CMG disturbances may be extrapolated. Because disturbance magnitude increases proportionally with wheel speed squared out to around 100 Hz, and the frequency response of the structural plant generally rolls off as the square of frequency, response amplitudes are expected to increase only slightly at higher frequencies. By squinting, this is seen in the jitter plot of Figure 5.36, where some inconsistency at the high end is due to contributions from different disturbance harmonics and greater modal sensitivity. With this basic relation, and reference to Figures 5.32 and 5.36, maximum response amplitudes on the order of 10 microns are expected at harmonics of the CMG wheel speed, starting around 100 Hz for the dominant harmonics and dropping off quickly for higher and lower harmonics. Due to the highly bandlimited nature of this disturber, the RMS response is strongly dependant on the modal density around these frequency bands, not included in the present model. Should a dominant structural resonance exist at 100 Hz, for example, the RMS response over a complete sample period is potentially greater for a CMG operating continuously at this frequency than for a reaction wheel sweeping through the resonance. In terms of interferometric imaging, the CMG in this situation would produce "bad" data over the entire sample interval, whereas the RWA may produce only a few sectors of corrupted data as it is sweeps up and down, assuming uncompensated response in both cases. This is further addressed in the following section.

5.2.5 Approach to Minimizing ACS Disturbances

With the response data of the preceding subsection and knowledge of the disturbance spectra, a general approach to minimizing the effects of major ACS disturbers is discussed. Along a similar format to the power subsystem, the approach first attempts optical compensation (PCD's), progressing to passive techniques, isolation and damping, and investigates active CST tools as necessary. The ACS does not contain large area components which are sensitive to environmental pressure disturbances, and balancing massive vehicle elements for limiting gravity gradients is a system architecture issue. But as discussed earlier, control actuators must scale with large subsystem components to accommodate additional environmental disturbances, resulting effectively in a scaling of the ACS-generated disturbance spectrum. Again, the baseline configuration for OPTICS includes large area solar arrays and characteristic subsystem masses, thus this effect is included in the present analysis.

As expected, system response exceeds the performance criteria when a vibration of sufficient magnitude coincides with a resonant frequency of the structural plant. Reaction wheels have the potential for large variations in their operating velocity, corresponding to disturbances with wide spectral coverage from multiple harmonics. These include diminishing amplitude components approaching DC, with major amplitudes at higher frequencies, resulting in a swept response spectrum which is broadband, dropping off beyond $\approx$ 100 Hz. CMG's, on the other hand display more stable vibrational behavior, with discrete bands at harmonics of the wheel speed, starting at around 100 Hz for OPTICS, and amplitudes scaleable from the RWA model. Figure 5.32 illustrates the general characteristic of these disturbers.

RWA

Large space structures, thus demand larger and faster control flywheels, with disturbance amplitudes correspondingly greater than the nominal HST RWA model and at higher nominal frequencies. Pathlength compensation devices (PCD'S) for OPTICS, with a maximum bandwidth between 1 and 10 Hz, will not provide much attenuation from these disturbers. Figure 5.38 displays the net pathlength response to I-RWA disturbances versus PCD corner frequency, for the undamped system (ζ=0.1%) and damping ratios of 1 and 10%. The 10 nanometer performance level is also shown for reference. No substantial reduction is achieved with corner frequencies below 10 Hz. For PCD's with 1 and 10 Hz break frequencies, for example, residual net response to I-RWA module disturbances is 800 and 700 n-m RMS respectively, a meager improvement over the 803 n-m uncompensated response. Similar performance is expected for CMG's.

The high frequency behavior suggests isolation schemes. For the broadband RWA, a passive isolation system can be implemented which is sufficiently above the control bandwidth, but possesses adequate rolloff behavior to attenuate the higher amplitude effects, as has been successfully demonstrated on the Space Telescope program [10,18,42]. However, it presents a greater challenge for OPTICS, with a bending fundamental over an order of magnitude below HST, densely packed modes and larger unit disturbances. It is desired to use as stiff an isolator as possible for these control actuators to avoid excitation from energy spillover from ACS control commands, without sacrificing performance. For a control bandwidth of 0.01 Hz, a lower bound of 0.1 Hz is placed on the isolated system corner frequency, where a stiffer system, above 1 Hz say, is desired to prevent driving the plant dynamics.

I-RWA disturbances are filtered with isolators typical of those used on HST, as in the previous section, and the subsequent response is investigated. Figure 3.1 shows the general transmissibility function utilized. And isolators are implemented at the unit or module mount interface, where the *net* RMS response from three modules must be limited to 10 nanometers. Figure 5.39 shows the calculated net RMS pathlength response using isolators with corner frequencies between 0.1 and 100 Hz. Curves for structural damping ratios of ζ=0.1, 1 and 10 % are shown, and the 10 nanometer performance line is provided for reference. Peaks and valleys correspond to the isolator resonance sweeping structural modes, where the large response near 1 Hz is due to the isolator resonance coinciding with the vehicle fundamental modes. This figure shows that isolators no stiffer than 0.6 Hz be utilized to meet performance for the undamped plant. The addition of structural damping alleviates some of this burden, permitting isolators of a few Hz to approximately 5 Hz for ζ=1 and 10% respectively. It is seen that as little as 1% damping allows positioning of the isolator break frequency above the structural fundamentals, which is desirable.

As with the power disturbances, it is clear that multiple combinations of damping and disturbance isolation exist which meet performance. Detail design of these systems will reveal an "optimal" solution. However, to the first order, Figure 5.39 shows that a few percent damping in the structure and RWA module isolators of corner frequency at a few Hz will meet performance specifications. To illustrate this, a representative system of 1% damping and 3 Hz isolators is selected. The resulting power spectral density and maximum jitter responses are displayed in Figures 5.40 and 5.41.

Structural damping augmentation is also used to attenuate sharp resonant peaks of disturbance response. The maximum jitter response of Figure 5.41 shows that the 10 nanometer specification is exceeded at certain frequencies, as the I-RWA sweeps through structural resonances. This results in corrupted imaging data at discrete times, but with acceptable RMS performance over the net sample interval. The general effect of various amounts of structural damping on the maximum jitter response is investigated in the previous section for RTG disturbances. And because the RWA and RTG modules are located in close proximity, similar attenuation is expected. From Figure 5.15, and the isolated response of Figure 5.41, a factor of 7 reduction in jitter amplitude, corresponding to a structural damping ratio of $\approx$7%, brings the entire response within 10 nanometers for the 3 Hz isolator. Again, the RMS response is acceptable for this isolator at 1% damping, however, with additional damping augmentation, to ζ=7%, the intermittent peaks can be held within 10 nanometers to enhance overall image quality.

CMG

Utilizing isolators for CMG disturbances is somewhat more straightforward, with less residual response to contend with, particularly at lower frequencies. For the assumed model of CMG disturbances, response will be relatively flat out to 100 Hz, where it is expected to display jitter amplitudes on the order of 10 microns for the dominant harmonics. The simple isolator model of Figure 3.1 rolls off at $\approx$40 dB/decade and flattens out to 20 dB/dec after 1 decade. Thus, isolators with 1 and 10 Hz corner frequencies should provide 60 and 40 dB max attenuation at 100 Hz, resulting in 10 and 100 nanometers residual jitter respectively. With 1% damping augmentation, or nearly a factor of 3 amplitude reduction, and the 3 Hz isolator used for RWA's, jitter performance below 10 nanometers is achieved. Whether this is sufficient to meet RMS performance specifications depends on the modal content of the structure in this bandwidth, and the coincidence of structural modes with CMG operational frequencies. However, correlating with RWA performance measures, where peak responses are shown to be more difficult to curtail, this analysis indicates that CMG RMS performance should also be met with 1% structural damping and 3 Hz passive isolators.

Summary

Table 5.11 summarizes the important system design parameters for the ACS subsystem options considered: Improved RWA and Advanced CMG. The Advanced CMG system is selected for the OPTICS spacecraft as the leading design option for superior system mass and power efficiency to the I-RWA system. This is clear from the data in Table5.11, where the CMG system is approximately 43% of the I-RWA mass and demands 200% less power. Additionally, the I-RWA system is torque limited to 20 Nm, constraining the maximum translation velocity of siderostats to 0.1 m/s over 1 meter, due to the large reaction torque required for these quick maneuvers. This in turn doubles the time required for each siderostat translation (to 20 sec), constraining the available science time to roughly half that for the CMG system. To provide torque commensurate with available science time for CMG's, requires an I-RWA system of 3-4 times the system mass and power of that shown in the table, a prohibitive sum.

As far as disturbance minimization, the previous analysis indicates that a similar passive system of isolators with 3 Hz corner frequency and a structural damping ratio of 1% is sufficient to meet the required RMS performance specification for both systems. Additional damping augmentation is shown to improve image quality, but is not included here, as this represents performance beyond that specified. Isolators have frequencies similar for both options and can be implemented at the unit or module level. However, because isolator mass is proportional to the mass of the isolated unit, net mass for isolating I-RWA's is nearly 5 times that for CMG's, an additional system mass penalty. This is also included in the total system mass. Pathlength compensation is shown to provide minimal attenuation for these disturbers, due to the inherent higher frequency behavior (see Figure 5.38), but is included as a common system element. Therefore, it is clear that an ACS subsystem utilizing CMG's for control actuation is the superior candidate for OPTICS.

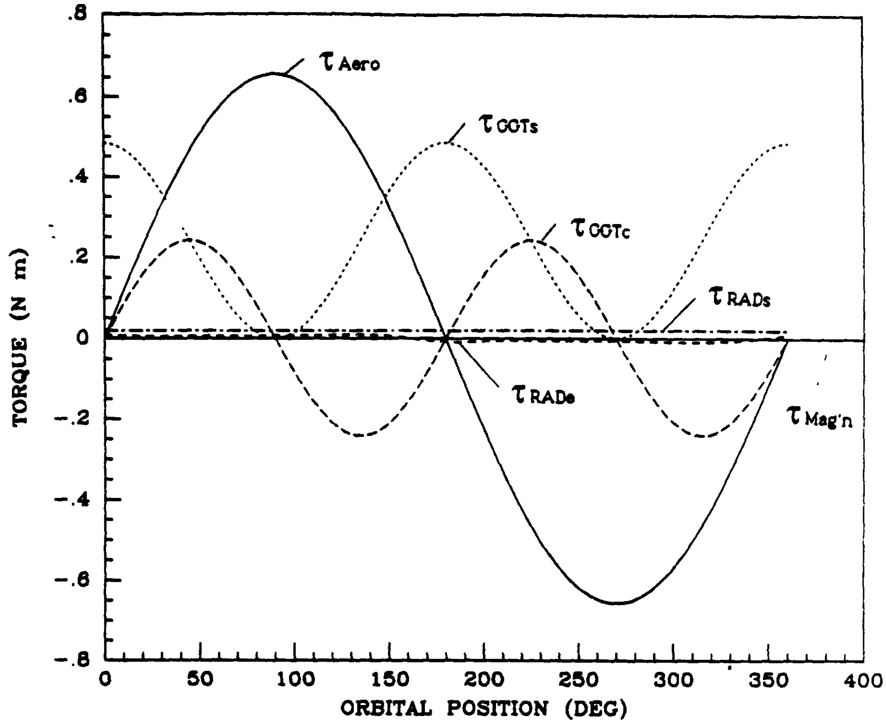

Figure 5.25: Approximation for Environmental Disturbance Torques Over One Orbit: 400 km Altitude.

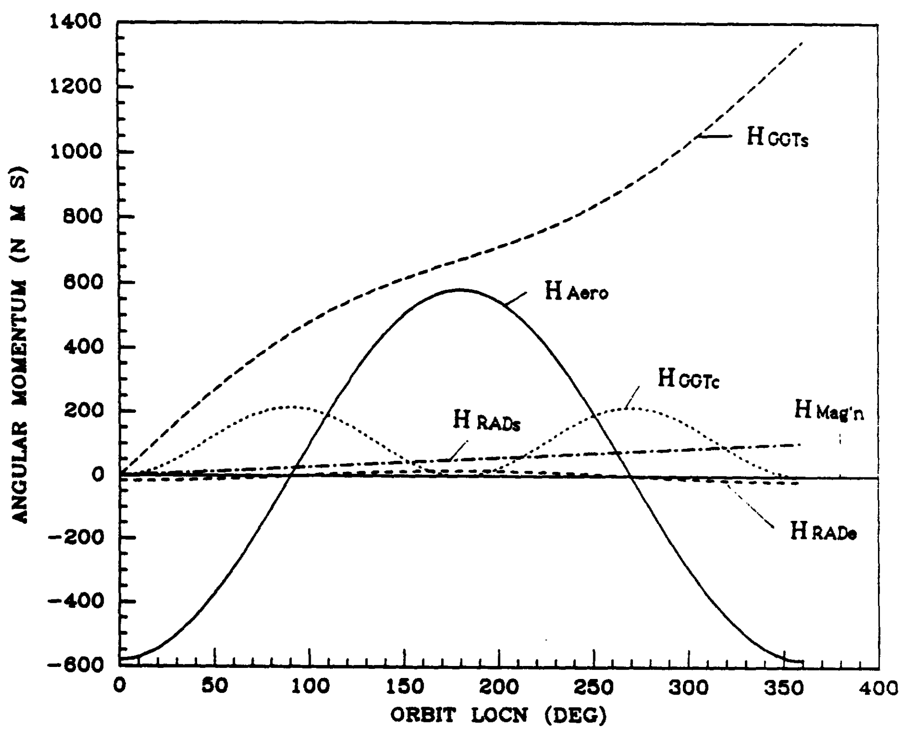

Figure 5.26: Approximation for Environmental Disturbance Angular Momentum Over One Orbit: 400 km Altitude.

Table 5.8: ACS Actuator Torque / Angular Momentum Requirements

Source		*Torque* *(N m)*	*Momentum* *(N m s)*
A. Environment:	(400 km orbit)		
	1. Aero	0.660	580
	2. GGT (cyclic)	0.230	210
	(secular)	0.250	1450
	3. Rad'n (solar)	0.019	103
	(earth)	0.009	17
	4. Magnetic	0.001	1
Sum:	(cyclic/secular)	1.13/0.27	808/1553
B. S/C Maneuver:			
	90 deg /60 min	0.61	1100
C. S/A Track:			
	90 deg /60 min	*small*	*small*
D. Siderostat Transl.:			
	$0.05 m/sec$ (max)	13.30	180
Sum (RSS)	(cyclic/secular)	13.40/0.27	1380/1553
50% Contingency		6.60/0.13	690/776
Total (per axis)	(cyclic/secular)	20.0/0.4	2070/2330

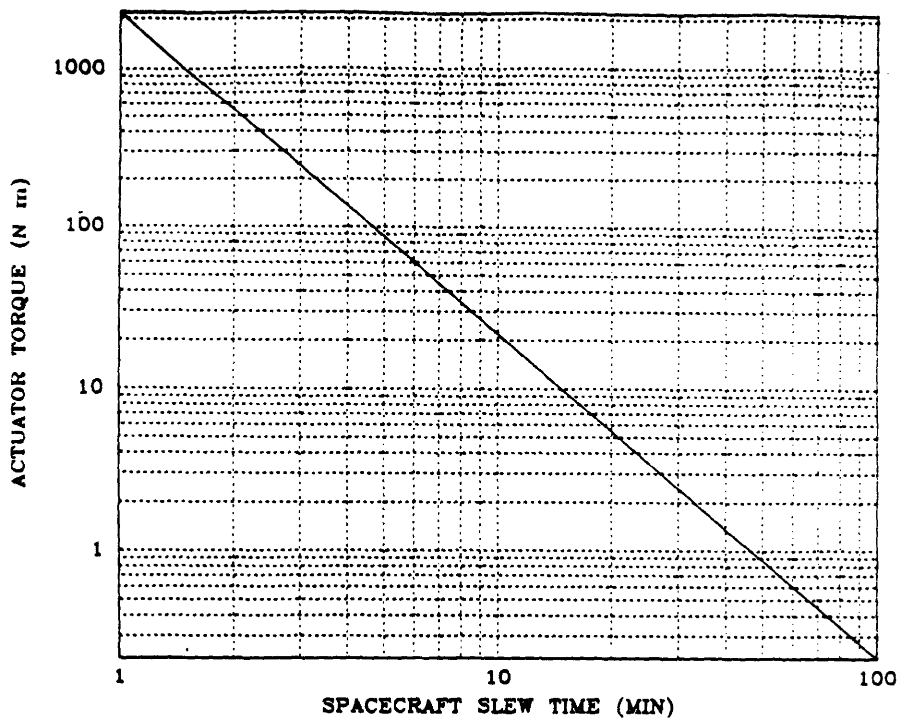

Figure 5.27: ACS Actuator Torque vs. Time Required to Slew Vehicle 90 degrees.

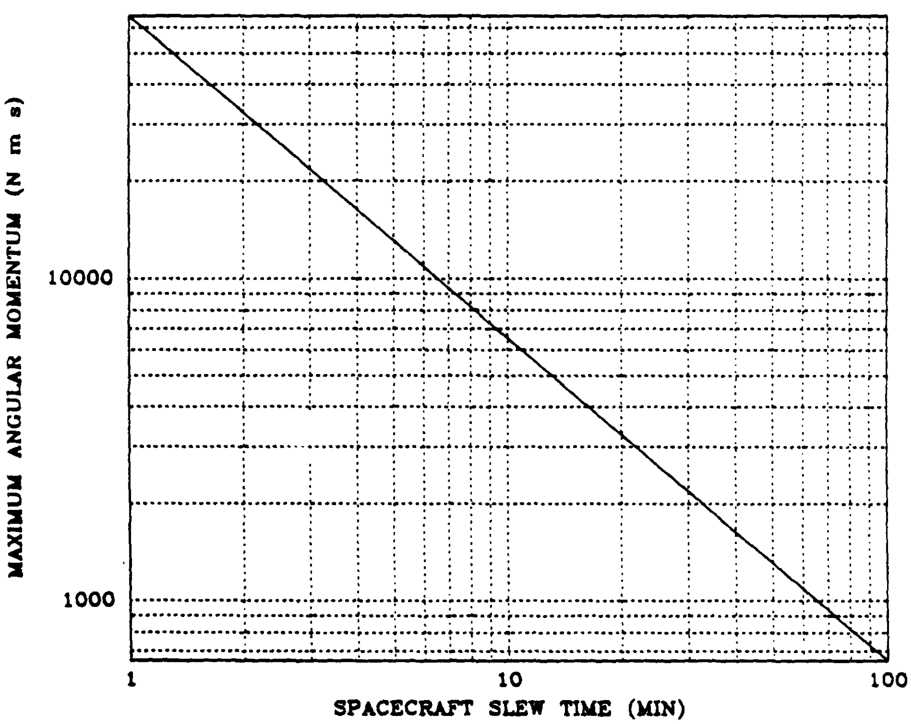

Figure 5.28: ACS Actuator Maximum Angular Momentum vs. Time Required to Slew Vehicle 90 degrees.

Table 5.9: Preliminary Design Parameters For ACS Options

Power Subsystem Option:	*Performance*	*Physical / Dynamical Characteristics*	*Disturbances*	*CST / Subsystem Considerations*
I. Passive Stabilization:	generally low			Performance too low for primary control - may augment active system
1. Spin-stabilized:	0.1 degree accuracy	Req. Dominant Inertial Axis		
2. Gravity gradient:	1-3 degree accuracy	Earth-pointing	E - Sensitive to higher order Aero / GGT terms	
3. Aero/solar pressure:		Earth-pointing		
4. Dual spin:		Req Dominant Inertial Axis	L,M,H,R - Electromech Spin bearing	
II. Active Stabilization:				
1. Reaction Wheels (RWA):	<0.01 degree accuracy 0.5-2.0 Nm / 260-600 Nms 50 Hz BW 4-6 Nms/kg; 40-50 kg/Nm 0-6000 RPM max 10-15 yr life	Rotating flywheel / electronics unit; Variable speed	L,M,H,R - Radial and axial forces and torques: torque motor ripple & cogging, rotor imbalance, bearing imperfection R - Thru-zero friction R - Friction for gimballed versions	Acurate knowledge of momentum vector req'd; Heritage
2. Momentum Wheels (MWA):	similar to RWA 2500 Nms / 0.2 Nm 7-30 Nms/kg 200-400 kg/Nm	Rotating flywheel / electronics unit; Variable speed	Similar	Acurate knowledge of momentum vector req'd; Heritage
3. Control Moment Gyro (CMG): (Single Gimbal)	<0.01 degree accuracy 2000-5000 Nms 3000-7000 Nm 10-20 Hz BW 6-15 Nms/kg / 0.17-0.04 kg /Nm 6000 RPM; 5-7 yr life	Rotating flywheel / electronics unit; Constant speed; Gimballed	Similar - generally higher rotational velocities (~2X RWA); R - Gimbal friction	Acurate knowledge of momentum vector req'd; Heritage
(Double Gimbal)	similar to SG-CMG 400-4000 Nms 1-10 Nm 6 Nms/kg 70 kg/Nm	Similar	Similar	Acurate knowledge of momentum vector req'd; Heritage
4. Magnetic Torquers:	> 1 degree accuracy low torque: 0.1 N m max 4000 A m2 (state-of-art) 650 Nms per orbit	Long, electromag coil rods; (250 cm, 7.6 cm dia, 50 kg)	Magnetic field generated	Heritage Some sensors sensitive to Mag'n
5. Propulsion (thrusters):	0.1 degree accuracy < 1 N - cold gas (chem) > 5 N - hot gas (chem) 0.001-1 N (elec)	Thrust engine; plumbing; fuel tanks; propellant mgmt.	E,L,R - Thrust, imperfections I - Propellant slosh L,M,H,R - Pumps, Flow noise	Contamination from effluent Structural / Fluid interactions Heritage

Table 5.10: Preliminary Attitude Control Subsystem Design

Component	*Description*	*Qty*	*Unit Mass (kg)*	*Total Mass (kg)*	*Avg Power (W)*
Sensors:					
Sun Sensor:	HST Heritage	3	3	9	15
Magnetometer:	3-axis; HST Heritage	2	2	4	5
Fixed Head Star Tracker: (FHST)	8 x 8 degree FOV; HST Heritage	3	15	45	70
Rate Gyro Assemblies: (RGA)	HST Heritage	6	18	108	100
Fine Guidance Interferometer: (FGI)	3 Telescopes; Combining Optics	1	90	90	50
Actuators:					
Control Moment Gyro: (CMG)	Sperry M1700 Heritage 4150 Nm / 2300 Nms	3	155	465	195
Reaction Wheel Assembly: (I-RWA)	HST RWA Heritage 2 Nm / 500 Nms	30	72	2160	1350
Momentum Management:					
Magnetic Torque Rods:	4000 Am^2; 0.1 Nm; 650 Nms per orbit	12	50	600	200
TOTAL:	I-RWA System			3016 kg	1790 W
	CMG System			1321 kg	635 W

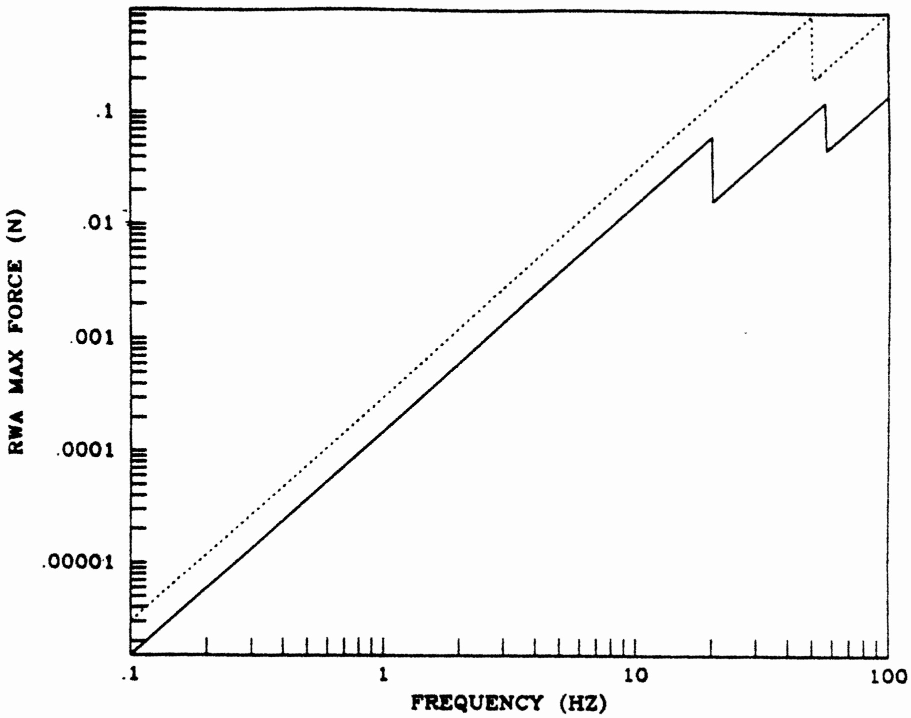

Figure 5.29: Nominal and Improved-HST RWA Maximum Force Model.

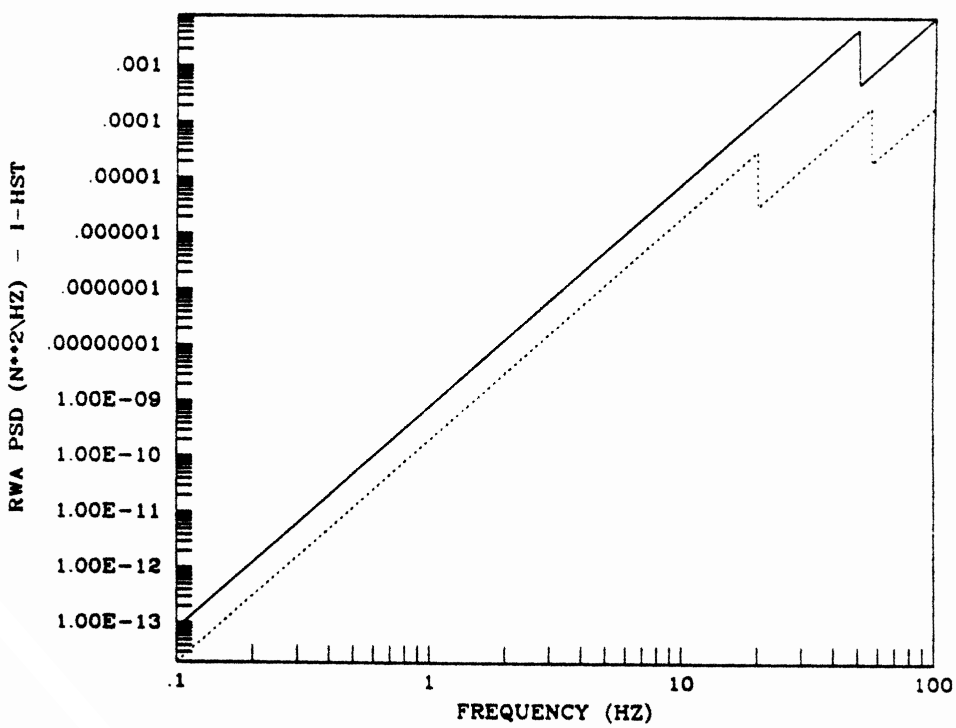

Fig. 5.30: Nominal and Improved-HST RWA Force PSD Model.

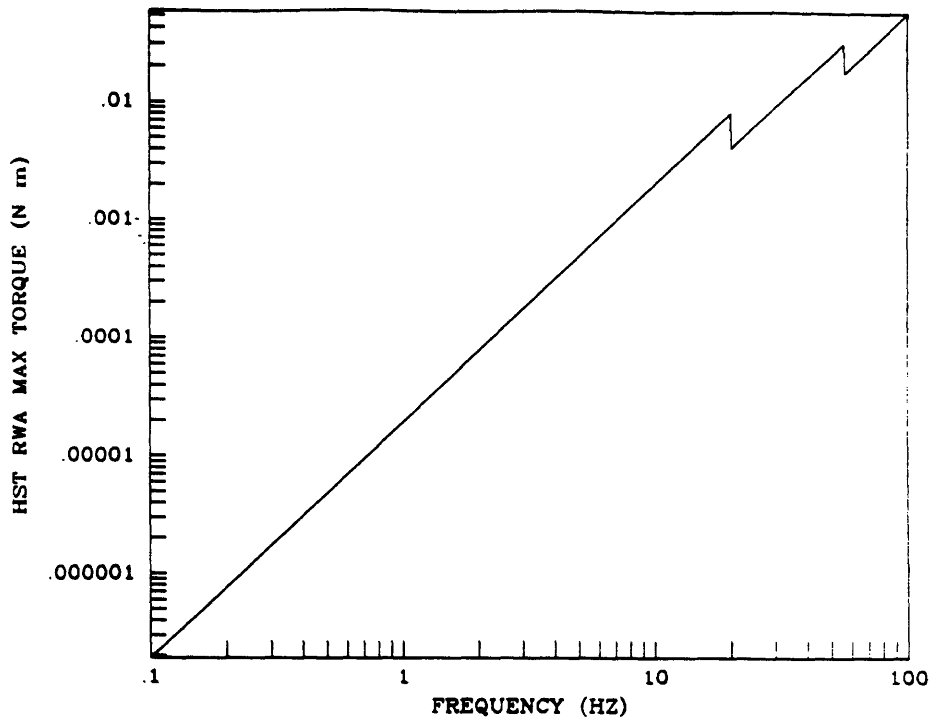

Figure 5.31: Nominal HST RWA Maximum Torque Model: (0-1200 RPM) .

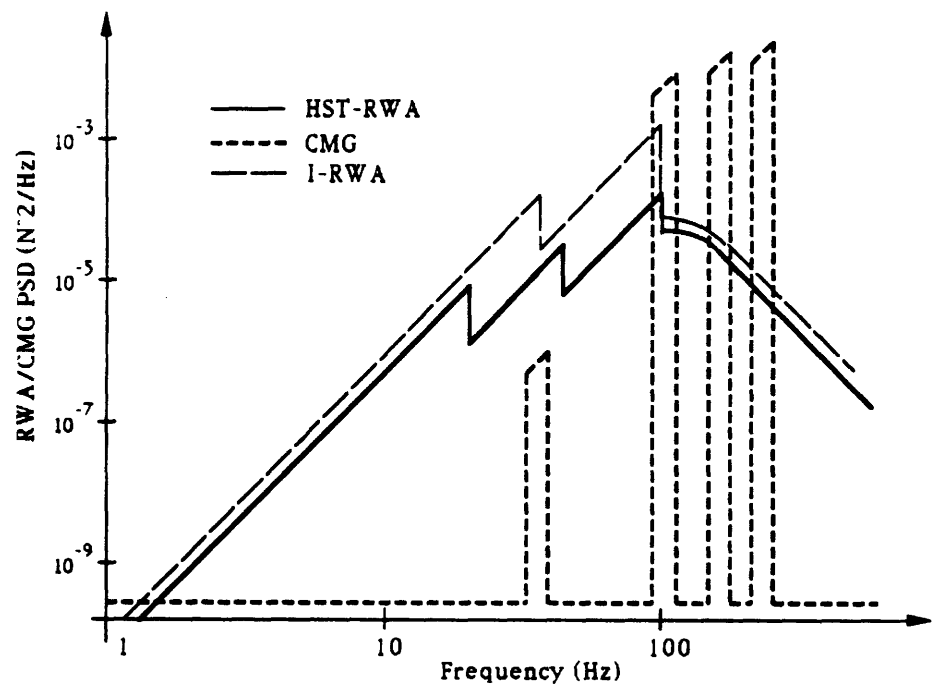

Figure 5.32: Extrapolation to Advanced CMG Force Model: (3X HST-RWA Mass, 6000 RPM).

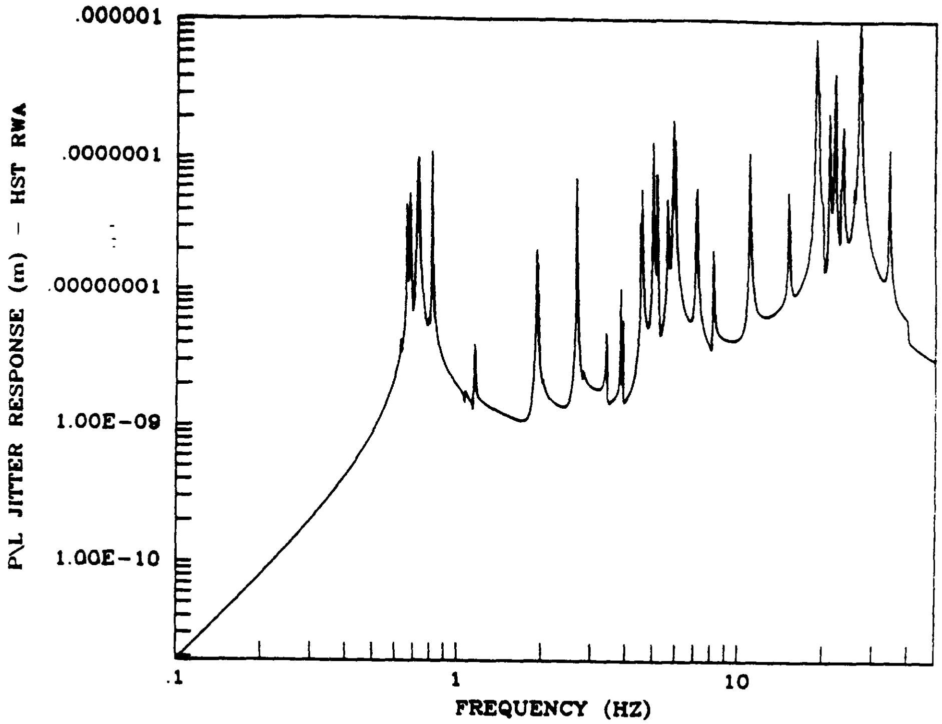

Figure 5.33: Pathlength Jitter Response to Nominal HST RWA Maximum Force Model (0-1200 RPM).

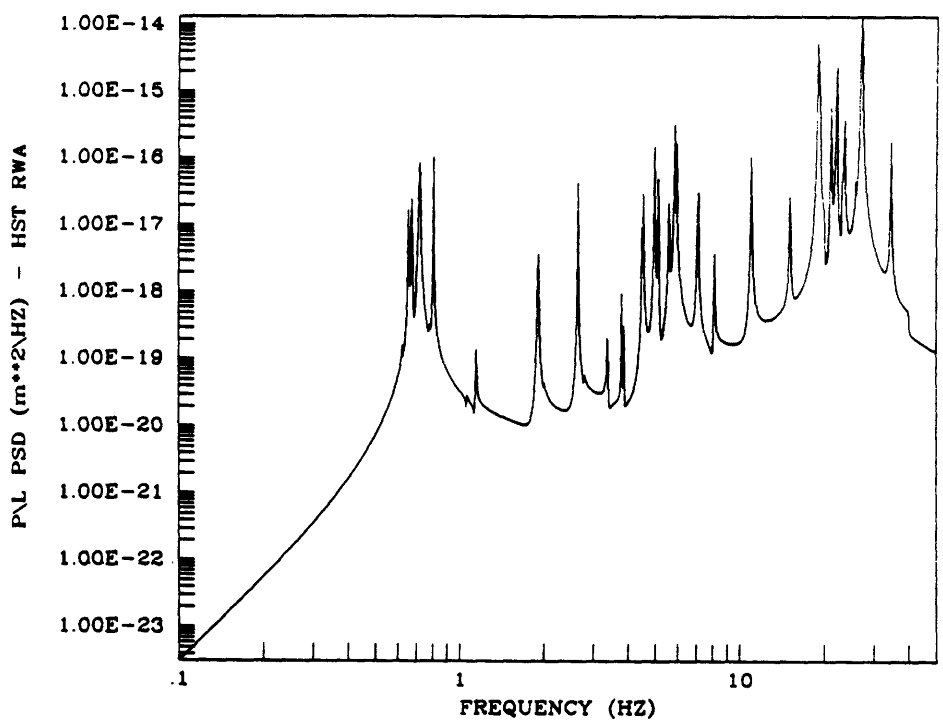

Figure 5.34: Pathlength Response PSD to Nominal HST RWA Force PSD Model (0-1200 RPM).

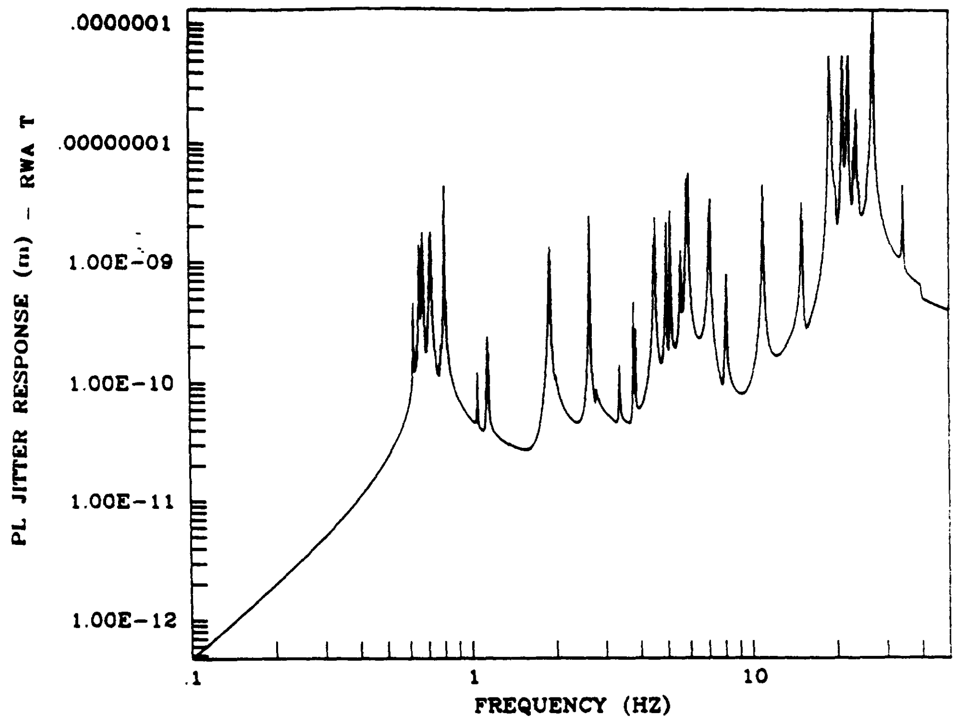

Figure 5.35: Pathlength Jitter Response to Nominal HST RWA Max Torque Model (0-1200 RPM).

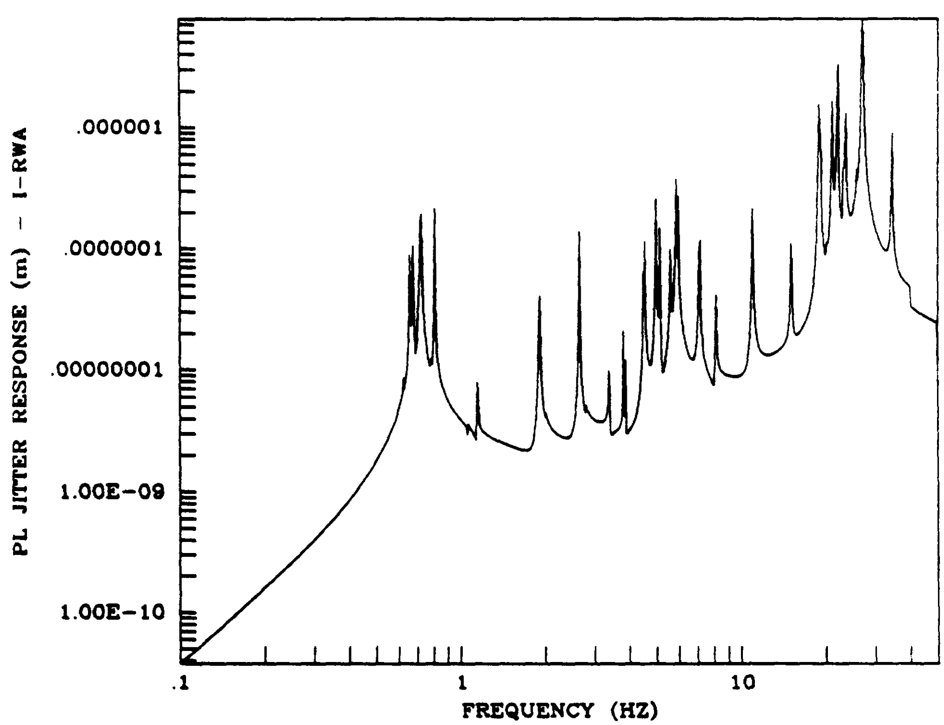

Figure 5.36: Pathlength Jitter Response to Improved RWA Max Force Model (2X Mass, 0-3000 RPM).

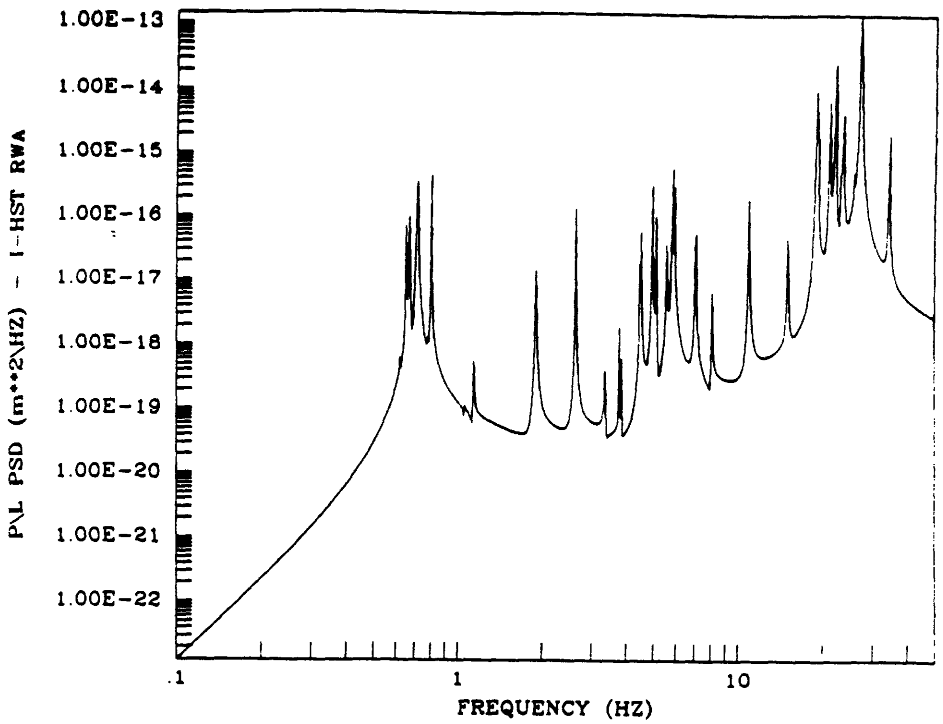

Figure 5.37: Pathlength Response PSD to Improved RWA Force PSD Model (2X Mass, 0-3000 RPM).

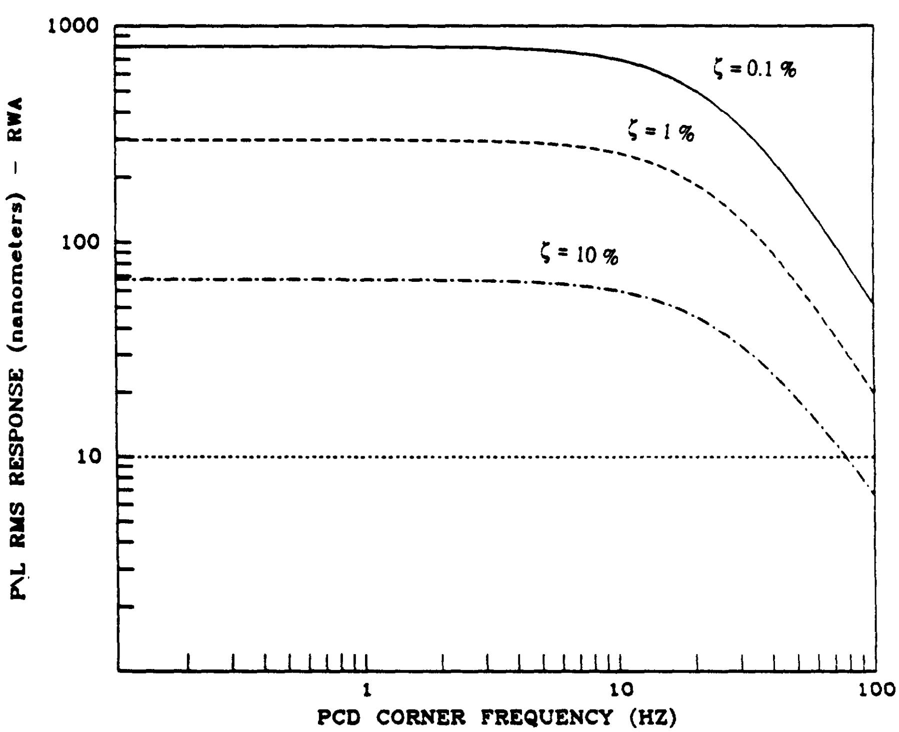

Figure 5.38: Pathlength RMS Response versus PCD Corner Frequency for Structural Damping Ratios of: ζ =0.1, 1 and 10%.

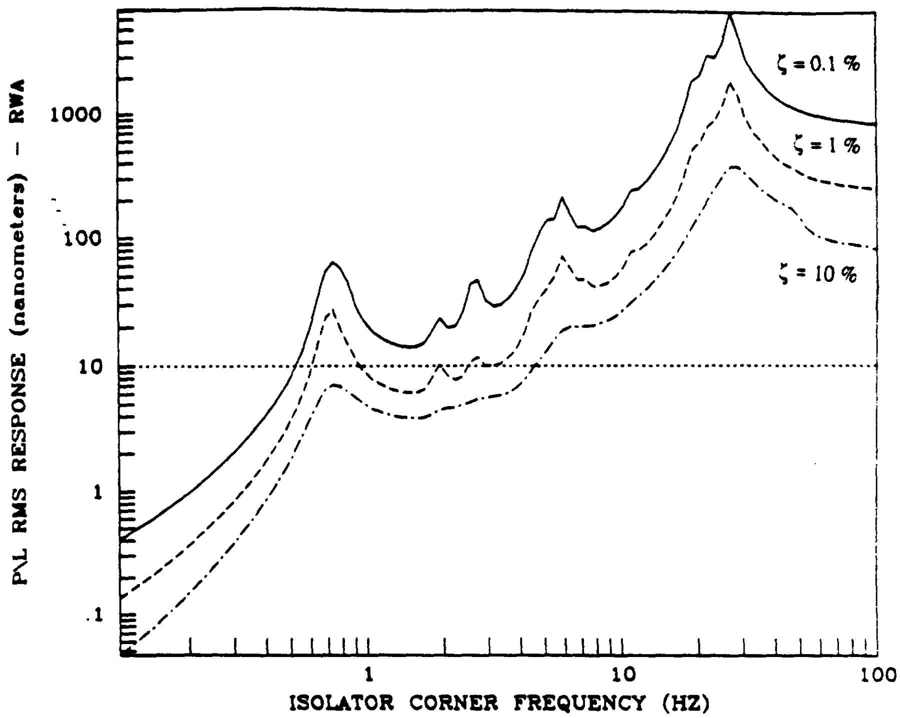

Figure 5.39: Pathlength RMS Response versus Isolator Corner Frequency for Structural Damping Ratios of: ζ =0.1, 1 and 10%.

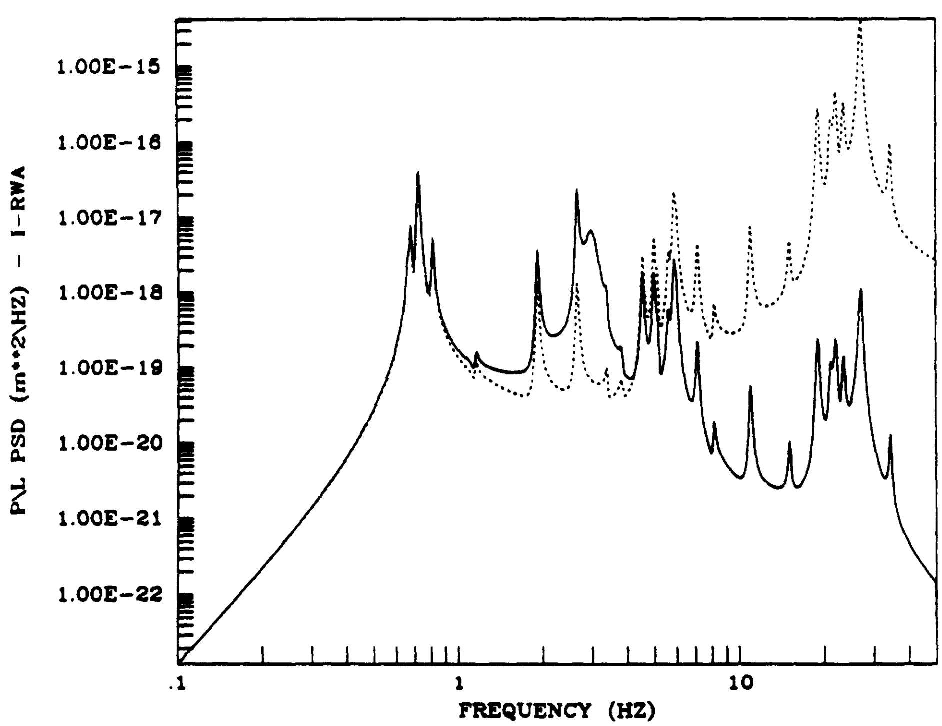

Figure 5.40: Pathlength Response PSD to I-RWA Disturb's: ζ=1% and $(\omega_c)_{isol}$=3 Hz.

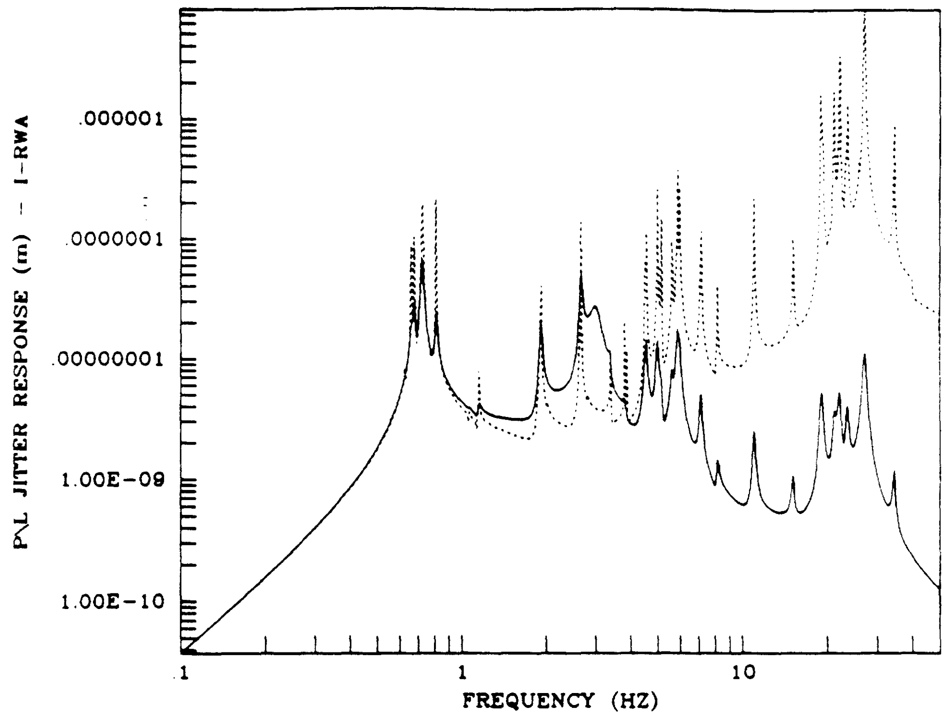

Figure 5.41: Pathlength Maximum Jitter Response to I-RWA Disturbances for: ζ=1% and $(\omega_c)_{isol}$=3 Hz.

Table 5.11: ACS Subsystem Design Summary

Parameter	*Improved-RWA System*	*Advanced CMG System*
1.Primary Elements (Qty):	RWA's (30), Magnetic Torquers (12), Sensor Complement	CMG's (3), Magnetic Torquers (12), Sensor Complement
2.Total Subsystem Mass:	3016 kg	1321 kg
3. Net Actuator Capacity: (per axis)	20 Nm / 5000 Nms	4150 Nm / 2300 Nms
4.Total (Avg) System Power:	1790 W_E	635 W_E
5.Disturbance Types:	L,M,H,R - Steady State/Swept	M,H,R - Steady State
6.On During Science:	YES	YES
7.Pathlength Response: (nanometers) Max Jitter:	8 micron	10 micron
RMS:	803 n-m	?? n-m
8.Recommended CST Tools:	PCD Control: 1 Hz Structural Damping Ratio: 1% Isolation: 3 Hz	PCD Control: 1 Hz Structural Damping Ratio: 1% Isolation: 3 Hz
9.Mass of CST System:	M_d + (5) M_i	M_d + M_i
10.CST Complexity:	Low-Med	Low-Med
11.MISC Constraints:	Constrains Maximum Siderostat Velocity to 0.1 m/s: 50% Science Time	100% Science Time

5.3 Interferometer and Metrology Subsystem

The purpose of this section is to investigate disturbances inherent to elements of the Interferometer and Metrology (I&M) subsystem, system performance (differential path-length) response to these disturbers, and approaches to minimizing their effects consistent with subsystem requirements. The previous two sections represent design and disturbance minimization approaches for major *bus* subsystems; Power and ACS generally place the greatest impact on the system design, and are of the greatest disturbers on the vehicle. Whereas, this section evaluates the *payload* subsystem for an interferometric-class spacecraft. It is therefore different from the other sections in that design options are not traded, but looks at the previously defined elements of the OPTICS interferometer and metrology systems. The approach is otherwise as before.

This spacecraft payload is the prime objective of the mission and inherently drives the requirements for OPTICS, and its' subsystems. However, due to interactions with the other subsystems and general mission performance demands, system requirements are also levied on the I&M subsystem. These are outlined in Table5.12.

Table 5.12: Optics and Metrology Subsystem Requirements

Interferometer Requirements:	
Optical Interferometer:	3 milli-arcsec Imaging and Astrometry
Imaging:	Full (100%) U-V Plane Coverage
Guidance Interferometer:	milli-arcsec Resolution; 1 nanometer Accuracy
Positional Accuracy:	50 nanometers RMS - Imaging
	10 nanometers RMS - Astrometry
Angular Accuracy:	1-10 milli-arcseconds
Metrology Requirements:	
Starlight Internal Pathlength Monitoring	
Siderostat and FGI Baseline Monitoring	
Laser Interferometer:	1 nanometer Accuracy
Structural Requirements:	
PL Jitter Budget:	10 nano-meters RMS
Transient Vibrations:	Settle to 10 n m in <10 sec

The interferometer and metrology requirements are derived in Chapter 4, as well as the structural vibration budget, shown in the table. The performance measure used in this study, again, is differential pathlength error for two science light paths between the siderostat collectors and fringe detector. It therefore captures only the pathlength error components internal to the spacecraft, including the internal flexible-local and some of the internal flexible-global components (see Chapter 4).

The relationship between the I&M subsystem, CST and the flexible OPTICS vehicle centers around the interdependency between I&M and the pathlength/structural control systems, and the disturbances and dynamical interactions introduced by I&M elements. Interferometer performance, ie. the mission performance metric, is directly dependant upon the capability of the net disturbance minimization scheme, including optical compensation (PCD's), command shaping of controlled elements, and all passive and active CST tools discussed in this thesis. This holds for both the science and guidance interferometers. But, the capability of these techniques is inherently limited by the availability of data on the errors which they must compensate, and as thus rely on the laser metrology system and guidance interferometer as the only means for providing error data at the required 1 nanometer accuracy. Along the theme of this chapter, this section does not attempt to investigate the details of interferometer and metrology system design, particularly with respect to optical instruments and their operation, fringe acquisition/tracking and image reconstruction, and the many real engineering challenges associated with a fully functional OPTICS I&M subsystem. Rather, the investigation continues to focus only on those aspects associated with disturbances and dynamical interactions introduced by I&M subsystem components, and the effect of these on system performance. Top level architecture and major elements are outlined to evaluate the system as a whole, leaving particulars of the detail design to further investigators.

5.3.1 I&M Subsystem Description

Figure 5.42 shows the top level functional block diagram for the I&M subsystem, for two dimensions. The I&M subsystem, as its' name implies, is composed of two distinct systems. The Interferometer system includes elements for the science interferometer (SI) and fine guidance interferometer (FGI), and the Metrology system is composed of components for precision laser measurement (position and rotation) of critical interferometer elements. A description of the major subsystem elements and integrated operation of both systems is discussed.

The OPTICS science interferometer has three, 1.0 meter diameter collecting telescopes, or siderostats, configured about one face of the tetrahedron, the view plane, which re-

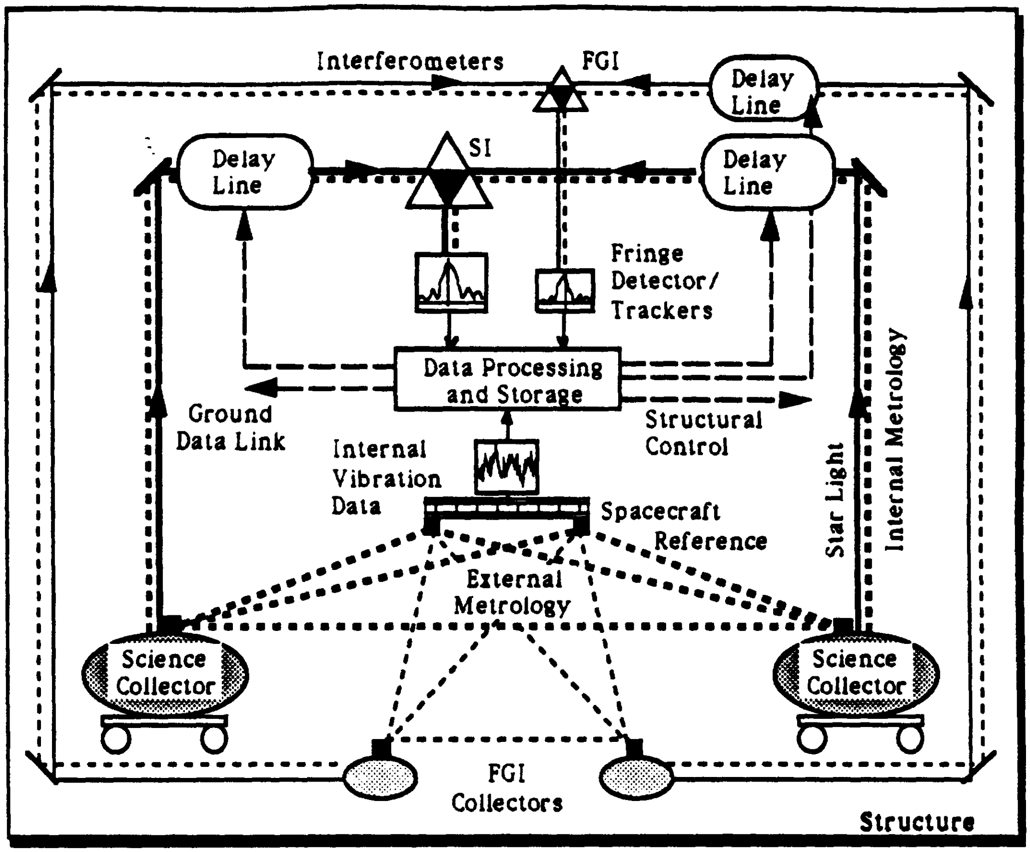

Figure 5.42: Functional block diagram for the I&M subsystem, shown for two dimensions.

ceive light from the targeted celestial object. Figure 5.43 displays the vehicle layout for siderostats and other major I&M elements. To map the U-V plane in imaging mode, siderostats are translated along their respective truss legs to obtain each of the unique baseline configurations for three collectors in a triangular array. Light beams are focused to manageable diameters ($\approx$1 centimeter) by the telescopes and directed along the truss legs, through pathlength equalization devices, and combined on a detector at the combining platform. Interference patterns are created by coherently combining pairs of the three light beams onto the detector, measuring magnitude and phase of the visibility function. Nominally, pathlength compensation devices (PCD's) are needed only to equalize internal paths of the two combined light beams as siderostats traverse the truss legs of the view plane. For a completely rigid structure, with optics in absolute alignment and vehicle attitude with respect to the science star perfect, the interference pattern on the detector remains stationary with the primary fringe centered, and uncorrupted data is produced.

The vehicle is flexible, however, optics jitter out of alignment and errors exist in the spacecraft attitude. Thus, measures are needed to account for these imperfections. Metrology provides this data.

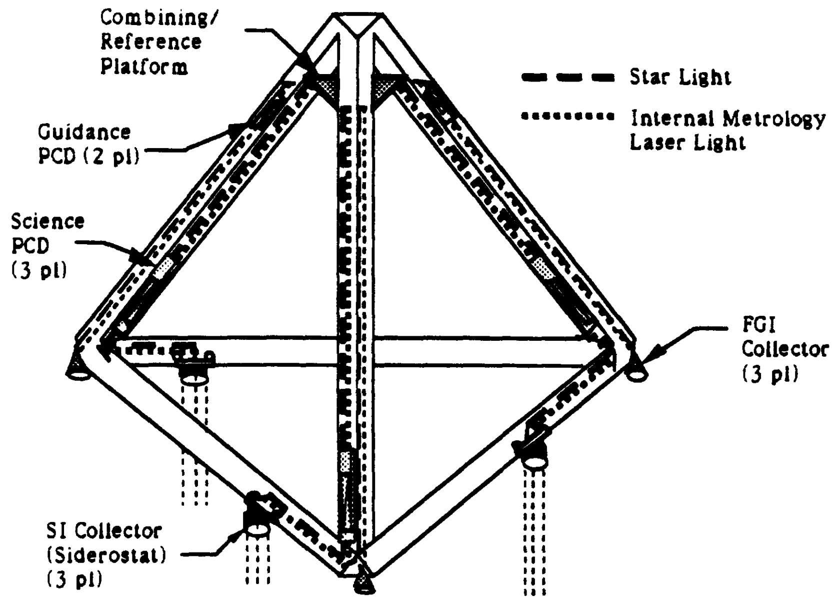

Figure 5.43: Vehicle layout for major elements of the Fine Guidance and Science Interferometer systems, showing coincidence of internal laser metrology and stellar light paths.

Changes in the differential pathlength and wavefront tilt produce phasing errors in the visibility function, resulting in image distortion. As discussed in Chapter 4, the major sources of these errors are from: internal flexibility effects that the light beams encounter between the siderostats and the detector, including erroneous vibration and deformation of all steering optics; external rigid body errors due to attitude variations of the entire vehicle; and global internal flexible effects which contribute to internal errors, siderostat baseline deviations and relative errors between the collectors and spacecraft reference. Refer to the functional diagram of Figure 5.42. For measuring the first type of error, internal flexible-local, internal laser metrology is employed. To sense these errors, light from a laser interferometer is sent down the identical optical path as the science light, bouncing off all of the same mirrors and waveplates between siderostats and detector, to detect net differential displacements of the internal paths. This data is then available to controllers, PCD's for example, to compensate these errors.

Internal metrology can only measure the pathlength changes internal to the vehicle structure. Rigid body rotations of the spacecraft from external disturbance sources cause the collectors on different parts of the structure to move with respect to the star, thus changing the effective baseline vectors and external pathlengths, or the portions of wavefront being sampled. To sense these errors requires a precision attitude sensor, of which only stellar interferometers can provide the necessary precision. Thus, the fine guidance interferometer (FGI) is required, as discussed in the previous section as an ACS sensor. Three dedicated collectors, 0.5 m diameter, are fixed at the extremes of the view-plane apexes, operating similarly to the science interferometer. Light from a bright guide star is collected by the guidance telescopes, directed through pathlength equalizers and combined in pairs on a detector at the combining platform to achieve the required two axes of attitude data. Internal metrology is similarly employed to measure internal variations in the guidance paths. With knowledge of the net pathlength error from the guidance star fringe trackers, and the measured internal flexible effects from internal metrology, the error due to rigid body attitude deviations is obtained. In other words, the FGI and its' associated internal metrology fixes a vehicle rigid-body reference with respect to the guide star. To correlate this reference with the science interferometer collectors and measure the third type of error, internal flexible-global, requires an external laser metrology system.

Figure 5.44 shows the minimal required external metrology system for measuring pathlength displacements; measurement of tilt can be accomplished at the detector, and is not included. Precision laser interferometers are used to detect changes in the distance between guidance collectors, between guidance collectors and the vehicle reference, vehicle reference and science siderostats, and between science siderostats. Clearly, when enough relative measurements are taken, positions of the various critical elements of the interferometer systems are all known with respect to each other, thus producing a determinate laser truss network. The total metrology system, then fixes the science siderostat positions with respect to the science star through the metrology systems and FGI, determines baseline vectors between science collectors and between FGI collectors, and provides measurement data for all of the internal and external errors. It is assumed here [37,22] that laser metrology systems have been investigated thoroughly enough to prove their feasibility, and appear to pose no severe technical barriers to achieve the required 1 nanometer measurement accuracy.

5.3.2 I&M Subsystem Disturbances

I&M subsystem disturbances are outlined in Chapter 2, showing several elements as major disturbers: siderostat carriage mechanisms which translate massive collecting telescope

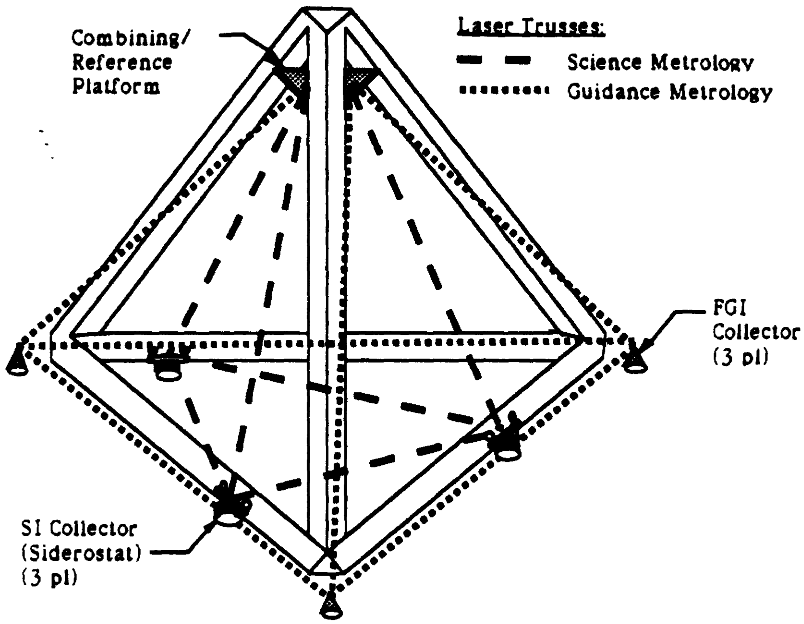

Figure 5.44: External metrology system for OPTICS showing the minimal laser "truss" network for differential pathlength measurement.

assemblies over entire lengths of the OPTICS view plane; pathlength compensation devices which contain a similar coarse translation capability, but at a fraction of the siderostat distance and mass; gimballed primary and fast steering secondary mirrors for compensating wavefront tilt errors; and the large amounts of thermal energy from inefficient, high precision metrology gas lasers and electronics. Disturbances from the translating siderostats are the only effects reviewed here, representing the major contributors from this subsystem.

A carriage assembly houses the science siderostats and provides the mechanism for coarse translations along the truss legs on a rail system. The carriage/rail system need only provide very coarse positioning of telescope assemblies, because accurately quantized siderostat locations are not required as long as the baseline vector is precisely measured, which the laser metrology takes care of. This system is envisioned to include some type of timing belt, cable driven assembly, or a motorized cart, similar to the pathlength compensation mechanisms, but larger. PCD's also require the translation of a mirror assembly over large distances. But these can take advantage of multiple folds in the light path to reduce the net translation distance, and subsequently have lower maximum velocity and induced disturbances.

Two major disturbance types are thus derived for siderostats and PCD's: transient inertial loads from the rapidly accelerated masses, and a broadband spectrum covering all of the mechanization and imperfection vibrations of quasi-discrete force spikes varying with translational velocity. The nominal imaging scenario has two science siderostats collecting photons while the third is repositioning itself to a new baseline. Immediately following the 10 second sample interval, optical switching pairs up the previously moving siderostat with one of the stationary ones to begin the next sample interval. And the now unpaired collector begins its translation. For full U-V plane coverage, the nominal translation distance is 1 meter per move, and must be accomplished in 10 seconds or less to not constrain the available science taking time, as discussed in Chapter 4.

As seen in the previous section, it is the requirement to rapidly translate siderostats that is a large driver in the sizing of ACS actuators. To counteract this inertial load, requires control torques which are proportional to the acceleration of the siderostat. Assuming a constant vehicle torque profile (or siderostat acceleration), similar to that for solar array command torques in Figure 5.5, a ramped velocity profile results, with peak velocity occurring midway through the translation. Figure 5.47 displays the relationship between maximum siderostat velocity over the 1 meter translation, the necessary vehicle reaction torque about an axis normal to the view plane, and resulting differential pathlength error. A 180 kg siderostat assembly translating 1 meter along a truss leg with a peak velocity of 0.1 m/sec applies approximately 18 Nm constant torque to the vehicle, about an axis normal to the view plane. This is the design criteria for torque-limited RWA's in the previous section, which places a 2:1 time constraint on the available science time. For the OPTICS CMG's, however, siderostat translation velocity is not constrained by the level of available reaction torque, and therefore no limit on science time is seen. For this case, the necessary 0.2 m/sec maximum velocity is realized, generating roughly 72 Nm torque, to be reacted by the vehicle. The coarse mode of PCD's, as mentioned, are very similar in operation to siderostat carriages, but with a throw mass almost two orders of magnitude less. This effect is certainly very important to the local dynamics, however for the current first order investigation of the global dynamics, the dominant siderostat disturbances are only evaluated.

Previously indicated in Chapter 2, vibration data does not exists for a space-based interferometer carriage mechanism because none have ever flown, nor been developed through detail design. The general form and magnitude of their disturbance spectra may be construed, however from the mechanization and experience from terrestrial interferometer trolleys [26], as discussed in Chapter 2. Both the siderostat and PCD mechanisms may generate disturbances from the operation of electromechanical motors, meshing of gears, circulation and imperfections in bearing assemblies, and friction between sliding components. These are manifested mainly in the form of semi-discrete force spikes, in the frequency spectrum, at multiple harmonics of the translation velocity, and may include a random component from friction. So, when the siderostat velocity ramps up and down during its 1 meter translation, the discrete force components sweep the frequency spectrum, not unlike reaction wheel disturbances. Short of a more detailed analysis or availability of experimental data, it is difficult to construct an accurate and representative disturbance spectrum displaying this behavior. And due to the time-varying nature of the carriage velocity, it is not appropriate to simply utilize disturbance data for a constant velocity mechanism ([26]). Thus, they will be approximated conservatively here as white noise over the model bandwidth, at magnitudes scaled from the Mt. Wilson data, and proportional to the carriage velocity: for a maximum velocity of 0.2 m/sec, a random force of 100 milli-N RMS (0.1-100 Hz) is assumed. Figure 5.45 displays the assumed model for this disturbance.

5.3.3 System Response to I&M Disturbances

Open loop responses to I&M disturbances are investigated, focusing on the dominant siderostat inertial loads and mechanism vibrations. Referring to Figure 5.47, is is clear that large pathlength errors will result over the course of each siderostat maneuver, showing nearly 10 microns of motion for the required 72 Nm constant reaction torque. For sequential sampling, these errors will be relatively cyclic as each individual telescope accelerates and decelerates over 1 meter, but not necessarily in phase. The transient response following each maneuver, then will contribute to the net error of the following motion. Clearly, if these errors are allowed to go uncompensated, the net response may quickly grow quite large. Therefore, the requirement to settle within 10 nanometers in less than 10 seconds (one sample interval) is conservatively imposed. Because transient response is of principle concern here, the time domain is primarily utilized. The same model configuration as in the previous sections is utilized.

As a first cut, a 10 second torque command with profile similar to Figure 5.5 and magnitude equal to one third of 72 Nm (24 Nm) is issued at each of three ACS actuator locations, reacting an accelerating siderostat at the middle of one view-plane truss leg. A random vibration with normal distribution and 100 milli-N RMS maximum amplitude (Figure 5.45) is also included at this midleg location in three coordinate directions to represent mechanization disturbances. The resulting time response is seen in Figure 5.48, where the plot resolution clearly captures only the dominant structural frequencies. As expected, the maximum response is over two times the static error associated with this level of torque; this is due to both the transient behavior and the additional random disturbance. Further investigation of contributors to error, not included here, shows that the response to the random vibration is a factor of ten below that for the reaction to siderostat torquing, but with different frequency content. The frequency response from a disturbance force at this siderostat location to differential pathlength error is seen in Figure 5.46. Dominant disturbance spikes are expected to occur at approximately 1 Hz and above, at maximum amplitudes of a few hundred milli-N. From Figure 5.46, this corresponds to roughly a few microns of peak pathlength vibration, which was seen in the time simulations for these disturbances.

The torque command of Figure 5.5 does not represent the best shaping for this maneuver. However, it is a good first approximation for a command requiring constant torque over a length of time. A factor of almost three reduction in residual peak amplitude is possible using a simple sine wave torque command. This is seen in Figure 5.49, where, to achieve the same 1 meter translation in 10 seconds, requires 226 Nm maximum torque. Clearly, the residual amplitude is reduced, but the during-command maximum amplitude is higher due to a more efficient input of energy and greater maximum torque, respectively. Further, minor reductions in residual amplitude are possible with better shaped commands, however, as seen here, it is difficult to improve on the commanded response. Response to the sine wave torque command with random mechanization disturbance (Figure 5.49) is thus used as characteristic for further investigation.

5.3.4 Approach to Minimizing I&M Disturbances

For the reduced, dominant set of I&M disturbances, siderostat inertial loads and mechanization vibrations, minimization schemes are investigated for meeting subsystem performance requirements. The approach is as in the previous sections, looking at pathlength optical compensation (PCD's), damping augmentation, and passive techniques prior to the more aggressive active CST tools.

PCD's, at a minimum, should be able to put a good dent in the pathlength error due to the commanded torque. The bulk of the initial response behaves as the command torque: a 0.1 Hz sine wave. Therefore, for pathlength compensation at bandwidths of 1 and 10 Hz, roughly 40 and 80 dB max attenuation respectively is realized at 0.1 Hz. This translates into 300 and 3 nanometers peak residual response to the command torque. Less attenuation is seen for the higher frequency flexible response, which begins at 0.6 Hz with amplitudes over 10 microns for the fundamental modes. Although the quasi-static response to command torque may be sufficiently attenuated with a fast optical compensator (10 Hz bandwidth), the best reduction for flexible structural response will leave at least a hundred nanometers peak response for the dominant lower modes. Recall the RMS value of a harmonic vibration is equal to $(1/\sqrt{2})$ times the peak value.

Even if optical compensation were able to handle the response from this single translation, which it cannot in this scenario, the burden quickly increases as subsequent maneuvers begin. Therefore, a means to extract energy from the system is required, allowing the response to settle within a single sample period. Figure 5.50 gives an idea for the order of magnitude time required for the pathlength response to damp within 10 nanometers, following a 10 second siderostat motion, for increased structural damping ratio. The above requirement and Figure 5.50 indicate that a 20% structural damping ratio is necessary to achieve the allotted settling time. Since the fundamental modes contribute most of the response, as shown in the time trace, this damping level is needed mainly for the lower modes of the vehicle. This is a large amount of damping, however, and may be difficult to achieve passively given present capability [14,62]. Active damping techniques may also be employed to attain the required net damping ratio. And a detailed investigation of passive and active techniques for this vehicle is required to assess if this level of damping is possible. If the appropriate damping is not achievable through active and passive techniques, this would then necessitate the requirement for active global control techniques.

Minimization of carriage vibrations permits a wider choice of techniques. Based on the assumed disturbance amplitudes for this disturber, response on the order of a few microns peak is expected, a factor of almost 1000 above performance specifications. And the potential for attenuating broadband vibrations on OPTICS using optical compensation, damping and isolation techniques is investigated in the previous sections. However, this disturber presents additional challenges due to its distributed and mobile nature. As the carriage translates across the truss leg, not only does the location of disturbance input change (changing instantaneous frequency response), but the dynamics and inertial properties of the structure in general are modified as the large mass changes position. This does not have a great impact on the fundamental frequency, a few percent maximum, but can shift the modal frequencies sufficiently to effect active techniques which rely on accurate models of the plant dynamics. The worst-case vehicle inertia (greatest differences in primary vehicle inertias, or cross terms) is for siderostats at their midleg locations, and is included in the estimates for environmental disturbances. This represents a delta-inertia of approximately 10^4 $kg\ m^2$ from their nominal location at the apexes. As far as attenuating the mechanization vibrations, it also becomes more difficult to isolate this moving disturber, which is highly dependant upon the specific carriage and track design, not fully addressed here.

Summary

Surely, if enough damping is added to the system in the form of passive (viscoelastic/viscous) and active (rate feedback) augmentation, the disturbance compensation task is lessened. And localized damping and isolation techniques are inappropriate for siderostat inertial disturbances. It is thus the limitation of these structural damping techniques, in terms of capability and system penalties, that will determine requirements for a more aggressive, actively controlled structure to compensate these global-type disturbances. A detailed analysis and optimization of these techniques is beyond the scope of this thesis, and is left for future investigators. Improvements in lightweight mirror technology will permit a lower net mass for these large telescopes, where reaction torque is proportional to this mass. However, these improvements are expected to gain factors of 2 to 3 in mass efficiency [8], still requiring large torques to offset their rapid translation.

To an extent, the minimization techniques discussed in the previous sections may be implemented for the broadband mechanization disturbances. Improvements in structural damping ratio will provide similar benefits for this mobile disturber, just as the more stationary ones. The system pathlength response is attenuated equivalently, peak response and RMS, with increased global damping, regardless of the origin of the disturbance. Localized damping approaches are more constrained, due to the large distance covered by siderostats. Similarly, isolation schemes are inherently more difficult to implement for such a distributed system. However, the first approach is to exhaust these local techniques on appropriate elements of the siderostat carriage/rail system to limit the transmitted vibrations to the vehicle. Effectiveness of these tools will be limited. And based on the assumed disturbance model and performance from the previous sections, it is believed that global techniques, and CST tools implemented at other critical elements (steering mirrors and combining optics) will be required.

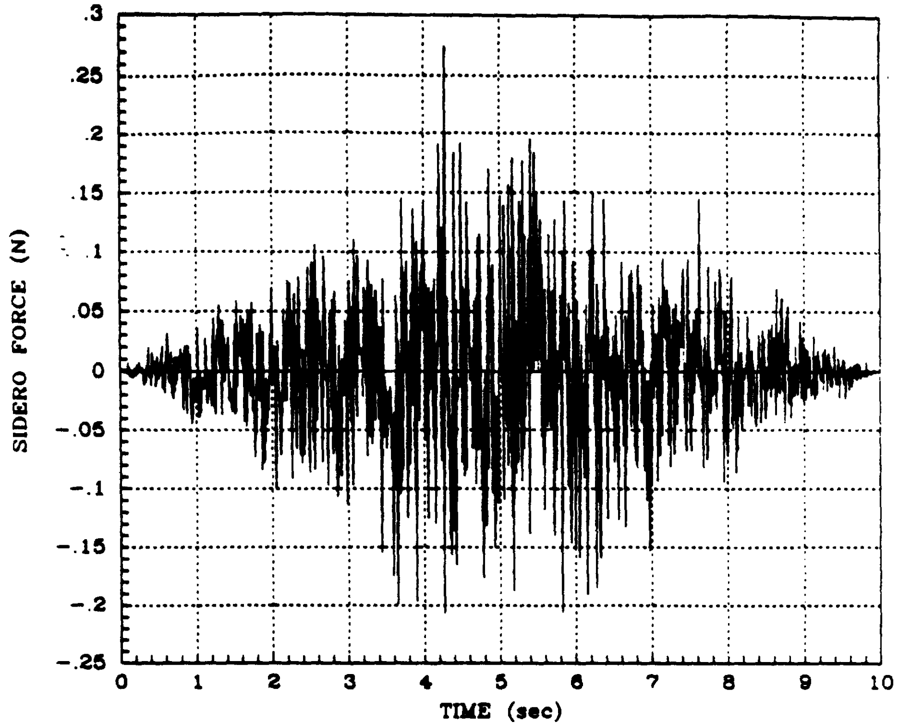

Figure 5.45: Siderostat Mechanization Disturbance Force Model: Random Noise with Amplitudes Proportional to Trolley Velocity.

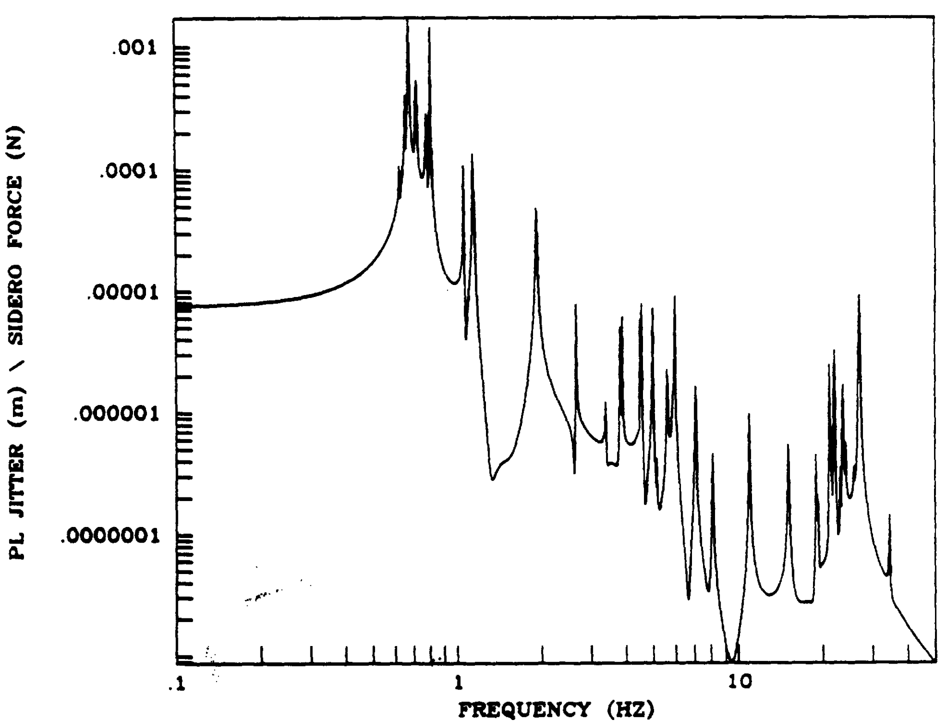

Figure 5.46: Frequency Response from Siderostat Disturbance Force to Pathlength Error.

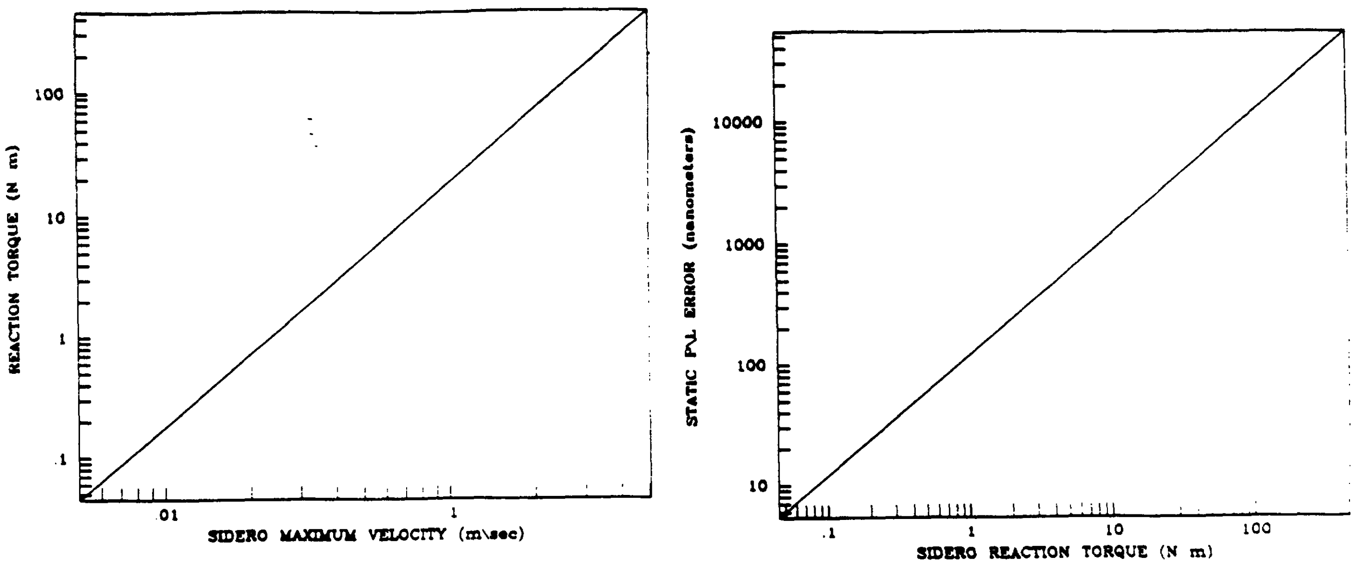

Figure 5.47: Relationship Between Maximum Siderostat Velocity Over 1 Meter, Vehicle Reaction Torque and Resulting Static Pathlength Error.

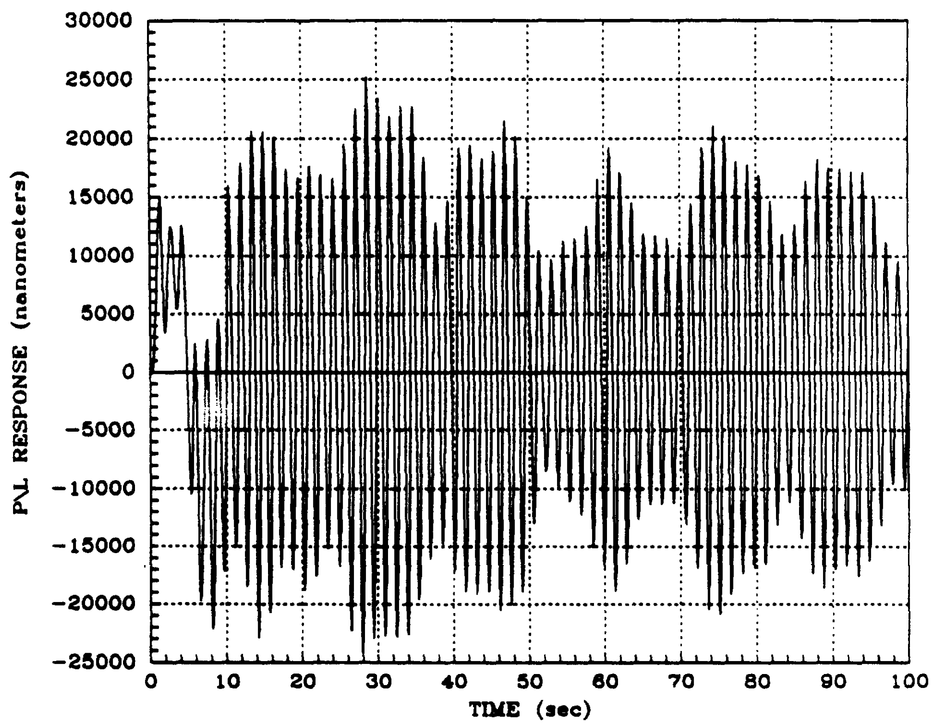

Figure 5.48: Pathlength Time Response to Siderostat Reaction Torque and Carriage Disturbances: 72 Nm Torque Amplitude.

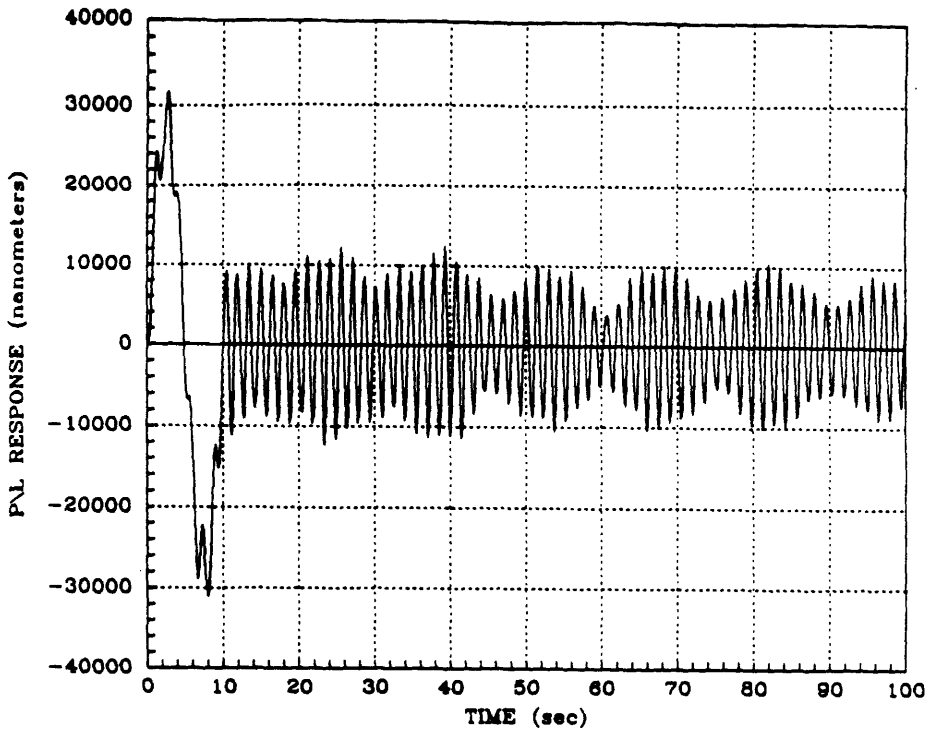

Figure 5.49: Pathlength Time Response to Siderostat Reaction Torque and Carriage Disturbances: Sine Torque Command, 113 Nm Max Amplitude.

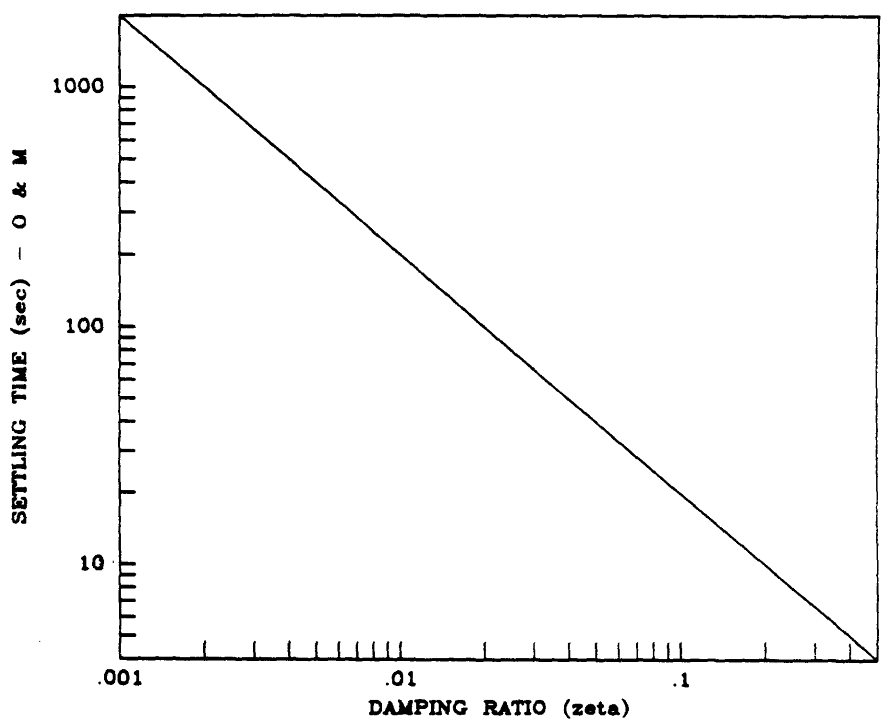

Figure 5.50: Time Required to Settle Within 10 nanometers vs. Structural Damping Ratio for Response to Siderostat Motion Disturbances.

Chapter 6

Generalizations and Recommendations

This chapter summarizes the thesis of this report, drawing a general framework for addressing disturbances and their effects on system performance from knowledge of the disturbance spectrum confronting the precision vehicle, available CST and system tools, and preliminary results investigated in the preceding chapter. The chapter reviews this general approach in a spatial, or system architecture perspective, then places it in a frequency domain context to correspond with basic disturbance classifications, and concludes with a summary of recommendations for future investigation in this area.

6.1 System Approach to Disturbance Minimization

When approaching the disturbance minimization task for a complex system, like the optical interferometer, it is convenient to think in terms of system elements, input-output relations, and net transfer functions. This leads to a spatial formulation, where the various disturbance sources, externally and internally entering the vehicle at certain locations represent the inputs, and all critical elements affecting system performance spatially separated from the disturbances, optical components of a pathlength for example, are the outputs. The transfer function, then is how the spacecraft reacts to disturbances in the form of system performance degradation along a net path through the vehicle, and provides opportunity for limiting their influence to levels consistent with mission specifications. Realistically, the response includes an infinite number of discrete transfer functions, and driving any one of these to zero is not likely with a finite structural link. With these limitations in mind, it is the general attempt through system design to take advantage of these spatial input-output relations as a series of stages contributing to the net response for each disturbance source, toward attenuating their influence at each step such that the residual amount reaching critical elements is manageable and/or consistent with performance requirements.

The basis for the approach derives from traditional industrial noise and vibration control schemes [3,5,17], and a bit of basic system sense, which utilize this transfer function concept in a "source-path-receiver" framework. Reference [5] describes noise control for a manufacturing facility with this approach by: 1. Modifying the machine disturbance sources to reduce their noise output. 2. Altering and/or controlling the factory transmission paths. and 3. Providing the human receiver with disturbance protective equipment. Vibration control efforts for aircraft have also historically used this approach, as documented in Reference [17]. It quickly becomes apparent that this general disturbance minimization method of source-path-receiver is applicable to every situation where sensitive elements reside with vibration-producing sources, including the interferometer spacecraft. Figure 6.1 shows this typical source-path-receiver approach, and characteristic attenuation as seen in the previous chapter.

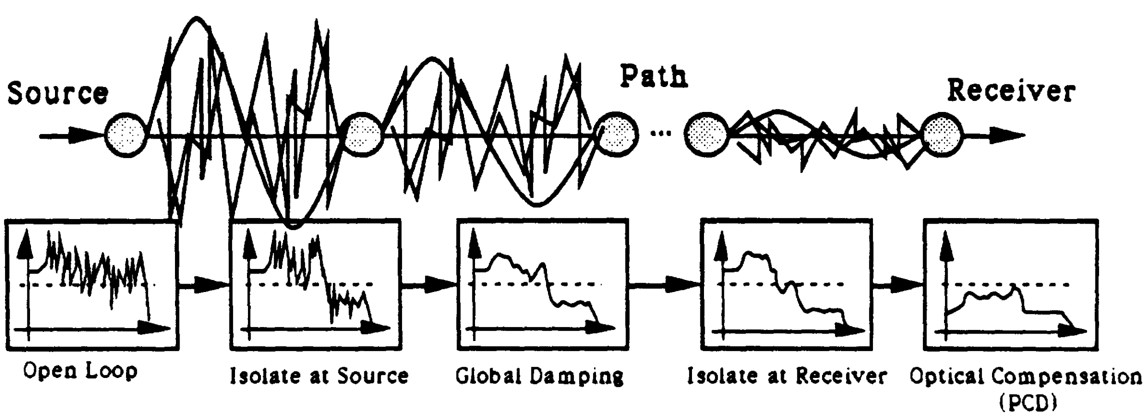

Figure 6.1: Example for the Source-Path-Receiver Approach to Disturbance Minimization Used in Chapter 5.

However, the CST problem is much more challenging, with several inherent differences which demand attention. Precision performance for this class of vehicle requires control to the nanometer level, several orders of magnitude below their terrestrial counterparts, where disturbances of much lower magnitude become significant. Rigid-body control bandwidths overlap structural and appendage modes, producing undesirable interaction. And the dense modal region of the vehicle coincides with a large portion of the disturbance spectrum. These considerations then, together with the basic source-path-receiver concept, provide the framework for disturbance minimization of the OPTICS vehicle, and precision space structures in general. Beyond this basic framework, the approach includes specific areas to address effects outside the vehicle system, from the space environment, and methods available to compensate for disturbances after they have reached the receivers. Figure 6.2

summarizes the disturbance minimization scheme for the OPTICS spacecraft.

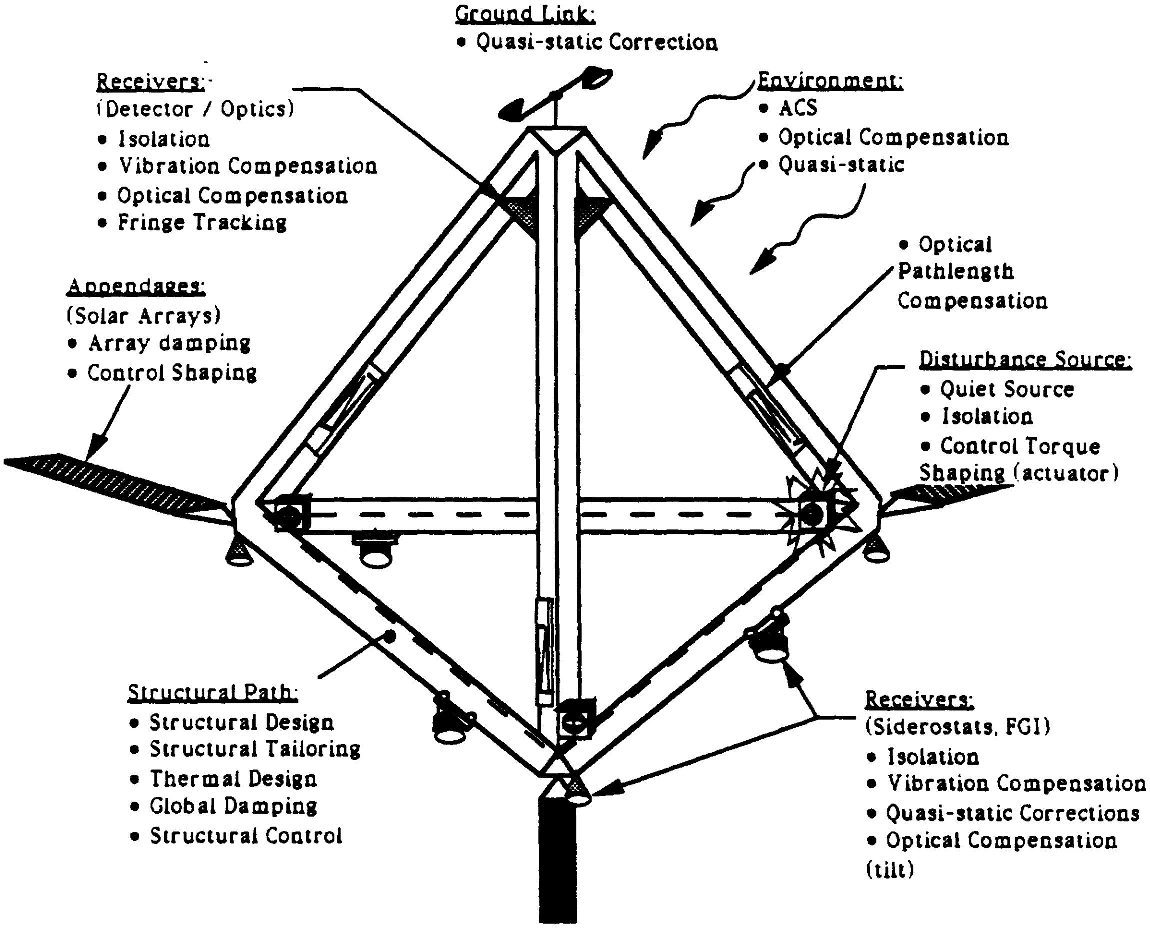

Figure 6.2: OPTICS Spacecraft Disturbance Minimization Approach

6.1.1 Environmental Effects

Chapter 2 indicates that to minimize environmental disturbances is primarily to isoinertialize the vehicle and minimize projected areas. From an orbital viewpoint, the effects of the atmosphere, gravity gradient and magnetic field may be reduced at higher altitudes, and solar eclipse transients are avoided with polar orbits, which hold their own system constraints. The subsequent environmental effects, given orbital parameters and vehicle configuration constraints, are the highly distributed body effects producing rigid body torques, quasi-static deformations from thermal, gravity gradient and pressure effects, and thermal and pressure transients during eclipse and orientation changes. With frequencies on the order of 10^{-4} Hz for rigid body environmental disturbance torques, an attitude control bandwidth on the order of 0.1 Hz is not greatly challenged to provide adequate control authority over these low magnitude disturbers. Quasi-static deformations, for the OPTICS truss with worst-case distributed atmospheric forces are expected to be on the order of hundreds of nano-meters. The subsequent performance errors should be comparable, or less, and may be corrected for by optical compensation (PCD) due to the very low frequency of this disturbance.

The major transient effects, primarily thermal, are seen during solar eclipse in a low earth orbit, and as discussed in Chapter 2, are potentially large sources of error. Beyond orbital constraints, large thermal gradients can be avoided only with sufficient thermal control. For large spacecraft, specifically large distributed trusses, the thermal protection required to prevent such gradients may be prohibitive. This will demand internal compensation through passive and active stabilization. Thus, thermal eclipse transients may be a significant threat to system performance.

6.1.2 Disturbance Minimization at the Source

Before attempting to minimize the effects of disturbances on the spacecraft structure (the path), the first stage involves limiting magnitudes, and preventing the addition of disturbances into the spacecraft system.

Quiet the Source

The principle criteria for choice of ACS and Power subsystem components in the previous chapter are selecting those elements which are inherently quiet and do not introduce significant individual dynamics to the system. A solar array-battery power system is chosen based on its benign nature, in spite of large flexible arrays driving the low frequency dynamics. A potentially more efficient option, solar dynamic, is less desirable for its many moving parts and active operation. The other part of this stage is to quiet the source through design, manufacturing and operational improvements directed toward more efficient operation and reduced imperfections which cause vibrations. The Space Telescope program provides several examples where design improvements lead to reduced line of sight jitter [11,15,18,43]. Careful balancing and precision bearing selection for reaction wheels, an improved shroud design for rate gyros, and gimbal counterbalancing and improved servo control design for high gain antenna pointing all resulted in reduced disturbances. Tape recorders were also evaluated for design improvements, with projected benefit; these however were passed over due to Space Telescope project constraints. As seen on HST, the potential for significant improvements exist, with factors of up to 10 noise reduction, based largely on the fact that typically, manufacturers have not been required to uphold such stringent vibration levels. However, this must be addressed on a component basis and may likely come at a cost.

Damping at the Source of Vibration - Transients

Another attempt to quiet the source is to limit the amount and duration of disturbance energy into the global structure. For large flexible system elements, like solar arrays in the previous chapter, transient effects are often dominant following a tracking maneuver or from excitation by another disturber, and it is desired to dissipate energy as quickly as possible from this low frequency source. This is achieved through damping enhancement applied in the areas of greatest strain rate or displacement on the vibrating member, utilizing the passive or active techniques discussed in Chapter 3. Shaping of the command signal through appendage drive control laws are effective for reducing the magnitude of the initial transient disturbance, as seen in Chapter 5, and can provide damping with rate feedback in the control loop. The high gain antenna drives on HST are a good example of this [11]. Adequate control command shaping and energy dissipation through damping must result in acceptable vibration levels within the specified settling time for the flexible component.

Isolation at the Disturbance Source

This stage attempts to "head 'em off at the pass" before vibrations can reach the global structure, as this represents a discrete location of entry for some disturbances. The goal of this stage is to filter the transmitted disturbance through a selective transmissibility function which is generally constrained at the high frequency end by the desire to attenuate as much of the disturbance spectrum as possible, and at the low end by dynamical considerations and links such as wire harness and fuel or coolant lines. Chapter 3 discusses the available passive and active isolation techniques and limitations of each with respect to transmissibility, and the previous chapter shows the potential for substantial attenuation with isolation, and implications of the high/low frequency constraints.

Three general cases are identified for disturbance isolation at the source: a discrete, stationary disturber; a control actuator; and a moving disturber. The discrete disturber is at once most straightforward, where any of the isolation techniques are applicable, and limited mainly by isolator capability and the desire not to push the low frequency dynamics of the system by being too soft. Examples of these are tape recorders, RTG modules, pumps and other equipment not requiring a rigid vehicle link. When the discrete disturber must now transmit control torques to the vehicle, a lower bound on isolator stiffness is driven by the bandwidth of the required control torques. Space Telescope reaction wheel isolators are a prime example of this [18,42], where the Space Telescope control bandwidth set the isolator corner frequency at 20 Hz, limiting attenuation capability to a factor of roughly two. And for OPTICS CMG's, it is necessary to limit isolator corner frequency to a few Hz, minimum, for adequate separation from the 0.1 Hz ACS bandwidth. A moving disturbance source, such as a translating siderostat, presents an even greater challenge for isolation schemes, and may be considered largely unisolate-able. Translating siderostats and pathlength compensation devices are examples of these, where isolation of the entire carriage rail system would be difficult, but components of the mechanism which produce vibrations, like drive motors, may be isolated in certain applications. Again, isolation must be considered on an individual basis, but offers substantial attenuation, as seen in the previous chapter.

6.1.3 Disturbance Minimization Through the Path

Once the disturbance is in the mainstream of the structure, its effects excite all points of the vehicle according to individual transfer functions from the disturbance location. In other words, the disturbance has now hit the "sounding board" from which undesirable vehicle response is produced.

Structural Design

Structural design of the spacecraft determines its inherent stability and dynamical characteristics. Therefore, it is the intent of the vehicle designer to balance the conflicting desire for maximum stiffness, thermal stability, and overall structural linearity with the least amount of mass. Chapter 3 discusses the means for approaching these characteristics, indicating that the resulting flexible structure may have some degree of non-linearity, particularly at the nanometer level, and limited thermal stability.

Passive Structural Tailoring

Passive structural tailoring attempts to define dynamical characteristics for the vehicle which avoid major disturbance frequencies and/or provide "controllable" characteristics which are synchronized with the control law and disturbance spectrum. Chapter 3 discusses this in a little more detail.

Global Thermal Techniques

Design of the thermal subsystem is important for determining gross stability of the structure to solar eclipses, vehicle attitude changes and onboard fluctuations. Chapter 3 outlines the primary passive and active thermal subsystem tools.

Global Damping Augmentation

The most direct approach is to use the global damping techniques from Chapter 3, which reduce the resonant peaks of response at all points on the vehicle. This is the general smoothing of the response seen from disturbances introduced into the OPTICS model, where the damping ratio, ζ, applies throughout the entire structural plant. Realistically, this is not always efficient in terms of damping performance per mass of augmentation used. For example, to add damping to the fundamental bending mode of a truss leg using damping members (D-struts) does not require the entire truss to be constructed with these devices, but only in the areas of greatest strain rate where they do the most good. Dampers in other locations add damping to a lesser extent and are thus far less efficient. For damping in truss structures, the most efficient passive means are to construct strut members with dissipating elements (viscoelastic, shunted piezoelectric, viscous), or include a dissipative device at the joints, in locations of greatest strain, or strain rate in the lattice. And similarly for active element dampers, where maximum effectiveness is also at the structural antinodes.

Global Structural Control

Active damping is actually a subset of global structural control, using feedback to provide rate-dependant dissipation. However, structural control here means more than added damping, where the global or local transfer function, the input-output relation, is tailored such that a controlled variable(s), displacement of a mirror for example, is driven to a zero state. This is the typical regulator control problem, and a summary of the general structural control approach is given in Chapter 3. Full global control of the OPTICS external flexible pathlength errors, for example, may require sufficient distributed sensing and actuation to provide data and control authority over all of the displacement degrees of freedom for each location where the light path is incident. This multi-variable control problem, then includes the minimization of a cost function including all displacement states at these critical points. This is the control equivalent of providing a completely rigid structure for the interferometer. The actual problem is dependant upon the specific control objective.

Structural control systems generally require accurate knowledge of the dynamical plant and an accurate model to represent the plant in the control loop. These techniques are therefore very sensitive to modelling errors, and uncertainty and variations in the plant dynamics, as from the slewing of large masses for example. They are also acute to limitations and noise in actuators and sensors, particularly in the nanometer range, where many devices have yet to show stable performance. Much research is devoted to this area, however, with high performance possible should sufficient developments occur in nanometer sensing, system identification and control design with modelled uncertainty.

6.1.4 Disturbance Minimization at the Receiver

With disturbance sources creating a "noisy" host vehicle, there remains one stage for limiting disturbances to the critical element: vibration isolation at the receiver.

Isolation at the Receiver

Similar to utilizing the bottleneck at the disturbance source for vibration isolation, the same passive or active techniques may be utilized at the receivers, or critical elements of the performance metric. The results from Chapter 5 for disturbance isolation are equivalent for isolation at this stage, as disturbances have no way of distinguishing whether they're coming or going, except here they have been altered through the structural path and may include multiple contributors, but the basic transmissibility is similar. Again, the most straightforward implementation is for stationary disturbance receivers, like directing optics and detectors. Translating or slewing elements, such as telescope assemblies and gimballed mirrors may also benefit from isolation with a dedicated mount. An isolation stage may be implemented between a siderostat and its translating carriage, or between the structure and a gimballed mirror assembly. A passive example of this is JPL's passive soft mount of HST-type isolators for a reactuated 3-axis gimballed mirror [50]. And active examples include the FEAMIS magnetic payload mount [2].

6.1.5 Disturbance Compensation

Once the disturbance is manifested in the form of vibration of a critical performance element, there are several opportunities to correct both quasi-static and dynamic errors.

Optical Pathlength/Tilt Compensation

By tracking fringes, the interferometer detector is able to measure directly the net pathlength difference between the interfering light beams. The detector also provides information on the wavefront tilt between the two incident beams. Using this information in conjunction with guidance interferometers, and internal and external metrology provides the error contributions from rigid body, internal flexible and external flexible effects, as discussed in Chapter 5. Attitude control provides relatively coarse corrections for the rigid body errors in the differential pathlength, and flexible effects are handled by the net approach herein discussed. By feeding forward this displacement and tilt information to servo control loops around a mirror translator (PCD) and gimbal (FSM), respectively, some compensation of the residual vibrations is achieved. The amount of attenuation possible is constrained by the inherent bandwidth of the mirror servo system. Internal flexible compensation can achieve very high bandwidths (hundreds of Hz) from the high rate internal laser metrology, limited primarily by the dynamical response of the actuator (piezoelectric). Whereas external flexible correction must rely on interferometer data from science star light, and is thus limited by the photon density capacity of the collectors to 1-10 Hz for OPTICS [45]. This represents a long pole for optical compensation and is thus used in the previous chapter to show potential performance improvements.

Ground-Commanded Correction

For intermittent corrections of primary optical misalignment, tip, tilt and defocus errors, a closed, man-in-the-loop correction may be implemented with a telemetry data link. This is envisioned as the same form of correction used on HST [63], where error information is transmitted to the ground and correction signals are sent to various push-pull actuators, such as stepper motors, on the primary and secondary mirrors for alignment accuracy in the micron range. This quasi-static correction may be performed between sampling intervals to prevent additional disturbances from the stepping actuators, and to offload potentially built-up errors during the sample interval. It is likely that this type of capability be required for initial calibration and alignment of major optical components following deployment/construction on orbit, and can provide valuable contingency for operational uncertainty.

Global Transients

Following a vehicle slew or, as seen in Chapter 5, during and after motion of an onboard mass, solar array or siderostat for example, global transient deformations can be major error sources. To prevent such transients, requirements may be imposed on the necessary rates of motion, depending upon the overall system timing budget, and control commands are shaped to avoid the rapid introduction of energy into the system. Given a set slew rate, well shaped commands can reduce the response following a maneuver. This residual transient response must be dissipated through global structural damping, as previously discussed, within acceptable time limits (10 seconds for OPTICS). Performance errors from the low frequency reaction torques during these motions may be compensated with damping, structural control and optical compensation.

6.1.6 Frequency Domain Approach

Major elements of the spatial formulation are placed into a frequency domain perspective that may readily be correlated with disturbance types discussed in Chapter 2 and the open loop responses obtained in Chapter 5. Figure 6.3 shows this breakdown of authority, including system performance requirements, structural and appendage dynamics, and approximate ranges for each of the major tools.

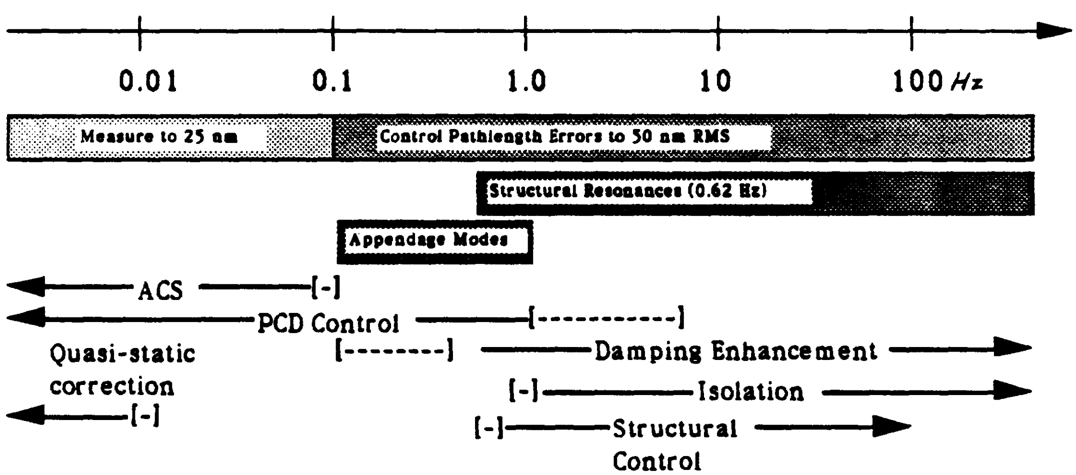

Figure 6.3: Disturbance Minimization in the Frequency Domain

6.2 Summary

This research has supported the thesis of a systems engineering approach to disturbance minimization by assessing the problem through disturbance characterization and overview of CST tools, through investigation into the system design of a representative precision vehicle, OPTICS, and by providing a framework and database from which further research in this area may progress.

Evaluation of the spectrum of spacecraft disturbances in Chapter 2 shows a diverse range of frequencies, magnitudes and types of performance-degrading effects. All precision spacecraft will undoubtedly contain a subset of this total spectrum, depending on the particular subsystems chosen, but are likely to face many of the same disturbance forms. A wide array of controlled-structures techniques are available for confronting these different disturbance forms, including inherently passive means and high performance actively controlled methods outlined in Chapter 3. This study has taken a first cut at the major disturbances: how they are generated, their behavior, magnitudes, frequencies, how they are introduced into the system, the magnitude of performance response (differential pathlength), and general effectiveness of a few combinations of CST techniques for reducing them to required levels. It is shown that appropriate combinations of damping enhancement, vibration isolation and optical pathlength compensation are complementary in their effectiveness for reducing disturbance levels, and are sufficient for several disturbance types in meeting the defined performance specifications.

The conceptual design and subsystem investigation of Chapters 4 and 5 were instrumental in previewing the systems responsibilities associated with minimizing disturbances on a large flexible vehicle. Here, specific constraints associated with subsystem design for minimum disturbance are displayed, namely, choosing inherently benign elements which are vibrationally quiet and do not introduce significant dynamics to the system, or those which are amenable to quieting CST techniques. Also, some of the broader system interactions associated with structural flexibility, precision performance demands and CST are revealed. These place severe constraints on the attitude control system from structural and appendage flexibility, and operational modes of the interferometer (siderostats), and directly influence the attainable performance of the system. What should be extracted from this thesis is that a *total* system must be considered for overall mission performance to be possible.

Finally, this thesis may serve as a foundation from which further research into system-level disturbance minimization and CST spacecraft design may proceed. The following section outlines some of the recommended avenues for future investigation.

6.3 Recommendations for Future Work

I Future work should further concentrate on finding "optimal" system combinations of CST tools for meeting performance, and providing a net benefit to the system. This work will require more accurate modelling and implementation of each of the tools or methodologies, and includes a more rigorous investigation into other system parameters such as mass efficiency, power demands, physical constraints and overall reliability. Also included is an evaluation of how much performance can be extracted from various tools or combinations of tools, and what the net costs to the system are.

II In order to evaluate the system as a whole, more detailed numerical simulation tools are needed. For the OPTICS structural model to represent all of the potential error sources requires the inclusion of rigid body modes, and representative local dynamics from optics and support structure which directly couple into pathlength errors. This will undoubtedly require a more sophisticated model to the continuum approach used here, in order to capture the higher frequency dynamics, and may be available from work on the SERC interferometer testbed. The model should also include flexible appendages, such as solar arrays or antennas, as these were shown to produce significant dynamics. With an accurate plant model, the system analysis should include the capability for closed-loop control, to be amenable to ACS control law evaluation, structural control methodologies, and to capture the total pointing and error control system.

III Optical pathlength compensation (PCD) is shown to be a critical tool for handling disturbance response, and may greatly reduce the burden on a structural control system. Further work should be devoted to investigating the maximum performance improvement attainable with these devices, in terms of bandwidth and operational regions, and integration into the overall system model. Work at the Jet Propulsion Laboratory is beginning to address this issue.

IV Attitude control interactions are increasingly important as spacecraft become more flexible, and as shown here, must operate amongst constraints from environmental disturbances, flexibility effects and operation of some elements. Future work could focus on investigating the system trades associated with these conflicting trends, particularly with respect to its interaction with a structural control system as structures continue to become more flexible.

Bibliography

[1] Agrawal, B.N., *Design of Geosynchronous Spacecraft*, Prentice Hall, Inc., Englewood Cliffs, NJ 1986.

[2] Allen, T.S., et. al., "FEAMIS: A Magnetically Suspended Isolation System for Space-Based Materials Processing," AAS 86-017, Sperry Corporation, Aerospace and Marine Group, Phoenix, AZ.

[3] Bell, L.H., *Industrial Noise Control: Fundamentals and Applications*, Marcel Dekker, Inc. NY, 1982.

[4] Bennett, G.L., et. al., "Dynamic Isotope Power (DIPS) System Technology Program", *Proceedings of the 23rd IECEC Conference*, Denver, CO 1988.

[5] Berendt, R.D., and Corliss, E.L., *Quieting: A Practical Guide to Noise Control*, National Bureau of Standards Handbook 119, US Dept. of Commerce, 1976.

[6] Chambers, G.J., "What is a Systems Engineer ?," IEEE Transactions on Systems, Man, and Cybernetics, vol. SMC-15, No. 4, July/August 1985.

[7] Chestnut, H., *Systems Engineering Tools*, Advanced technology Laboratories, General Electric Co., John Wiley and Sons,Inc., 1965.

[8] Connolly, A., "ESA Technology Research Activities on Lightweight Mirrors," N88-10629 ESA Workshop on Optical Interferometry in Space, Grenada, Spain, June 1987.

[9] Crawley, E., 16.93 class notes: *Dynamics and Control of Space Structures*, MIT, Spring 1989.

[10] Davis, L.P., Wilson, R.E., Jewell, J.E., and Rodden, J.J., "Hubble Space Telescope Reaction Wheel Assembly Vibration Isolation System," NASA Marshall SFC, Huntsville AL.

[11] Dodder, R.H., et.al., "Space Telescope Antenna Pointing System Analysis and Test," *IFAC: Automatic Control in Space,* Tolouse, France 1985.

[12] Dougherty, H., Brady, A.M., and Reschke, L.F., "Noise Characterization and Minimization of a Precision Gyroscope Rate Sensor," Eleventh Biennial Guidance Test Symposium, Holloman AFB, NM, 1983.

[13] Gariboti, J.F., "Requirements and Issues for the Conrol of Flexible Space Structures," AIAA Paper 84-1025, HR textron, Inc., 2485 McCabe Way, Irvive, CA 92714.

[14] Hagood, N.W., *Development and Experimental Verification of Damping Enhancement Methodologies for Space Structures,* 1988 SM Thesis, Department of Aeronautics and Astronautics, M.I.T., Cambridge, MA.

[15] Haile, W.B., "Optical Jitter Caused by Engineering/Science Tape Recorders," Engineering Memorandum No. S&M 321, Space Telescope Program, February 15, 1982.

[16] Hall, A.D., *A Methodology for Systems Engineering,* Bell Telephone Labs, Inc., D. VanNostrand Co., Inc., 1962.

[17] Harris, C.M., and Crede, C.E., *Shock and Vibration Handbook, Volume 3: Engineering Design and Environmental Conditions,* McGraw-Hill Book Co., 1961.

[18] Hasha, M.D., "Passive Isolation/Damping System for Hubble Space Telescope Reaction Wheels," *The 21st Aerospace Mechanisms Symposium,* NASA Johnson Space Center, May, 1987, N87 - 29873.

[19] Hastings, 16.851 class notes: *Space Propulsion and Power,* MIT, Spring 1989.

[20] Hughes, P.C., *Spacecraft Attitude Dynamics,* John Wiley and Sons, 1986.

[21] Jacques, B., *Design of Structures for Control,* 1990 SM Thesis, Department of Aeronautics and Astronautics, M.I.T., Cambridge, MA.

[22] "JPL CSI Test Bed Development Preliminary Design Review," Jet Propulsion Laboratory, July 26, 1989.

[23] Laskin, R.A., and San Martin, M., "Control/Structure System Design of a Spaceborne Optical Interferometer," AAS 89-424, *AAS/AIAA Astrodynamics Specialist Conference,* Stowe, VT 1989.

[24] Laskin, R.A., and Sirlin, S.W., "Future Payload Isolation and Pointing System Technology," Jet Propulsion Laboratory.

[25] Meirovich, L., *Elements of Vibration Analysis*, Second Edition, McGraw-Hill Book Company, 1986.

[26] McGregor, J.M., "Mt. Wilson Disturbance Measurements," Jet Propulsion Laboratory Interoffice Memorandum, 3543-89-273, November 15, 1989.

[27] Murray, C.A., *Apollo, The Race to the Moon*, Simon and Schuster, New York, 1989.

[28] NASA [1]: *NASA Space Systems Technology Model*, Vol. I, II and III, June 1985, NASA/OAST Code RS.

[29] NASA [2]: *Spacecraft Magnetic Torques*, NASA SP- 8018, March 1969.

[30] NASA [3]: *Spacecraft Gravitational Torques*, NASA SP- 8024, May 1969.

[31] NASA [4]: *Spacecraft Radiation Torques*, NASA SP- 8027, October 1969.

[32] NASA [5]: *Spacecraft Aerodynamic Torques*, NASA SP- 8058, January 1971.

[33] NASA [6]: *A Review of Micrometeoroid Flux Measurements and Models for Low Orbital Altitudes of the Space Station*, NASA TM- 86466, September 1984.

[34] NASA [7]: *Space and Planetary Environment Criteria Guidelines for Use in Space Vehicle Development*, Vol. 1, NASA TM- 82478, 1982.

[35] NASA [8]: *Spacecraft Mass Expulsion Torques*, NASA SP - 8034, December 1986.

[36] NASA [9]: *Propellant Slosh Loads*, NASA SP - 8009, August 1968.

[37] NASA [10]:"COSMIC: A Conceptual Definition Study," NASA, Marshall Space Flight Center, December, 1981.

[38] Ochocki, Capt. D.R., *Space Based Laser Disturbance Compendium*, AFWL-TN-85-06, Parts 1,2 and 3, July 1986.

[39] Osborne, N.A., and Rittenhouse, D.L., "The Modelling of Friction and its' Effect on Fine Pointing Control," Martin Marietta Aerospace, Denver, CO, AIAA Paper 74-875.

[40] Pue, A.J., et.al., "Configuration Tradeoffs for the Space Infrared Telescope Facility Pointing Control System," The Johns Hopkins University, AIAA Paper 85-1856.

[41] Reppucci, G.M., and Sorenson, A.A., "Space Station Power System Challenges." *Proceedings of the 20th Intersociety Energy Conversion Engineering Conference*, SAE P-164, Miami Beach, FL, August 1985.

[42] Rodden, J.J., et.al., "Line of Sight Performance Improvement with Reaction Wheel Isolation," AAS Paper 86-005, February 1986.

[43] Rodden, J.J., "Noise Performance Investigation and Improvement of a Rate Integrating Gyroscope," Eleventh Biennial Guidance Test Symposium, Holloman AFB, NM, 1983.

[44] San Martin, M., personal correspondence, Jet Propulsion Laboratory, Pasadena, CA.

[45] San Martin, M., "Guide Star Magnitude Selection and Their Relation to Path Length and Wave-Front Tilt Control Loop Bandwidth." Jet Propulsion Laboratory, Interoffice Memorandum, 33-89-319, May 18, 1989.

[46] Scribner, K., *Active Narrowband Vibration Isolation for Compact Payloads With Resonant Bases,* 1990 SM Thesis, Department of Aeronautics and Astronautics, M.I.T., Cambridge, MA.

[47] SERC Testbed Development Project: Hyde, T.; Jacques, R.; Kim, E.; Miller, D.; Spangler, R.; Ting, J.; Eyerman, C.E. et. al..

[48] Sincarsin, G.B., and Hughes, P.C., "Torques From Solar Radiation Pressure Gradient During Eclipse," *J. Guidance, Control and Dynamics,* No. 6, pp. 511-517, 1983.

[49] Singer, F.S.(editor), *Torques and Attitude Sensing in Earth Satellites,* Academic Press, NY 1964.

[50] Sirlin, S.W., "Vibration Isolation Versus Vibration Compensation on Multiple Payload Platforms," *3rd Annual NASA/DOD CSI Conference*, January 30 - February 2, 1989.

[51] *Space Science in the 21st Century: Imperatives for the Decades 1995 to 2015,* (Task Group on Astronomy and Astrophysics, Space Science Board, Commission on Physical Sciences, Mathematics and Resources), The National Research Council, National Academy Press, Washington, DC, 1988.

[52] "Space Telescope / Solar Array Interaction Study," ST/SE - 24, Section G, Part 10, Lockheed MSC, LMSC/F061010.

[53] Sun, C.T., Kim, B.J., Bogdanoff, J.L., "On the Derivation of Equivalent Simple Models for Beam- and Plate-Like Structures in Dynamic Analysis," Purdue University, 22nd Structures, Structural Dynamics and Materials Conference, 1981.

[54] Susko, M., "A Review of Micrometeoroid Flux Measurements and Models for Low Orbital Altitudes of the Space Station," NASA Technical Memorandum, NASA-TM-86466, 1984.

[55] Traub, W., "Optical Path Fluctuations," Memorandum, Smithsonian Astrophysical Observatory, Center for Astrophysics, February 15, 1989.

[56] Tung, F.C., "Advanced X-Ray Astrophysics Facility - Preliminary Pointing Control Analyses," TRW Space and Technology Group, NAS 8-37751, November 9, 1988.

[57] VanLandingham, E., "Space Power Technology to Meet Civil Mission Requirements," *Proceedings of the 23rd IECEC Conference,* Denver, CO 1988.

[58] von Flotow, A.H., "Control-Motivated Dynamic Tailoring of Truss-Work Structures," AIAA Guidance and Control Conference, Williamsburg, VA, August 1986.

[59] Wertz, J.R.(editor), *Spacecraft Attitude Determination and Control,* D. Reidel Publishing Co., Dordrecht, Holland 1987.

[60] Wetch, J.R., et. al., "The application and use of Nuclear Power for Future Spacecraft", *Proceedings of the 20th Intersociety Energy Conversion Engineering Conference,* SAE P-164, Miami Beach, FL, August 1985.

[61] Wiggins, L.E., "Relative Magnitudes of the Space Environment Torques on a Satellite," *AIAA Journal 2,* (No.4), pp. 770 - 771, 1964.

[62] Wilson, J.F. and Davis, L.P., "Viscous Damped Space Structure for Reduced Jitter," 58th Shock and Vibration Symposium, Huntsville, AL, August 1987.

[63] Wojtalik, F.S., "Hubble Space Telescope Systems Engineering," IFAC 10th Triennial World Congress, Munich, FRG 1987.

[64] Woodcock, G.R., *Space Stations and Platforms,* Orbit Book Company, Malabar, FL 1986.